

The discovery channel at the Neutrino Factory: $\nu_{\mu} \rightarrow \nu_{\tau}$ pointing to sterile neutrinos

This article has been downloaded from IOPscience. Please scroll down to see the full text article.

JHEP08(2009)041

(<http://iopscience.iop.org/1126-6708/2009/08/041>)

[The Table of Contents](#) and [more related content](#) is available

Download details:

IP Address: 80.92.225.132

The article was downloaded on 03/04/2010 at 10:21

Please note that [terms and conditions apply](#).

The discovery channel at the Neutrino Factory: $\nu_\mu \rightarrow \nu_\tau$ pointing to sterile neutrinos

Andrea Donini,^a Ken-ichi Fuki,^c J. López-Pavón,^a Davide Meloni^b and Osamu Yasuda^c

^a*Instituto Física Teórica UAM/CSIC, Universidad Autónoma de Madrid Cantoblanco, E-28049 Madrid, Spain*

^b*I.N.F.N., Sezione di Roma III and Università degli Studi di "Roma Tre", Dipartimento di Fisica, Via Vasca Navale 84, I-00146 Rome, Italy*

^c*Tokyo Metropolitan University, Department of Physics, Minami-Osawa 1-1 Hachioji, Tokyo 192-0397, Japan*

E-mail: andrea.donini@uam.es, fuki@phys.metro-u.ac.jp,
jacobo.lopez@uam.es, meloni@fis.uniroma3.it,
yasuda@phys.metro-u.ac.jp

ABSTRACT: We study the potential of a Neutrino Factory in constraining the parameter space of a scheme with one sterile neutrino separated from three active ones by an $O(1)$ eV^2 mass-squared difference. We present approximated analytic expressions for the oscillation probabilities, showing that the greatest sensitivity to sterile neutrinos at a Neutrino Factory can be achieved using the $\nu_\mu \rightarrow \nu_\mu$ and the $\nu_\mu \rightarrow \nu_\tau$ oscillations. We have studied two setups: a Neutrino Factory with 50 GeV (20 GeV) stored muons, with two detectors of the Hybrid-MIND type (a magnetized ECC next to a magnetized iron calorimeter), located at $L = 3000, 7500$ km ($L = 4000, 7500$ km) from the source. Four channels have been used: $\nu_e \rightarrow \nu_\mu, \nu_\tau$; $\nu_\mu \rightarrow \nu_\mu, \nu_\tau$. The relevant backgrounds, efficiencies and systematic errors have been taken into account, and we have discussed dependence of the sensitivities on the systematic errors. We have found that the 50 GeV (20 GeV) setup can constrain $\sin^2 2\theta_{13}^{(4fam)} \leq 7 \times 10^{-5} (2 \times 10^{-4})$; $\theta_{34} \leq 12^\circ (14^\circ)$; and $\theta_{24} \leq 7.5^\circ (8^\circ)$. Our results hold for any value of $\Delta m_{SBL}^2 \gtrsim 0.1 eV^2$. Eventually we have shown that, if a positive signal is found, the proposed setup is able to measure simultaneously θ_{34} and δ_3 with a precision of few degrees and few tens of degrees, respectively, solving the so-called "intrinsic" and "sign degeneracies". Combination of ν_μ disappearance and of the $\nu_\mu \rightarrow \nu_\tau$ channel, that will be called "the discovery channel", at the two baselines is able to measure at 99% CL a new CP-violating phase δ_3 for $\sin^2 2\theta_{34} \geq 0.06$.

KEYWORDS: Neutrino Physics, Beyond Standard Model, Solar and Atmospheric Neutrinos

ARXIV EPRINT: [0812.3703](https://arxiv.org/abs/0812.3703)

Contents

1	Introduction	1
2	Four neutrino schemes	5
2.1	(2+2)-schemes	6
2.2	(3+1)-schemes with the LSND constraint	6
2.3	(3+1)-schemes without the LSND constraint	6
2.4	Oscillation probabilities at the Neutrino Factory in the (3+1)-scheme	8
3	The Neutrino Factory and the Hybrid-MIND detector	10
3.1	The MIND detector: $\nu_e \rightarrow \nu_\mu$ and $\nu_\mu \rightarrow \nu_\mu$	12
3.2	The MECC detector: $\nu_e \rightarrow \nu_\tau$ and $\nu_\mu \rightarrow \nu_\tau$	13
4	Sensitivity to (3 + 1) sterile neutrinos at the Neutrino Factory	16
4.1	Sensitivity to $(\theta_{13}, \theta_{14})$	16
4.1.1	Sensitivity to $(\theta_{13}, \theta_{14})$	16
4.1.2	Sensitivity to $U_{e4}U_{\mu4}$ and $U_{e4}U_{\tau4}$	24
4.2	Sensitivity to $(\theta_{24}, \theta_{34})$	25
4.3	Discrimination of the four neutrino schemes	30
4.4	Dependence of sensitivity on the systematic errors	33
4.5	A CP-violating sterile neutrino signal	35
5	Conclusions	41
A	The mixing matrix elements $U_{\alpha j}$	42
B	Oscillation probabilities by the KTY formalism	43

1 Introduction

From the results of solar [1–8], atmospheric [9, 10], reactor [11–14] and accelerator [15–18] neutrino experiments, we now know that neutrinos have masses and mixings. In the framework of three flavor oscillations, neutrino oscillations are described by three mixing angles, θ_{12} , θ_{13} , θ_{23} , and one CP phase δ , as well as two independent mass-squared differences, Δm_{21}^2 and Δm_{31}^2 . In the standard parametrization [19] for the three flavor mixing matrix U_{PMNS} [20–23], when θ_{13} is small, $(\Delta m_{21}^2, \theta_{12})$ and $(\Delta m_{31}^2, \theta_{23})$ correspond to the mass-squared difference and the mixing angle of the solar and atmospheric oscillations, respectively. From the solar neutrino experiments we have $\Delta m_{\text{sol}}^2 \simeq 7.7 \times 10^{-5} \text{ eV}^2$, $\sin^2 \theta_{12} \simeq 0.30 - 0.31$ [24, 25], and from the atmospheric neutrino experiments $|\Delta m_{\text{atm}}^2| \simeq$

$2.4 \times 10^{-3} \text{ eV}^2$, $\sin^2 2\theta_{23} \simeq 0.47 - 0.50$ [24, 25]. As for θ_{13} , the reactor data [11–13] and three-family global analysis of the experimental data give an upper bound,¹ $\sin^2 \theta_{13} \leq 0.04$, while we have no information on δ at present (see, however, ref. [28]).

In order to determine precisely the remaining two parameters θ_{13} and δ , long baseline experiments with intense neutrino beams have been proposed [29–35]. As in the case of the B factories [36, 37], these precision measurements will allow us to look for deviation from the standard three flavor oscillations scenario. Possible scenarios for such deviations include non-standard interactions which affects the neutrino productions and detections [38], those which modify the neutrino propagations [39, 40], light sterile neutrinos [22], unitarity violation due to the effect of heavy fermions [41, 42], etc. These scenarios (except the non-standard interactions which change the neutrino propagation, only), in general break unitarity of the PMNS matrix. As in the B physics, test of unitarity is one of the important problems which should be investigated in the future long baseline experiments (see ref. [43] for a review). Among the proposed long baseline experiments with high intense neutrino beams, a Neutrino Factory [34], which uses a muon storage ring to produce neutrino beams from muon decays, is expected to have excellent sensitivity to θ_{13} and δ .

One of the advantages of a Neutrino Factory is that the flux is flavor-rich, well under control and with no ν_τ contamination. This last point is of particular relevance for new physics searches in neutrino oscillations, since the $\nu_\mu \rightarrow \nu_\tau$ oscillations provide one of the most promising signal of non-standard physics in oscillations (as it will be shown in section 2.4 for sterile neutrinos; see also refs. [44–47]) and ν_τ detection is important to check unitarity of the PMNS matrix (although, clearly, unitarity violations of the PMNS matrix are best studied in weak decay processes, [41]). A Neutrino Factory with multi-GeV muons is a powerful facility to look for τ 's signals, if detectors dedicated to τ -detection are provided. Notice that oscillations into ν_τ cannot be measured by so-called β beams [35] and that high energy conventional superbeams are affected by ν_τ contamination of the flux (through B -mesons decay).

Four-neutrino mass schemes have attracted much attention since the announcement by the LSND group on evidence for neutrino oscillations $\bar{\nu}_\mu \rightarrow \bar{\nu}_e$ with a mass squared difference $\Delta m^2 \sim O(1) \text{ eV}^2$ [48–50]. Because the mass squared difference suggested by the LSND result is much larger than those for the solar and atmospheric neutrino oscillations, in order to explain all these data in terms of neutrino oscillations, it is necessary to introduce *at least* a fourth light neutrino state. From the LEP data [19, 51], which indicate that the number of weakly interacting light neutrinos is three, the fourth state has to be a sterile neutrino. For this reason, the LSND signal could be considered as an evidence for the existence of a sterile neutrino. Recently the MiniBooNE experiment [52] gave a negative result for neutrino oscillations with the mass squared difference $\Delta m^2 \sim O(1) \text{ eV}^2$ which was suggested by the LSND data, and it has become difficult for four-neutrino models to explain the LSND data. The so-called (3+2)-scheme with two sterile neutrinos has also been proposed [53] to account for LSND, but also in this case, tension with

¹ In refs. [25–27], a global analysis of the neutrino oscillation data has been shown, in which a non-vanishing value for θ_{13} is found. This result, however, is compatible with $\theta_{13} = 0$ at less than 2σ , and it has not been confirmed by the other groups performing global fits [24].

the disappearance experiments remains, as long as we take into account the LSND data. Adding a third sterile neutrino does not seem to help [54], and in general global analyses seem to indicate that sterile neutrinos alone are not enough to account for all the data in terms of neutrino oscillations. Models with sterile neutrinos and exotic physics have been therefore proposed [55–59].

While the efforts to account for all the data including the LSND in terms of neutrino oscillations have been unsuccessful, sterile neutrino scenarios which satisfy all the experimental constraints *except* LSND are still possible. Even if the inclusion of light sterile neutrinos is not needed to explain the present experimental data, it is certainly worth investigating scenarios where sterile neutrinos do appear and constrain their parameter space. Light singlet fermions are indeed present in the low-energy spectrum of many theories and models including them represent, for example, phenomenologically natural frameworks to break three-flavor unitarity.

In ref. [60] the (3+1)-scheme without imposing the LSND constraint was studied in the context of the CNGS experiments [61], finding that if the OPERA detector is exposed to the nominal CNGS beam intensity, a null result can improve a bit the present bound on θ_{13} , but not those on the active-sterile mixing angles, θ_{14} , θ_{24} and θ_{34} .

In this paper, we have extended the analysis in ref. [60] to the case of a Neutrino Factory experiment. We have first of all extended the analytic computation of the oscillation probabilities for the (3 + 1)-model at long baseline experiments in matter using the formalism by Kimura-Takamura-Yokomakura (KTY) [62, 63]. Approximated formulæ in powers of θ_{13} , of the deviations from maximality of θ_{23} ($\delta\theta_{23}$) and of the active-sterile mixing angles, θ_{i4} , have been obtained. On the basis of this analysis, we have found that the greatest sensitivity to the active-sterile mixing angles is achieved using the $\nu_\mu \rightarrow \nu_\mu$ and $\nu_\mu \rightarrow \nu_\tau$ channels (as it was noticed, for example, in refs. [64, 65] and refs. therein). To take full advantage of these signals, detectors capable of both ν_μ and ν_τ identification are needed. In our numerical analysis we have, thus, assumed a detector of the Hybrid-MIND type [66]: a 50 kton magnetized iron calorimeter next to a 4 kton Emulsion Cloud Chamber with magnetized iron plates. This detector has a greater efficiency to $\nu_\mu \rightarrow \nu_\tau$ than the standard OPERA-type ECC, with lead plates acting as target.

We have then extensively analyzed the physics reach of a 50 GeV Neutrino Factory which has 2×10^{20} useful muon decays per year aimed at two detectors of the Hybrid-MIND type located at $L = 3000$ km and $L = 7500$ km from the source, with both polarities running for 4 years each. As a consistency check, we have also studied the case of a 20 GeV Neutrino Factory which has 5×10^{20} useful muon decays per year aimed at the same two detectors of the Hybrid-MIND type located at $L = 4000$ km and $L = 7500$ km, again with both polarities running for 4 years each. The latter option was the scenario which was suggested in the *International Scoping Study for a future Neutrino Factory and Super-Beam facility* [43].

Four signals have been considered: the "standard" Neutrino Factory channels, the golden channel $\nu_e \rightarrow \nu_\mu$ [67] and the silver channel $\nu_e \rightarrow \nu_\tau$ [68]; the ν_μ disappearance channel; and the novel signal $\nu_\mu \rightarrow \nu_\tau$, that will be named in this paper the " *discovery channel*". We think that this name is appropriate due to its high-sensitivity to new physics

signals in neutrino oscillations, as found from the theoretical analysis of oscillation probabilities. At the same time, however, we are forced to remind that the effective potential of this channel is tightly linked to the performances of the proposed detectors able to identify τ 's, that are still in a very preliminary design phase and that should be studied further.

Using the first two channels at the 50 GeV Neutrino Factory, we can extend the three-family θ_{13} -sensitivity plots to the four-family $(\theta_{13}^{(4fam)}, \theta_{14})$ -plane, putting a stringent upper bound on $\theta_{13}^{(4fam)}$ mixing angle, $\sin^2 2\theta_{13}^{(4fam)} \lesssim O(10^{-4})$ at 90% CL. Using the combination of the ν_μ disappearance channel and of the "discovery channel" $\nu_\mu \rightarrow \nu_\tau$ at the 50 GeV Neutrino Factory, we are able to constrain the active-sterile mixing angles θ_{34} and θ_{24} , $|\theta_{34}| \lesssim 12^\circ$ and $|\theta_{24}| \lesssim 7.5^\circ$ at 90% CL. We have found that the combination of the shortest baseline data with the longest baseline ones significantly improves the sensitivity in both planes, $(\theta_{13}^{(4fam)}, \theta_{14})$ and $(\theta_{24}, \theta_{34})$.

We have, then, compared the results for the 50 GeV Neutrino Factory with those that can be obtained at the 20 GeV ISS-inspired one (with 2×10^{20} and 5×10^{20} useful muon decays per year per baseline, respectively). We have found that the former setup has a greater potential than the latter for sterile neutrino searches, in particular for the simultaneous measurement of θ_{24} and θ_{34} . We interpret this result as consequence of the larger τ statistics that can be collected using higher energy muons.

We have also studied the region of the four-family parameter space for which a four-neutrino signal cannot be confused with the three-family model, determining the "discovery potential" of the Neutrino Factory in the $(\theta_{13}^{(4fam)}, \theta_{14})$ - and $(\theta_{24}, \theta_{34})$ -planes.

We have, then, performed a preliminary study of the potential of the 50 GeV Neutrino Factory to measure four-family parameters, showing 99% CL contours in the (θ_{34}, δ_3) - and $(\theta_{13}^{(4fam)}, \delta_2)$ -planes. We have found that the shortest baseline data are affected by "intrinsic" [69] and "sign" degeneracies [70]. On the other hand, the longest baseline data have a rather good precision in θ_{34} and are not affected by those degeneracies. The combination of the two baselines, thus, is able to measure simultaneously θ_{34} and δ_3 with a precision of a few degrees and a few tens of degrees, respectively. In this context, we have also studied the " δ_3 -discovery potential". We have found that the ν_μ disappearance channel can measure a CP-violating δ_3 for $\sin^2 2\theta_{34} \geq 0.4$ with a 50% CP-coverage; the combination of the ν_μ disappearance and of the $\nu_\mu \rightarrow \nu_\tau$ "discovery" channels, however, is able to measure a CP-violating δ_3 for $\sin^2 2\theta_{34} \geq 0.06$ with a 80% CP-coverage. The combination of the two channels is extremely effective in solving correlations and degeneracies, thus improving the δ_3 -discovery potential by an order of magnitude in $\sin^2 2\theta_{34}$. We have also shown how the measurement of the three-family like CP-violating phase δ_2 is modified by the presence of non-vanishing active-sterile mixing angles.

Eventually, we have studied the impact of statistic and systematic errors on the performance of the detector proposed to identify τ 's (the magnetized ECC component of the Hybrid-MIND detector, MECC). We have found that, to improve significantly the potential of the MECC, systematic errors should be kept at the level of a few percents. On the other hand, increasing the mass of the MECC from 4 kton to 8 kton is found to be of marginal impact. It is clear from this analysis that the τ -detector section of the Hybrid-MIND should be studied further to understand its ultimate potential. To this purpose,

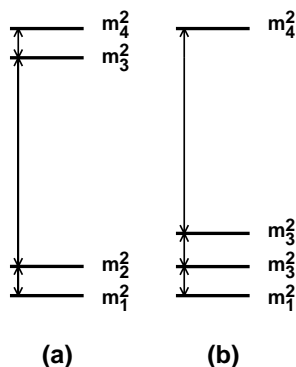


Figure 1. The two classes of four-neutrino mass spectra, (a): (2+2) and (b): (3+1).

we will take great advantage of the understanding of the ECC technology and systematics after the first years of OPERA data taking.

An analysis such as this is not completely new: first studies of sterile neutrinos at a Neutrino Factory were presented at the first NuFact workshop in Lyon in 1999 [71, 72] in the framework of the so-called (2+2)-schemes and subsequently extended to the case of (3+1)-schemes in ref. [64]. The possibility to use the Neutrino Factory detectors, optimized to look for three-family oscillations, to disentangle three- from four-neutrino signals was considered in ref. [65, 73]. Recently, in ref. [74] a four-family neutrino analysis in the spirit of ref. [60] has been performed. The main differences between this paper and ref. [74] are (i) that careful numerical analyses are carried out here by taking into account backgrounds, efficiencies and systematic errors specific to the considered signals and setup, and (ii) that the four channels $\nu_\mu \rightarrow \nu_\tau$, $\nu_\mu \rightarrow \nu_\mu$, $\nu_e \rightarrow \nu_\mu$, $\nu_e \rightarrow \nu_\tau$ at the Neutrino Factory are considered and their contributions are clarified in the present paper.

The paper is organized as follows. In section 2 the main features of four-neutrino schemes and the present bounds on the mixing angles in these scenarios are briefly summarized. Furthermore we compute approximated oscillation probabilities in matter in the atmospheric regime using the KTY formalism [62, 63] (details of our computations are given in appendix A). In section 3 we remind the details of the considered Neutrino Factory setup. In section 4 we present our results using various channels at the Neutrino Factory. Finally, in section 5 we draw our conclusions.

2 Four neutrino schemes

Four-neutrino schemes consist of one extra sterile state in addition to the three weakly interacting ones. Depending on whether one or two mass eigenstate(s) are separated from the others by the largest mass-squared gap,² the schemes are called (3+1)- and (2+2)-schemes, as is shown in figure 1. In the (3+1) schemes, there is a group of three close-by

²The only assumption for the largest mass-squared difference is that oscillations caused by this mass-squared difference are averaged. So the results hold for any value of $\Delta m_{\text{sbl}}^2 \gtrsim 0.1 \text{ eV}^2$. Interesting models with "sterile" neutrino with masses $m \sim O(1) \text{ KeV}$ can be found, for example, in ref. [75].

neutrino masses that is separated from the fourth one by the larger gap. In (2+2) schemes, there are two pairs of close masses separated by the large gap. These two classes lead to very different phenomenological consequences.

2.1 (2+2)-schemes

A characteristic feature of (2+2) schemes is that the extra sterile state cannot simultaneously decouple from *both* solar and atmospheric oscillations. The fraction of sterile neutrino contributions to solar and atmospheric oscillations is given by $\eta_s \equiv |U_{s1}|^2 + |U_{s2}|^2$ and $1 - \eta_s \equiv |U_{s3}|^2 + |U_{s4}|^2$, respectively, where the mass squared differences Δm_{21}^2 and $|\Delta m_{43}^2|$ are assumed to be those of the solar and atmospheric oscillations. The experimental results show that mixing among active neutrinos give dominant contributions to both the solar and atmospheric oscillations (see, e.g., ref. [76]). In particular, in figure 19 of ref. [76] we can see that at the 99% level $\eta_s \leq 0.25$ and $1 - \eta_s \leq 0.25$, which contradicts the unitarity condition $\sum_{j=1}^4 |U_{sj}|^2 = 1$. In fact the (2+2)-schemes are excluded at 5.1σ CL [76]. This conclusion is independent of whether we take the LSND data into consideration or not and we will not consider (2+2)-schemes in the rest of this paper.

2.2 (3+1)-schemes with the LSND constraint

On the other hand, (3+1)-schemes are not affected by the tension between the solar and atmospheric constraints on sterile neutrino oscillations, because as long as the mixing of sterile neutrino is small, then phenomenology of solar and atmospheric oscillations is approximately the same as that of the three flavor framework. The (3+1) schemes start having a problem only when one tries to account for LSND and all other negative results of the short baseline experiments. To explain the LSND data while satisfying the constraints from other disappearance experiments, the oscillation probabilities of the appearance and disappearance channels have to satisfy the following relation [77, 78]:

$$\sin^2 2\theta_{\text{LSND}}(\Delta m^2) < \frac{1}{4} \sin^2 2\theta_{\text{Bugey}}(\Delta m^2) \cdot \sin^2 2\theta_{\text{CDHSW}}(\Delta m^2) \quad (2.1)$$

where $\theta_{\text{LSND}}(\Delta m^2)$, $\theta_{\text{CDHSW}}(\Delta m^2)$, $\theta_{\text{Bugey}}(\Delta m^2)$ are the value of the effective two-flavor mixing angle as a function of the mass squared difference Δm^2 in the allowed region for LSND ($\bar{\nu}_\mu \rightarrow \bar{\nu}_e$), the CDHSW experiment [79] ($\nu_\mu \rightarrow \nu_\mu$), and the Bugey experiment [80] ($\bar{\nu}_e \rightarrow \bar{\nu}_e$), respectively. The reason that the (3+1)-scheme to explain LSND is disfavored is basically because eq. (2.1) is not satisfied for any value of Δm^2 . A (3+2)-scheme with two sterile neutrino has also been proposed [53] to account for LSND, and it may be possible to reconcile the LSND and MiniBooNE data by introducing a CP phase [54, 81]. Also in this case, however, tension with CDHSW [79] and Bugey [80] remains, as in the case of the (3+1)-scheme.

2.3 (3+1)-schemes without the LSND constraint

If we give up our effort to account for the LSND data, on the other hand, we no longer have the constraint (2.1). In this case we have only the upper bound on the extra mixing angles and this scenario satisfies all the experimental constraints (except that of LSND).

Throughout this work, therefore, we will consider a (3+1)-scheme without taking the LSND data into account while satisfying all the negative constraints, as it was done in ref. [60].

It has been discussed that the mixing angles of four neutrino schemes may be constrained by big-bang nucleosynthesis (see refs. [77, 82] and references therein), and if such arguments are applied, then the mixing angles of sterile neutrinos would have to be very small. However, it is known that in some model [83] neutrino oscillations themselves create large lepton asymmetries which prevent sterile neutrinos from being in thermal equilibrium, so it is not so clear whether the arguments in [77, 82] hold. At present, therefore, it is fair to say that there is not yet general consensus on this issue (see ref. [84] and references therein). In this paper we will not impose cosmological constraints on our scheme.

The mixing matrix U can be conveniently parametrized in terms of six independent rotation angles θ_{ij} and three (if neutrinos are Dirac fermions) or six (if neutrinos are Majorana fermions) phases δ_i . In oscillation experiments, only the so-called “Dirac phases” can be measured, since the “Majorana phases” appear only as an overall phase of the oscillation amplitude and disappear in the oscillation probability. The Majorana or Dirac nature of neutrinos can thus be tested only in $\Delta L = 2$ transitions such as neutrino-less double β -decay or lepton number violating decays [19]. In the following analysis, with no loss in generality, we will restrict ourselves to the case of 4 Dirac-type neutrinos only.

A generic rotation in a four-dimensional space can be obtained by performing six different rotations along the Euler axes. Since the ordering of the rotation matrices R_{ij} (where ij refers to the plane in which the rotation takes place) is arbitrary, plenty of different parametrizations of the mixing matrix U are allowed. In this paper we are interested in the so-called “atmospheric regime”, with oscillations driven by the atmospheric mass difference, $\Delta_{\text{atm}} = \Delta m_{\text{atm}}^2 L/2E \sim O(1)$. We will then make use of the following parametrization, adopted in ref. [54]:

$$U = R_{34}(\theta_{34}, 0) R_{24}(\theta_{24}, 0) R_{23}(\theta_{23}, \delta_3) R_{14}(\theta_{14}, 0) R_{13}(\theta_{13}, \delta_2) R_{12}(\theta_{12}, \delta_1). \quad (2.2)$$

In eq. (2.2), $R_{ij}(\theta_{ij}, \delta_i)$ are the complex rotation matrices in the ij -plane defined as:

$$[R_{ij}(\theta_{ij}, \delta_i)]_{pq} = \begin{cases} \cos \theta_{ij} & p = q = i, j \\ 1 & p = q \neq i, j \\ \sin \theta_{ij} e^{-i\delta_i} & p = i; q = j \\ -\sin \theta_{ij} e^{i\delta_i} & p = j; q = i \\ 0 & \text{otherwise.} \end{cases} \quad (2.3)$$

It is convenient to put phases in R_{12} (so that it automatically drops in the limit $\Delta_{\text{sol}} = \Delta m_{\text{sol}}^2 L/2E \rightarrow 0$) and R_{13} (so that it reduces to the “standard” three-family Dirac phase when sterile neutrinos are decoupled). The third phase can be put anywhere; we will place it in R_{23} . Note that in the one-mass dominance regime [85] (i.e. for $\Delta_{\text{atm}}, \Delta_{\text{sol}} \rightarrow 0$) all the phases automatically disappear from the oscillation probabilities for some choices of the four-family PMNS matrix parametrization.

The mixing matrix elements in the parametrization (2.2) are given in the appendix A.

This parametrization has been used in ref. [60] to put bounds on the active-sterile mixing angles θ_{i4} using existing data (including MiniBooNE but neglecting LSND). These bounds can be summarized as follows:

1. Bounds from ν_e disappearance reactor experiments

Reactor experiments such as Bugey and Chooz can put stringent bounds on θ_{13} and θ_{14} in this parametrization: $\theta_{13} \leq 13^\circ$ and $\theta_{14} \leq 10^\circ$ at 99% CL, for any value of $\Delta m_{\text{SBL}}^2 > 0.1 \text{ eV}^2$, with some correlation between the two (in particular the four-family Chooz bound on θ_{13} is slightly modulated by θ_{14}).

2. Bounds from ν_μ disappearance experiments

A “negative” result in a ν_μ disappearance experiment at ”atmospheric” L/E (such as K2K or MINOS), in which ν_μ oscillations can be very well fitted in terms of three-family oscillations, puts a stringent bound on the mixing angle θ_{24} . The bound from such experiments found in ref. [60] is: $\theta_{24} \leq 14^\circ$ at 99% CL, for $\Delta m_{\text{SBL}}^2 \geq 0.1 \text{ eV}^2$.

3. Bounds on θ_{34}

Neither ν_e nor ν_μ disappearance probabilities in vacuum depend strongly on θ_{34} (as it can be seen in ref. [60]). An upper bound on θ_{34} , however, can be drawn as the result of indirect searches for $\nu_\mu \rightarrow \nu_s$ conversion in atmospheric neutrino experiments, that take advantage of the different interaction with matter of active and sterile neutrinos. Present bounds on θ_{34} arise, thus, from a measurement of spectral distortion. On the other hand, bounds on θ_{13}, θ_{14} and θ_{24} are mainly drawn by a flux normalization measurement. As a consequence, the bound on θ_{34} that we can draw by non-observation of $\nu_\mu \rightarrow \nu_s$ oscillation in atmospheric experiments is less stringent than those we have shown before. For this reason, θ_{34} can be somewhat larger than θ_{13}, θ_{14} and θ_{24} : $\theta_{34} \leq 32^\circ$ at 99% CL.

These bounds are depicted in figure 2 of ref. [60], where 90%, 95%, 99% and 3σ CL contours in the $(\theta_{13} - \theta_{14})$ - and $(\theta_{24} - \theta_{34})$ -planes are shown for $\Delta_{\text{sol}} \rightarrow 0$ and $\Delta m_{\text{atm}}^2 = 2.4 \times 10^{-3} \text{ eV}^2$ and $\theta_{23} = 45^\circ$.

2.4 Oscillation probabilities at the Neutrino Factory in the (3+1)-scheme

To understand the details of the different channels with the greatest sensitivity to the four-family neutrino schemes, it is useful to obtain simple analytical expressions for the different channels in matter. Hereafter, we will assume a constant Earth density along the neutrino path, computed using the PREM [86]. Notice that, in the framework of Neutrino Factory experiments simulations, the impact of non-constant matter density has been thoroughly studied, showing that for the baselines and the muon energy considered in this paper the details of the density profile crossed by neutrinos does not modify the results.³

³This is totally different, for example, in the case of β -Beams with Li/B decaying ions. In those setups, a resonance is crossed for $O(5 \text{ GeV})$ neutrinos for $L = O(10000) \text{ km}$ baselines [87].

To derive the oscillation probabilities, we adopt the KTY formalism [62, 63] (the details are given in the appendix B). Furthermore, to get simplified forms of the formulæ, it is convenient to obtain the probabilities expanding with respect to the following small parameters:

$$\epsilon \equiv \theta_{34} \sim \sqrt{\theta_{13}} \sim \sqrt{\theta_{14}} \sim \sqrt{\theta_{24}} \sim \sqrt{\delta\theta_{23}} \lesssim 4 \times 10^{-1},$$

with $\delta\theta_{23} = \theta_{23} - \pi/4$.

The relevant oscillation probabilities in matter, expanded to third order in ϵ , are given by

$$P_{ee} \sim 1 + O(\epsilon^4), \tag{2.4}$$

$$P_{e\mu} \sim P_{e\tau} \sim P_{es} \sim O(\epsilon^4), \tag{2.5}$$

$$P_{\mu\mu} = 1 - \sin^2 \frac{\Delta_{31}L}{2} - 2(A_n L) s_{24} s_{34} \cos \delta_3 \sin \Delta_{31}L + O(\epsilon^4), \tag{2.6}$$

$$P_{\mu\tau} = (1 - s_{34}^2) \sin^2 \frac{\Delta_{31}L}{2} + \{s_{24} s_{34} \sin \delta_3 + 2(A_n L) s_{24} s_{34} \cos \delta_3\} \sin \Delta_{31}L + O(\epsilon^4), \tag{2.7}$$

$$P_{\mu s} = s_{34}^2 \sin^2 \frac{\Delta_{31}L}{2} - s_{24} s_{34} \sin \delta_3 \sin \Delta_{31}L + O(\epsilon^4), \tag{2.8}$$

where $\Delta_{31} = \Delta m_{31}^2/2E$, and we take the convention that the central value of $|\Delta m_{31}^2|$ is Δm_{atm}^2 , which is determined by the two flavor analysis of the atmospheric neutrino data. The matter density parameter A_n is $A_n = \sqrt{2}G_F n_n/2$. Notice that at $O(\epsilon^3)$ the expansion parameter $\delta\theta_{23}$ is not present in the oscillation probabilities (it only arises at the next order in ϵ).

From eqs. (2.4)–(2.8), it can be easily verified that unitarity of the PMNS matrix is satisfied to this order in ϵ . As it can be seen, moreover, the ν_e decouples within this approximation. We can thus conclude that the "classic" Neutrino Factory channels, such as the "golden channel" $\nu_e \rightarrow \nu_\mu$ and the "silver channel" $\nu_e \rightarrow \nu_\tau$, are of limited interest to study sterile neutrinos, as we will see later in the numerical analysis.⁴ Leading sensitivity to θ_{34} is provided by the first term in $P_{\mu\tau}$, eq. (2.7), that is proportional to $(1 - s_{34}^2)$. Sensitivity to θ_{24} is best achieved using the $\nu_\mu \rightarrow \nu_\mu$ oscillations, though the relevant term appears at $O(\epsilon^4)$, as it will be shown in section 4.2. In eqs. (2.6)–(2.7) we can also see that combined sensitivity to θ_{24} and θ_{34} is achievable through the $O(\epsilon^3)$ matter-dependent $s_{24}s_{34} \cos \delta_3$ term in $P_{\mu\mu}, P_{\mu\tau}$. The bounds on these two angles are those that can be improved the most by the Neutrino Factory experiments. We can thus safely say that the ν_μ disappearance channel and the $\nu_\mu \rightarrow \nu_\tau$ appearance channel are the most relevant signals to look for sterile neutrinos. This will be confirmed by the numerical analysis later.

Notice that θ_{34} is considerably less constrained than the rest of the new angles (which are as constrained as θ_{13}). Therefore, the $\nu_\mu \rightarrow \nu_\tau$ channel would have at the theoretical level the strongest sensitivity to sterile neutrino parameter space: $P_{\mu\tau}$ is the only one (with the exception of $P_{\mu s}$, that cannot be directly measured) that is of $O(\epsilon^2)$ in the

⁴ This has been known since long. See for example refs. [60, 64, 65].

expansion parameters. Moreover, $\nu_\mu \rightarrow \nu_\tau$ can also look for CP-violating signals in four-family scenarios through the $O(\epsilon^3)$ matter-independent $s_{24}s_{34} \sin \delta_3$ term, something out of the reach of the ν_μ disappearance channel (that can only measure δ_3 through CP-conserving signals).

As it is well known, τ -detection experiments are extremely difficult at the experimental level. If the experimental problems could be overcome, $\nu_\mu \rightarrow \nu_\tau$ would be the important channel to study sterile neutrinos as well as other kinds of new physics, such as the non-standard interactions [44, 45], or unitarity violations [46, 47]. In particular, if CP violation occurs due to these new physics, then the $\nu_\mu \rightarrow \nu_\tau$ channel is quite powerful in measuring the new CP-violating phases. For this reason, we will name it throughout this paper as "the discovery channel".

Notice that the $\nu_\mu \rightarrow \nu_\tau$ channel has not been studied in detail yet in the framework of neutrino factories studies (with the possible exceptions of refs. [88, 89]).

3 The Neutrino Factory and the Hybrid-MIND detector

In a Neutrino Factory [34, 90] muons are first produced with a multi-MW proton source, accelerated up to energies of several GeV's, and finally injected into a storage ring with long straight sections aiming to one or more detectors. The muon decays $\mu^+ \rightarrow e^+ \nu_e \bar{\nu}_\mu$ and $\mu^- \rightarrow e^- \bar{\nu}_e \nu_\mu$ provide a very well known two-flavor neutrino flux [91] with energies in the range $E_\nu \in [0, E_\mu]$. Neutrino Factory designs have been proposed in Europe [92, 93], the US [94–97], and Japan [98]. The dedicated *International Scoping Study for a future Neutrino Factory and Super-Beam facility* [43] showed that, provided sufficient resources, an accelerator complex capable of providing about 10^{21} muon decays of a given polarity per year can be built.

The Neutrino Factory setup that we propose for sterile neutrinos searches and that we examine in detail in the rest of the paper is defined as follows: muons of both polarities are accelerated up to $E_\mu = 50$ GeV and injected into one storage ring with a geometry that allows to aim at two far detectors, the first located at 3000 km and the second at 7500 km from the source. An alternative option, considered in the final ISS Accelerator Report [99], is to inject the muon beam into different storage rings, each of them aimed to a single far detector. The number of useful muon decays per year aimed at each detector has been fixed to 2×10^{20} . This number is rather conservative since, in the final ISS Physics Report [43], with a similar storage ring(s) geometry, 5×10^{20} useful muon decays per year aimed at each detector are considered (i.e., 10^{21} total useful muon decays per year). Four years of data taking for each muon polarity are envisaged.

The Neutrino Factory fluxes (for μ^- accumulated in the storage ring) at $L = 3000$ km as a function of the neutrino energy for $E_\mu = 50$ GeV are shown in figure 2(left). Two detectors of different technologies have been considered to detect the ν_μ and ν_τ signals. The first one is a magnetized iron calorimeter [102], that was proposed with a slightly different design in ref. [103] to measure the "golden" $\nu_e \rightarrow \nu_\mu$ wrong-sign muons signal. The second detector is a Magnetized Emulsion Cloud Chamber (MECC) [66], an evolution of the ECC modeled after OPERA that was first considered for Neutrino Factory studies

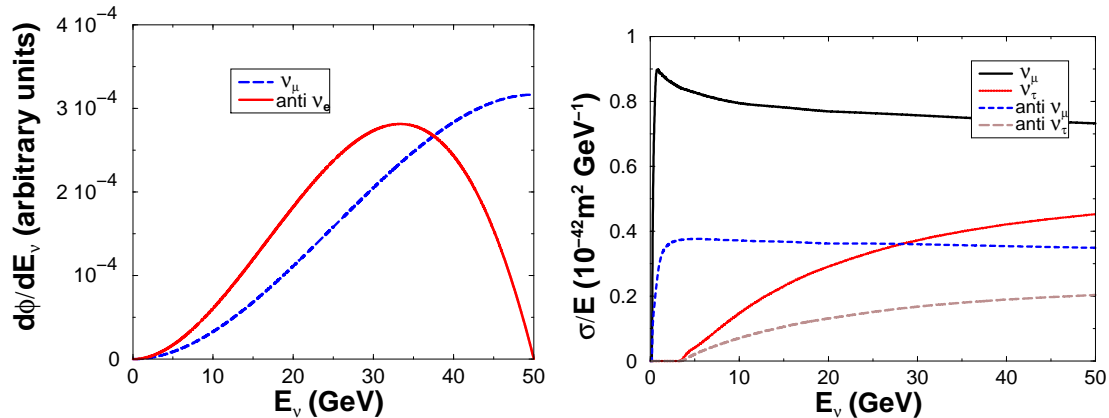


Figure 2. Left: 50 GeV Neutrino Factory fluxes at $L = 3000$ km; Right: the $\nu_\mu N$ and $\nu_\tau N$ cross-sections on iron [100, 101].

in refs. [68, 104] to look for the "silver channel" $\nu_e \rightarrow \nu_\tau$ (a channel that can be looked at only in a Neutrino Factory setup).

The $\nu_\mu N$ and $\nu_\tau N$ cross-sections on iron as a function of the neutrino energy for both neutrinos and anti-neutrinos are shown in figure 2 (right).

Notice that the adopted setup, similar to those proposed in the first Neutrino Factory studies (see, for example, refs. [67, 69]), slightly differs from the setup that was suggested in the final ISS Physics Report. The latter consists in stored muons with energies in the range $E_\mu \in [20, 30]$ GeV, aiming to two detectors located at $L = 4000$ km and $L = 7500$ km from the source. The longest baseline corresponds to the so-called "magic baseline" [105], where three-family CP-violating effects vanish. We have chosen the same baseline for the far detector in our setup, although in the (3+1)-neutrino model not all of the CP-violating phases dependence decouple at this distance (as it can be seen from eqs. (2.6), (2.7) and in section 4). The shortest baseline was optimized in the ISS Physics Report to look for CP-violating three-family signals, finding that a detector with a baseline of $L = 4000$ km performed slightly better than at $L = 3000$ km. This optimization, however, is no longer valid when looking for the (3+1)-neutrino model signals. We decided, therefore, to adopt the $L = 3000$ km baseline used in previous studies, for which possible sites have already been explored.⁵ Eventually, we use a stored muon energy that is larger than the optimal value adopted in the ISS Physics Report, again chosen to maximize the sensitivity to three-family observables such as θ_{13} , the sign of the atmospheric mass difference and the three-family CP-violating phase δ . It is indeed well known from previous studies (see, for example, ref. [106] for an optimization of the muon energy to look for NSI signals at the Neutrino Factory) that to look for new physics the higher the muon energy the better. An evident motivation for this is that the $\nu_\mu \rightarrow \nu_\tau$ channel is very important to look for new physics in neutrino oscillations, and high neutrino energies are required to circumvent the extremely low $\nu_\tau N$ cross-section in the tens of GeV energy range (see figure 2, right).

⁵For example, the island of La Palma in the Canary Islands, the island of Longyearbyen in Norway or the Oulu mine in Pyhösalmi in Finland are possible options for the location of a detector at approximately 3000 km from the source for a CERN-based Neutrino Factory.

To show that the 50 GeV Neutrino Factory setup proposed above is more suited to look for sterile neutrino signals, we will compare our results with an ISS-inspired Neutrino Factory, defined as follows: muons of both polarities are accelerated up to $E_\mu = 20$ GeV and injected into storage ring(s) with a geometry that allows to aim at two far detectors, the first located at 4000 km and the second at 7500 km from the source. The number of useful muon decays per year aimed at each detector has been fixed in this case to 5×10^{20} , following the final ISS Physics Report [43]. Four years of data taking for each muon polarity are envisaged. When studying the performance of the ISS-inspired 20 GeV setup, we consider the same detectors as in the case of the 50 GeV Neutrino Factory.

3.1 The MIND detector: $\nu_e \rightarrow \nu_\mu$ and $\nu_\mu \rightarrow \nu_\mu$

The baseline detector, a 50 kton magnetized iron calorimeter of the MINOS type, was originally optimized to reduce the background to the wrong-sign muon signal for $\nu_e \rightarrow \nu_\mu$ oscillations (represented dominantly by right-sign muons with a wrong charge assignment and charmed meson decays) to the 10^{-6} level. To achieve this extremely ambitious signal-to-background ratio, tight kinematical cuts were applied. Such cuts, although strongly reducing the background, have the disadvantage of an important suppression of the signal below 10 GeV, an energy region that, on the other hand, has been shown to be extremely important. A non-negligible signal below and above the first oscillation peak (that, for $L \sim 3000$ km, lies precisely in this energy range) is crucial to solve many of the parametric degeneracies [69, 70, 107, 108] that bother the three-family (θ_{13}, δ)-measurement. To reduce such problems, a modification of the original detector proposal called MIND (Magnetized Iron Neutrino Detector) was presented in ref. [102].

Studies of the four-family $\nu_e \rightarrow \nu_\mu$ oscillation (still the best channel to measure θ_{13}) are not different from those performed in the framework of the three-family model. In particular, no new sources of background are expected. Quite the contrary, those backgrounds induced by wrongly reconstructed $\bar{\nu}_\mu$ are expected to decrease for large values of θ_{34} , due to the increased oscillation into sterile neutrinos, see eq. (2.8). When looking at $\nu_e \rightarrow \nu_\mu$ oscillations, we will therefore take advantage of the wrong-sign muon identification efficiency presented in the ISS Detector Report [66]: $\epsilon_{e\mu} = 0.7$ above 10 GeV, with the efficiency increasing linearly from $\epsilon_{e\mu} = 0.1$ at 1 GeV.

The MIND detector can also be used to look for $\nu_\mu \rightarrow \nu_\mu$ disappearance (one of the channels of interest to study sterile neutrino models), providing a very good measurement of the atmospheric parameters θ_{23} and Δm_{atm}^2 and giving some handle to solve the “octant degeneracy” (see, e.g., ref. [88, 109]). For the right-sign muon sample there is no need to accurately tell the charge of the muon, since the background induced by misidentified wrong-signs muons is negligible with respect to the signal, [110]. We can safely use for this signal the muon identification efficiency of the MINOS experiment [111]: $\epsilon_{\mu\mu} = 0.9$ above 1 GeV. Notice that at the MIND detector it is not possible to single out τ 's decaying to muons. We cannot thus use MIND to study the leading $\nu_\mu \rightarrow \nu_\tau$ oscillation and the “silver” $\nu_e \rightarrow \nu_\tau$ channel.

We have considered as background for the ν_μ disappearance channel 10^{-5} of all neutral current events, *all* wrong-sign muon events and the right-sign muons coming from $\nu_\mu \rightarrow \nu_\tau$

oscillation with τ decaying into muons. The inclusion of this background has no effect on our results for this channel, that are remarkably systematic-dominated.

Different treatments of the energy response of the detector can be found. For example, in ref. [67] a constant energy resolution $\Delta E_\nu = 0.2E_\mu$ was considered, by grouping events in five bins of energy width $\Delta E_\nu = 10$ GeV. On the other hand, in ref. [112] a finer binning was adopted, with a more refined treatment of the energy resolution: 43 bins of variable ΔE_ν were considered in the energy range $E_\nu \in [1\text{GeV}, E_\mu]$, folding the event distribution with a Gaussian resolution kernel of variable width, $\sigma_E = 0.15 \times E_\nu$. In this paper we have followed the first approach, grouping events into 10 constant energy resolution bins with $\Delta E_\nu = 0.1E_\mu$, leaving possible improvements of the detector simulation following ref. [112] (if needed) for future publications.

Throughout our numerical simulations we have assumed 2% and 5% for the bin-to-bin uncorrelated systematic errors on the golden channel and on the ν_μ disappearance signal. We have also assumed 1% and 5% for normalization and energy spectrum distortion as the correlated systematic errors for all the channels.⁶ The dependence of the sensitivities on the systematic errors will be discussed in section 4.4.

Notice that a different proposal for a magnetized iron calorimeter that can be used for a Neutrino Factory experiment has been advanced in ref. [113].

3.2 The MECC detector: $\nu_e \rightarrow \nu_\tau$ and $\nu_\mu \rightarrow \nu_\tau$

Two technologies were considered in the literature to study neutrino oscillations into τ 's: Liquid Argon detectors [88, 89] and Emulsion Cloud Chamber techniques. In both cases, the $\nu_e, \nu_\mu \rightarrow \nu_\tau$ signal can be tagged looking for right-sign muons in coincidence with a τ decay vertex, to distinguish them from ν_μ disappearance muons. Therefore, a detector with muon charge identification and vertex reconstruction is needed.

A dedicated analysis to use an ECC modeled after OPERA at the Neutrino Factory to look for the "silver channel" $\nu_e \rightarrow \nu_\tau$ [68] has been published in ref. [104]. In that reference, a 5 kton ECC was considered, with a detailed study of the main sources of background.

The result of that analysis was that τ 's can be identified with a very low background, at the price of a very low efficiency, $O(5\%)$. One of the main motivation of such low efficiency was that only the $\tau \rightarrow \mu$ decay channel was used, i.e. only 17% of the total amount of produced τ 's. In the OPERA detector used at the CNGS and in the analysis of ref. [104], the τ charge identification is achieved using two large spectrometers located at the end of two thick active sections, with bricks made of repeated layers of lead (acting as the target for $\nu_\tau N$ interactions) and emulsions. In the Magnetized ECC (MECC) proposal [66] the lead plates are replaced by iron plates, again interleaved with emulsions layers. The ECC can be, thus, directly magnetized through the iron plates. Emulsion spectrometers (currently in their test phase, [114]) are located at the end of the ECC section. Eventually, the MECC is placed in front of the MIND detector, to form the so-called Hybrid-MIND

⁶ In principle, some of the correlated systematic errors could be common among the different channels (such as the detector volume uncertainty) or different baselines (such as the cross section uncertainty), but for simplicity we assume here that all the correlated systematic errors are independent among the different channels or different baselines. The results in the present paper may be, therefore, somewhat conservative.

setup. The efficiency of this detector to τ 's is much higher than in the case of the standard ECC, since τ decay into electrons and into hadrons can be used in addition to $\tau \rightarrow \mu$ decays. The expected efficiency is, thus, approximately five times larger than in the case of the ECC (see, for example, refs. [66, 115] and refs. therein).

The MECC bricks are bigger than the corresponding ECC ones, due to the replacement of the lead target with iron. The huge volume to be magnetized put, thus, a tight limit on the maximum foreseeable detector mass. We will therefore consider throughout the paper a 4 kton MECC [116] located in front of the 50 kton MIND, and use this detector to study both the silver channel $\nu_e \rightarrow \nu_\tau$ and the novel "discovery channel" $\nu_\mu \rightarrow \nu_\tau$. For the silver channel signal, we will use an energy dependent efficiency $\epsilon_{e\tau}$ taken from ref. [104], multiplying it by a factor five to take into account that all τ 's decay channel can be used at the MECC. A detailed study of the efficiency to the $\nu_\mu \rightarrow \nu_\tau$ channel at the MECC, on the other hand, is lacking. We will therefore assume a constant efficiency $\epsilon_{\mu\tau} = 0.65$ above 5 GeV, increasing by a factor five the efficiency considered in ref. [60]. This assumption must be checked in further studies of the MECC-type detectors exposed to a Neutrino Factory beam.

The backgrounds for the silver and the discovery channels should be also correspondingly increased at the MECC with respect to the ECC ones. At the ECC, the expected signal-to-background ratio (after some kinematical cuts) for $\nu_\mu \rightarrow \nu_\tau$ (using the $\tau \rightarrow \mu$ decay channel, only) is 50:1 or larger [60], the dominant source of background for the process $\nu_\mu \rightarrow \nu_\tau \rightarrow \tau^- \rightarrow \mu^-$ being represented by non-oscillated muons that produce charmed mesons eventually decaying into μ^- either through NC or CC in which the muon is not observed. No detailed study of the expected background for the $\nu_e \rightarrow \nu_\tau$ or the $\nu_\mu \rightarrow \nu_\tau$ signals at the MECC exposed to a Neutrino Factory beam has been performed yet, though. We have thus decided to make the assumption that, using MECC, all τ decay channels should be affected by similar backgrounds. We have therefore consistently multiplied the backgrounds for $\nu_e \rightarrow \nu_\tau$ and $\nu_\mu \rightarrow \nu_\tau$ computed in refs. [60, 104] by a factor five. This is possibly a conservative assumption,⁷ since the MECC is expected to have a signal-to-background ratio for this signal slightly better than the ECC [117]. We consider, however, this to be the only reasonable choice that we can take at this preliminary stage of four-family neutrino detailed study at the Neutrino Factory (not to be compared with the order-of-magnitude estimations made in previous papers).

Also in this case, we have grouped events into 10 bins with $\Delta E_\nu = 5$ GeV constant energy resolution. We have assumed 10% for the bin-to-bin uncorrelated systematic errors, 1% and 5% for normalization and energy spectrum distorsion as the correlated systematic errors throughout the numerical simulations for both the $\nu_e \rightarrow \nu_\tau$ and the $\nu_\mu \rightarrow \nu_\tau$ signals. Once again, the results here may be slightly conservative because we may be overcounting the systematic errors. In table 1 we show the expected number of τ^- from $\nu_\mu \rightarrow \nu_\tau$

⁷ Notice that, for the silver channel, at least the background induced by right-sign τ 's with wrong charge assignment should be depleted in a four-family neutrino scenario with respect to the standard three-family one. This particular background is strongly affected by active-sterile mixing angles, since, in the allowed region of the parameter space, $\nu_\mu \rightarrow \nu_\tau$ oscillations are significantly depleted with respect to the standard three-neutrino ones.

$(\theta_{13}; \theta_{14}; \theta_{24}; \theta_{34})$	$N_{\tau^-}^{CNGS}$	$N_{\tau^-}^{3000}$	$N_{\tau^+}^{3000}$	$N_{\tau^-}^{7500}$	$N_{\tau^+}^{7500}$
$(5^\circ; 5^\circ; 5^\circ; 20^\circ)$	8.9	559	10	544	2
$(5^\circ; 10^\circ; 5^\circ; 20^\circ)$		557	29	544	5
$(5^\circ; 5^\circ; 10^\circ; 20^\circ)$	8.3	474	11	529	2
$(5^\circ; 5^\circ; 10^\circ; 30^\circ)$	10.5	384	18	454	3
$(5^\circ; 10^\circ; 5^\circ; 30^\circ)$		424	59	441	11
$(5^\circ; 5^\circ; 10^\circ; 30^\circ)$	10.5	384	18	454	3
$(10^\circ; 5^\circ; 5^\circ; 20^\circ)$	8.5	522	22	512	2
$(10^\circ; 10^\circ; 5^\circ; 20^\circ)$		517	42	510	6
$(10^\circ; 5^\circ; 10^\circ; 20^\circ)$	7.9	443	22	498	2
$(10^\circ; 5^\circ; 5^\circ; 30^\circ)$	6.5	397	30	413	4
$(10^\circ; 10^\circ; 5^\circ; 30^\circ)$		389	74	412	11
$(10^\circ; 5^\circ; 10^\circ; 30^\circ)$	10.3	361	30	428	4
3 families, $\theta_{13} = 5^\circ$	15.1	797	3	666	0
3 families, $\theta_{13} = 10^\circ$	14.4	755	12	632	1

Table 1. Event rates for the $\nu_\mu \rightarrow \nu_\tau$ and $\bar{\nu}_e \rightarrow \bar{\nu}_\tau$ channels for 1 kton MECC detector, exposed to a 2×10^{20} ($\nu_\mu, \bar{\nu}_e$) flux for one year, for different values of θ_{14}, θ_{24} and θ_{34} in the (3+1) scheme. The other unknown angle, θ_{13} has been fixed to: $\theta_{13} = 5^\circ, 10^\circ$. The CP-violating phases are: $\delta_1 = \delta_2 = 0; \delta_3 = 90^\circ$. As a reference, rates at the 1.8 kton OPERA detector (exposed to the nominal CNGS beam intensity) and the expected event rates for 1 kton MECC detector in the case of the three-family model (i.e., for $\theta_{i4} = 0$ and maximal CP-violating phase δ) are also shown. In all cases, perfect efficiency is assumed.

and τ^+ from $\bar{\nu}_e \rightarrow \bar{\nu}_\tau$ for a 1 kton MECC detector with perfect efficiency, exposed to a 2×10^{20} ($\nu_\mu, \bar{\nu}_e$) flux for one year, for different values of $\theta_{13}, \theta_{14}, \theta_{24}$ and θ_{34} . The other parameters are: $\theta_{12} = 34^\circ; \theta_{23} = 45^\circ; \Delta m_{\text{sol}}^2 = 7.9 \times 10^{-5} \text{ eV}^2; \Delta m_{\text{atm}}^2 = 2.4 \times 10^{-3} \text{ eV}^2$ and $\Delta m_{\text{SBL}}^2 = 1 \text{ eV}^2$ (all mass differences are taken to be positive). Eventually, phases have been fixed to: $\delta_1 = \delta_2 = 0; \delta_3 = 90^\circ$. For comparison, the rates at the CNGS (for the nominal CNGS flux, of 4.5×10^{19} pot/year, an active lead target mass of 1.8 kton and 5 years of data taking) and the expected number of events in the three-family model for a 1 kton MECC detector with perfect efficiency are also shown. We can see that the number of expected τ^- events at the 1 Kton MECC is $O(500)$ at both baselines, with some dependence on the different mixing angles. The fact that at both baselines we expect a similar number of events is a consequence of the convolution of the $\nu_\mu \rightarrow \nu_\tau$ oscillation probability with the $\nu_\tau N$ cross-section and the ν_μ neutrino flux: at the shortest baseline, the probability is maximal below 10 GeV; at the longest baseline, the maximum is located in the 30 GeV bin. The higher cross-section for this energy bin compensates for the decrease in the ν_μ neutrino flux, thus giving a similar number of τ 's in the detector.

Notice that we will not use the MECC section of the Hybrid-MIND detector to look for the golden $\nu_e \rightarrow \nu_\mu$ and the $\nu_\mu \rightarrow \nu_\mu$ disappearance signals. Both channels can be studied, though, at the price of an increase in the scanning load.

4 Sensitivity to (3 + 1) sterile neutrinos at the Neutrino Factory

In this section we study the physics reach of the 50 GeV Neutrino Factory setup discussed in the previous section to (3+1)-model sterile neutrinos. We will make use of all possible oscillation channels available at this setup, namely the golden channel $\nu_e \rightarrow \nu_\mu$ and the disappearance channel $\nu_\mu \rightarrow \nu_\mu$ using the MIND section of the detector; the silver channel $\nu_e \rightarrow \nu_\tau$ and the "discovery channel" $\nu_\mu \rightarrow \nu_\tau$ using the MECC section of the detector.

In section 4.1 and 4.2 we study how a negative result at the Neutrino Factory can be used to improve present bounds on the four-family model $\theta_{13}^{(4\text{fam})}$, extending the standard three-family θ_{13} -sensitivity analysis, and on the three active-sterile mixing angles θ_{14}, θ_{24} and θ_{34} . In particular, the golden and silver channels ($\nu_e \rightarrow \nu_\mu, \nu_\tau$) cooperate to put a strong bound on $\theta_{13}^{(4\text{fam})}$ (see section. 4.1). On the other hand, the ν_μ disappearance channel and the "discovery channel" $\nu_\mu \rightarrow \nu_\tau$ improve significantly the exclusion bounds for (3+1)-sterile neutrinos in the $(\theta_{24}, \theta_{34})$ plane (see section 4.2). Preliminary results for the combination of these two channels at a 50 GeV Neutrino Factory setup have been presented in refs. [118, 119].

In section 4.3 we consider a different situation: in the case of a positive signal at the Neutrino Factory, can we discriminate between the (3+1)-sterile neutrino model and the "standard" three-family one? We will show that, using the combination of the four available channels, we can indeed discriminate between the two models in a significant region of the active-sterile mixing angles parameter space. In sections 4.1, 4.2 and 4.3 we will also compare our results with those that could be obtained using the 20 GeV ISS-inspired Neutrino Factory defined in section 3.

In section 4.4 we discuss the dependence of the four channels on the systematic errors. It is known that the golden and silver channels are dominated by the statistical errors. We will show, on the other hand, that both the disappearance and discovery channels are dominated by the systematic errors, emphasizing that improvement on systematic errors is extremely important to take full advantage of the discovery channel.

In case a positive signal is found, it is interesting to study the various CP-violating signals. This is done in section 4.5, where we show the attainable precision in the simultaneous measurement of θ_{34} and of the CP-violating phase δ_3 and the δ_3 -discovery potential, when both active-sterile mixing angles θ_{24} and θ_{34} are not exceedingly small. We also show how the measurement of the three-family-like CP-violating phase δ_2 is modified by the presence of non-vanishing active-sterile mixing angles.

4.1 Sensitivity to $(\theta_{13}, \theta_{14})$

In this subsection first we discuss sensitivity to $(\theta_{13}, \theta_{14})$ at the Neutrino Factory. As we will see below, sensitivity to θ_{14} turns out to be poor. So we will consider sensitivity to other combinations of the mixing matrix elements later.

4.1.1 Sensitivity to $(\theta_{13}, \theta_{14})$

The sensitivity is defined as follows: we first compute the expected number of events for $\nu_e \rightarrow \nu_\mu$ and $\nu_e \rightarrow \nu_\tau$ oscillations for the input values $\theta_{13}^{(4\text{fam})} = 0$, and $\theta_{14} = \theta_{24} = \theta_{34} = 0$,

where $\theta_{jk}^{(4\text{fam})}$ ($(j, k) = (1, 2), (1, 3), (2, 3)$) and $\theta_{j4} \equiv \theta_{j4}^{(4\text{fam})}$ stand for the mixing angles in the four-family scheme denoted by (4fam).⁸ This number, that is identical in the three- and four-family models, is labeled as N^0 . We then compute the expected number of events in the $(\theta_{13}^{(4\text{fam})}, \theta_{14})$ -plane for the same oscillation channels in the four-family model. The $\Delta\chi^2$, computed with respect to the "true" value N^0 , is eventually evaluated. The contour for which the 2 d.o.f.'s $\Delta\chi^2$ is $\Delta\chi^2 = 4.61$ defines, then, the region of the parameter space of the (3+1)-sterile neutrino model that is non-compatible at 90% CL with the input data corresponding to vanishing $(\theta_{13}^{(4\text{fam})}, \theta_{14})$ (to the right of the contour line) and the region that it is still allowed (to the left of the line) at this CL.

The minimum of the χ^2 is computed as follows:

$$\begin{aligned} \Delta\chi^2 = \min_{\text{marg par}} \left[\sum_{\text{pol.}, (\text{chan.}), (L)} \min_{\alpha'_s, \beta'_s} \left\{ \sum_j \frac{1}{\sigma_j^2} \left((1 + \alpha_s + x_j \beta_s) N_j(4\text{fam}) \right. \right. \right. \\ \left. \left. \left. + (1 + \alpha_b + x_j \beta_b) B_j(4\text{fam}) - N_j^0 - B_j^0 \right)^2 + \left(\frac{\alpha_s}{\sigma_{\alpha_s}} \right)^2 + \left(\frac{\alpha_b}{\sigma_{\alpha_b}} \right)^2 \right. \right. \\ \left. \left. + \left(\frac{\beta_s}{\sigma_{\beta_s}} \right)^2 + \left(\frac{\beta_b}{\sigma_{\beta_b}} \right)^2 \right\} + \Delta\chi_{\text{atm+re}}^2(4\text{fam}) \right], \end{aligned} \quad (4.1)$$

where we have introduced the prior that comes from the four-family analysis of the atmospheric and reactor data:⁹

$$\begin{aligned} \Delta\chi_{\text{atm+re}}^2(4\text{fam}) = \frac{(s_{23}^2(4\text{fam}) - 0.50)^2}{\sigma^2(s_{23}^2)} + \frac{(|\Delta m_{32}^2(4\text{fam})| - 2.4 \times 10^{-3} \text{eV}^2)^2}{\sigma^2(|\Delta m_{32}^2(4\text{fam})|)} \\ + \frac{(s_{13}^2(4\text{fam}) - 0.01)^2}{\sigma^2(s_{13}^2)} + \frac{(s_{14}^2)^2}{\sigma^2(s_{14}^2)} + \frac{(s_{24}^2)^2}{\sigma^2(s_{24}^2)} + \frac{(s_{34}^2)^2}{\sigma^2(s_{34}^2)}. \end{aligned} \quad (4.2)$$

where $|\Delta m_{32}^2(4\text{fam})|$ stands for the atmospheric mass squared difference in the four-family scheme, and the errors of the oscillation parameters in the four-flavor scheme in eq. (4.2) are deduced from refs. [24] and [60] as follows:

$$\begin{aligned} \sigma(s_{23}^2) = 0.07, \quad \sigma(|\Delta m_{32}^2|) = 0.12 \times 10^{-3} \text{eV}^2, \quad \sigma(s_{13}^2) = 0.016, \\ \sigma(s_{14}^2) = 0.013, \quad \sigma(s_{24}^2) = 0.02, \quad \sigma(s_{34}^2) = 0.12. \end{aligned} \quad (4.3)$$

In the minimization procedure in eq. (4.1), "marg par" stands for the oscillation parameters to be marginalized over (that can be different for different plots), and $\alpha_s, \alpha_b, \beta_s$ and β_b are the variables for the correlated systematic errors, which stand for the uncertainties in the overall normalization and in the linear distortion in the spectral shape in the magnitude of signal (s) or background (b) [121], where we have defined $x_j \equiv E_j / (E_{\text{max}} - E_{\text{min}})$ for

⁸ Using the four-family expressions for the oscillation probabilities in vacuum shown in ref. [60], it can be seen that, for vanishing θ_{14} and θ_{24} , the four-family mixing angle $\theta_{13}^{(4\text{fam})}$ maps into the three-family one, $\theta_{13}^{(3\text{fam})}$. On the other hand, for non-vanishing θ_{14} , the four-family parameter is expected to be slightly smaller than the three-family one.

⁹ Since $\Delta\chi^2$ is expected to depend little on the solar neutrino oscillation parameters, we will not vary the solar oscillation parameters throughout this paper, so we omit the terms on the solar parameters here.

neutrino energy E_j for the j -th bin. Following ref. [121], we assume the correlated systematic errors $\sigma_{\alpha_s} = \sigma_{\alpha_b} = 0.01$ for the normalization and $\sigma_{\beta_s} = \sigma_{\beta_b} = 0.05$ for the spectrum distortion. In the analysis of the case with single baseline length, we have minimized the χ^2 for each baseline separately, i.e., no sum is performed over L , and in the analysis combining the two baselines, we have minimized the sum of χ^2 for each baseline. Similarly, in the analysis of a single channel, no sum is performed over the channels (“chan.”), while in the analysis combining the different channels we have summed over the different channels, i.e., golden and silver in this section. In all cases we sum up χ^2 for the two possible stored muon polarities (“pol.”). The index j runs over 10 energy bins. B_j is the background correspondent to the j -th bin (B_j^0 stands for the expected background in the four-family model for vanishing $\theta_{13}^{(4fam)}$ and θ_{14} in the j -th bin). Within this procedure, for any minimization that we perform the best-fit for the variables on which we marginalize over can be different. However, when we project onto the two-dimensional $(\theta_{13}^{(4fam)}, \theta_{14})$ -plane (or onto the $(\theta_{24}, \theta_{34})$ -plane in the next section) this information is lost. Notice that this approach is analogous to that used in the three-flavor analysis in ref. [120]. A final comment is in order: in the case of a real experiment, the minimum of the χ^2 distribution will in general not correspond exactly to the “true” values of the parameters to be fitted. The $\Delta\chi^2$, computed with respect to the best-fit point, will be therefore slightly different from our definition. This procedure, however, is commonly adopted to compute the expected sensitivity of an experiment that is still under development, so as to compare different setups on equal footing.

The variance is defined as:

$$\sigma_j^2 = N_j^0 + B_j^0 + [f_j N_j^0]^2 + [f_j B_j^0]^2, \tag{4.4}$$

where f_j is the uncorrelated bin-to-bin systematic error in the j -th bin: 2% for the golden channel and 10% for the silver channel, irrespectively of the energy bin, of the baseline and of the stored muon polarity. Notice that we can use the Gaussian expression for the χ^2 throughout our numerical simulation, with the possible exception of the silver channel data at the longest baseline, for which a Poissonian expression could be more appropriate due to the extremely low statistics (as it can be seen from table 1). However, as it will be shown in the following discussion on the results, the impact of the silver channel at that baseline is negligible.

In the numerical analysis of this section, the following parameters in common between three- and four-family models have been kept fixed to their central values:¹⁰ $\theta_{12} = 34^\circ$, $\theta_{23} = 45^\circ$; $\Delta m_{sol}^2 = 7.9 \times 10^{-5} \text{ eV}^2$, $\Delta m_{31}^2 = 2.4 \times 10^{-3} \text{ eV}^2$. The following two parameters specific to the four-family model have been also kept fixed: $\Delta m_{SBL}^2 = 1 \text{ eV}^2$ and $\delta_1 = 0$. Eventually, we have marginalized over $\theta_{24} \in [0, 12^\circ]$, $\theta_{34} \in [0, 35^\circ]$ and $\delta_2, \delta_3 \in [0, 360^\circ]$. Matter effects have been included considering a constant matter density $\rho = 3.4 \text{ g/cm}^3$ for the shortest baseline and $\rho = 4.3 \text{ g/cm}^3$ for the longest one, computed averaging over the density profile in the PREM [86] along the neutrino path. We have checked that marginalization over a 10% matter density uncertainty does not modify our results.

¹⁰We will not introduce any label to distinguish these parameters between three- and four-family models.

It is useful to show here the analytic expressions for the golden and silver channels oscillation probabilities in vacuum. For both channels it is mandatory to go beyond the $O(\epsilon^3)$ of the expansion in power of small parameters that was shown in eqs. (2.4), (2.8). At high orders in powers of ϵ , it is no longer possible to neglect terms proportional to the solar mass difference. In particular, for the short baseline $L = 3000$ km (the only case in which vacuum formulæ give some insight on the numerical results), the parameter $\Delta_{21}L$ ranges from $O(\epsilon^3)$ to $O(\epsilon^4)$, depending on the neutrino energy. We will thus show the oscillation probabilities $P_{e\mu}$ and $P_{e\tau}$ to order ϵ^8 in powers of $\sqrt{\theta_{13}}, \sqrt{\theta_{14}}, \sqrt{\theta_{24}}, \sqrt{\delta\theta_{23}}, \theta_{34}$ and $(\Delta_{21}L)^{1/4}$. For completeness, we have also computed the oscillation probability P_{es} and P_{ee} to the same order in ϵ (P_{es} can be found in the appendix), checking unitarity of the mixing matrix. Oscillation probabilities in matter at this order in ϵ are difficult to obtain and they will not be presented here.

The golden channel oscillation probability expanded to order ϵ^8 in vacuum is:

$$\begin{aligned}
P_{e\mu} = & 2\theta_{14}^2\theta_{24}^2 + 2\{\theta_{13}^2(1 + 2\delta\theta_{23} - \theta_{13}^2 - \theta_{14}^2 - \theta_{24}^2)\} \sin^2 \frac{\Delta_{31}L}{2} \\
& + 2\sqrt{2}\theta_{13}\theta_{14}\theta_{24}(1 + \delta\theta_{23}) \sin\left(\delta_2 - \delta_3 + \frac{\Delta_{31}L}{2}\right) \sin \frac{\Delta_{31}L}{2} \\
& + \sin 2\theta_{12}\theta_{13}(\Delta_{21}L) \cos\left(\delta_1 - \delta_2 + \delta_3 - \frac{\Delta_{31}L}{2}\right) \sin \frac{\Delta_{31}L}{2} \\
& + \frac{1}{\sqrt{2}} \sin 2\theta_{12}\theta_{14}\theta_{24}(\Delta_{21}L) \sin \delta_1 - s_{12}^2\theta_{13}^2(\Delta_{21}L) \sin \Delta_{31}L + \frac{1}{2} \sin^2 2\theta_{12}(\Delta_{21}L)^2,
\end{aligned} \tag{4.5}$$

whereas the silver channel oscillation probability at the same order is:

$$\begin{aligned}
P_{e\tau} = & 2\theta_{14}^2\theta_{34}^2 \\
& + 2\{\theta_{13}^2(1 - 2\delta\theta_{23} - \theta_{13}^2 - \theta_{14}^2 - \theta_{34}^2 + 2\delta\theta_{23}\theta_{34}^2) - \theta_{13}^2\theta_{24}\theta_{34} \cos \delta_3\} \sin^2 \frac{\Delta_{31}L}{2} \\
& - 2\sqrt{2}\theta_{13}\theta_{14}\theta_{24}\theta_{34}^2 \sin\left(\delta_2 - \delta_3 + \frac{\Delta_{31}L}{2}\right) \sin \frac{\Delta_{31}L}{2} \\
& + 2\sqrt{2}\theta_{13}\theta_{14}\theta_{34}\left(1 - \delta\theta_{23} - \frac{\theta_{34}^2}{2}\right) \sin\left(\delta_2 + \frac{\Delta_{31}L}{2}\right) \sin \frac{\Delta_{31}L}{2} \\
& - \sin 2\theta_{12}\theta_{13}(1 - \theta_{34}^2)(\Delta_{21}L) \cos\left(\delta_1 - \delta_2 + \delta_3 - \frac{\Delta_{31}L}{2}\right) \sin \frac{\Delta_{31}L}{2} \\
& - \frac{1}{\sqrt{2}} \sin 2\theta_{12}\theta_{14}\theta_{34}(\Delta_{21}L) \sin(\delta_1 + \delta_3) - s_{12}^2\theta_{13}^2(\Delta_{21}L) \sin \Delta_{31}L \\
& + \frac{1}{2} \sin^2 2\theta_{12}(\Delta_{21}L)^2.
\end{aligned} \tag{4.6}$$

Notice that the golden and silver channel expressions have leading terms proportional to θ_{13}^2 , i.e. they are $O(\epsilon^4)$ (as it was anticipated in section 2.4). This is the same order at which leading terms arise in the three-family model. We expect, thus, a similar sensitivity to θ_{13} in both three- and four-model analyses at the Neutrino Factory using these channels. On the other hand, we expect poor sensitivity to θ_{14} using these channels. First of all, dependence on θ_{14} in the golden and silver channel arise only at higher orders in ϵ (at $O(\epsilon^6)$ for the golden channel and at $O(\epsilon^5)$ for the silver channel, respectively). Secondly,

all the terms proportional to θ_{14} in the above probabilities appear in combination with either θ_{34} or θ_{24} , so when we evaluate the value of $\Delta\chi^2$ by marginalizing over θ_{34} and θ_{24} , both of which have tendency to be small because of the priors, these two probability can become almost independent of θ_{14} . For this reason, we expect poor sensitivity to θ_{14} using these channels. Nevertheless we discuss the sensitivities to both θ_{13} and θ_{14} because the sensitivity to θ_{13} can have nontrivial dependence on the true value of θ_{14} in the four neutrino case, as we will see below.

Eventually, the ν_e disappearance probability is:

$$\begin{aligned}
 P_{ee} = & 1 - 2\theta_{14}^2(1 - \theta_{14}^2) - 4\theta_{13}^2(1 - \theta_{13}^2 - 2\theta_{14}^2)\sin^2\frac{\Delta_{31}L}{2} \\
 & + 2s_{12}^2\theta_{13}^2(\Delta_{21}L)\sin\Delta_{31}L - \sin^2 2\theta_{12}(\Delta_{21}L)^2
 \end{aligned}
 \tag{4.7}$$

Notice that this channel has leading $O(\epsilon^4)$ dependence on both θ_{13} and θ_{14} . For this reason the most stringent bound on this angle has been obtained by reactor experiments, as we have shown in section 2.3. A detector with an extremely good electron identification efficiency is needed to perform this task, however, something beyond the reach of the MIND or MECC detectors. We are, thus, not considering this channel in the present paper. Figures 3 and 4 present the sensitivity to (3+1)-sterile neutrinos in the $(\theta_{13}^{(4fam)}, \theta_{14})$ -plane at 90% CL at the 50 GeV Neutrino Factory setup for several representative choices of δ_2 and δ_3 . In particular, δ_3 has been fixed to $\delta_3 = 0$ and 90° in figure 3 and figure 4, respectively. In both cases, the phase δ_2 (that reduces to the three-family CP-violating phase δ in the limit $\theta_{i4} \rightarrow 0$) has been fixed to $\delta_2 = 0, 90^\circ, 180^\circ$ and 270° . Results for the two baselines are shown both separately and summed: blue lines stand for the shortest baseline data; red lines stand for the longest baseline data; green lines stand for the sum of the two baselines. Solid lines stand for golden channel data, only, whereas dashed lines stand for the sum of golden and silver channels data. Eventually, the horizontal dashed grey line represents the present bound on θ_{14} that takes into account the four-family analysis of the atmospheric and reactor data.

First of all, notice that the golden and silver channel data show a very limited sensitivity to θ_{14} when marginalizing over θ_{24} and θ_{34} , as it was expected by inspection of the oscillation probabilities $P_{e\mu}$ and $P_{e\tau}$, eqs. (4.5), (4.6).

Secondly, when we focus on the golden channel results (solid lines), we notice a rather different behavior at the short and long baseline. At the short baseline, the sensitivity to $\theta_{13}^{(4fam)}$ is significantly phase-dependent: the maximal sensitivity to $\theta_{13}^{(4fam)}$ ranges from $\sin^2 2\theta_{13}^{(4fam)} = 1.5 \times 10^{-5}$ for $\delta_2 = \delta_3 = 0$ to 6×10^{-3} for $\delta_2 = \delta_3 = 90^\circ$, with a strong dependence on the θ_{14} value. This is a consequence of cancellations between the term proportional to $\theta_{13}(\Delta_{21}L)$ in the third line of eq. (4.5), that in three-family represents the interference between solar and atmospheric oscillations, and the term proportional to $\theta_{13}\theta_{14}\theta_{24}$ in the second line of the same equation.

The behavior is extremely different when we consider the golden channel at the long baseline. The location of the far detector corresponds to the three-family "magic baseline" [105], where the three-family dependence on the CP-violating phase δ vanishes. Notice that this happens as a consequence of the vanishing of the term in the third line of

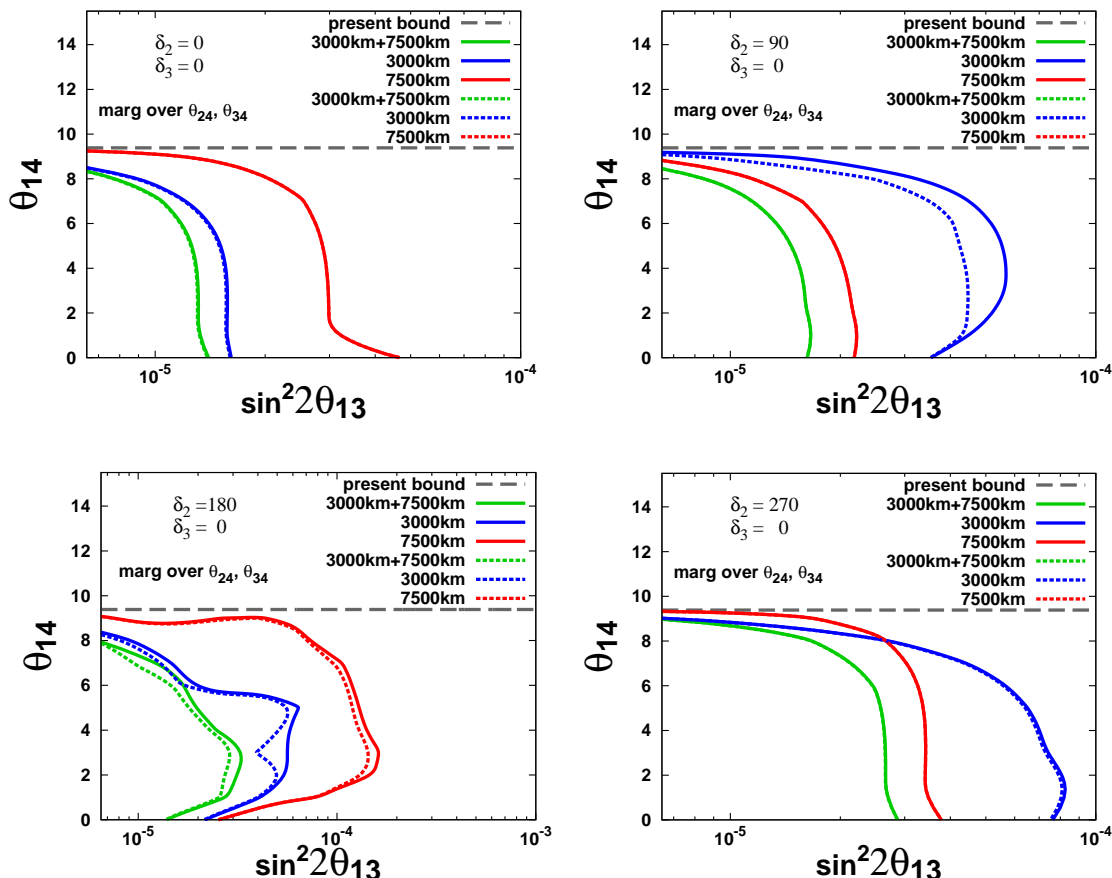


Figure 3. Sensitivity limit at 90% CL in the $(\sin^2 2\theta_{13}, \theta_{14})$ plane for $\delta_3 = 0$ and different values of δ_2 . The solid lines refer to the golden channel results, only. Dashed lines stand for the sum of golden and silver channel results. The colors are: blue for $L = 3000$ km; red for $L = 7500$ km; green for the combination of the two baselines; the horizontal dashed grey line represents the present bound on θ_{14} . The four panels represent our results for: $\delta_2 = 0$ (top left); $\delta_2 = 90^\circ$ (top right); $\delta_2 = 180^\circ$; (bottom left); $\delta_2 = 270^\circ$ (bottom right).

eq. (4.5) when computed in the Earth matter. This is, indeed, the only term through which a δ -dependence enters into the three-family golden channel oscillation probability. The four-family term in the third line of eq. (4.5), that reduces to the three-family one for vanishing θ_{i4} and δ_1, δ_3 , vanishes also. Therefore, no cancellations between different terms occur at this baseline and sensitivity to $\theta_{13}^{(4fam)}$ depends much less than for the short baseline on the values of δ_2, δ_3 and θ_{14} . This is precisely what we can see in all panels of figure 3 and 4.

A similar effect can be observed when we add the silver channel data to the golden channel ones at the short baseline. In this case, the term in the third line of eq. (4.5) cancels with the term in the fifth line of eq. (4.6) at the leading order, leaving an $O(\epsilon^8)$ term suppressed by $\theta_{13}\theta_{34}^2(\Delta_{21}L)$. Also in this case, we see indeed in all panels of both figures that a reduced dependence of the sensitivity to $\theta_{13}^{(4fam)}$ from δ_2, δ_3 and θ_{14} is achieved.

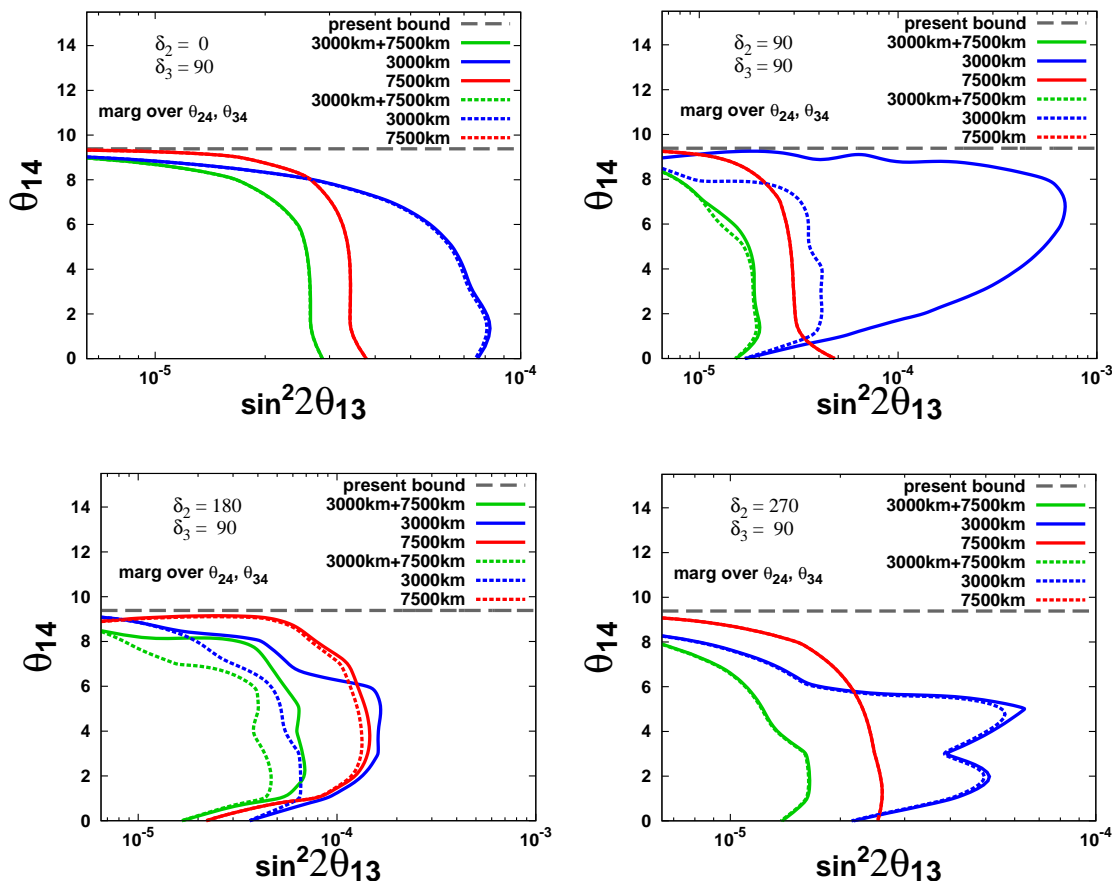


Figure 4. Sensitivity limit at 90% CL in the $(\sin^2 2\theta_{13}, \theta_{14})$ plane for $\delta_3 = 90^\circ$ and different values of δ_2 . The solid lines refer to the golden channel results, only. Dashed lines stand for the sum of golden and silver channel results. The colors are: blue for $L = 3000$ km; red for $L = 7500$ km; green for the combination of the two baselines; the horizontal dashed grey line represents the present bound on θ_{14} . The four panels represent our results for: $\delta_2 = 0$ (top left); $\delta_2 = 90^\circ$ (top right); $\delta_2 = 180^\circ$; (bottom left); $\delta_2 = 270^\circ$ (bottom right).

Particularly striking is the case of $\delta_2 = \delta_3 = 90^\circ$, figure 4 (top right), where we can see that the sensitivity to $\theta_{13}^{(4fam)}$ goes from $\sin^2 2\theta_{13}^{(4fam)} = 6 \times 10^{-3}$ for the golden channel alone to $\sin^2 2\theta_{13}^{(4fam)} = 3 \times 10^{-5}$ for the combination of golden and silver channels. On the other hand, the silver channel statistics at $L = 7500$ km from the source is extremely poor (see table 1). For this reason we have no impact whatsoever of this channel on the $\theta_{13}^{(4fam)}$ sensitivity at the long baseline.

The performance of the detectors located at the two baselines differ significantly depending on the specific choices of δ_2 and δ_3 . For most of the choices of (δ_2, δ_3) , the longest baseline outperforms the shortest one, with the only exceptions of $\delta_2 = 0, 180^\circ; \delta_3 = 0$ (figure 3, left panels) and $\delta_2 = 180^\circ; \delta_3 = 90^\circ$ (figure 4, bottom left panel).

The combination of the two channels and the two baselines at the 50 GeV Neutrino Factory has a rather good sensitivity to $\theta_{13}^{(4fam)}$: in the absence of a signal, we can exclude

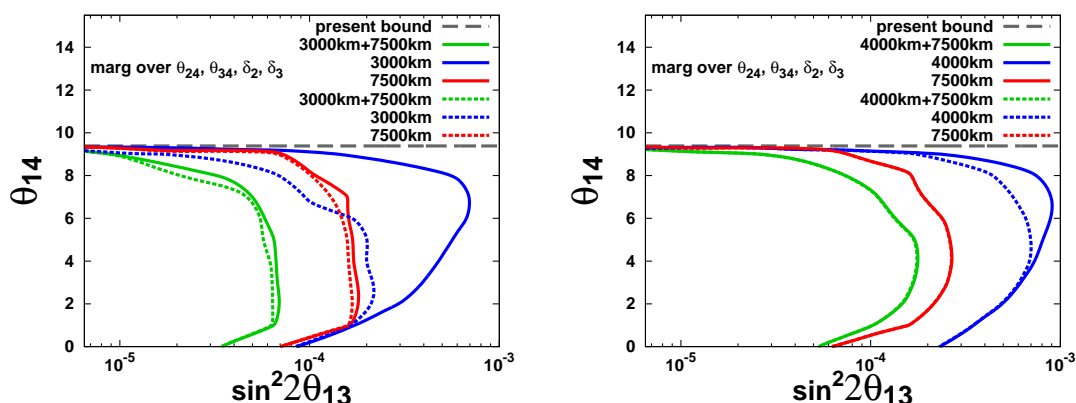


Figure 5. Sensitivity limit at 90% CL in the $(\sin^2 2\theta_{13}, \theta_{14})$ plane, marginalizing over $\theta_{24}, \theta_{34}, \delta_2$ and δ_3 . The solid lines refer to the golden channel results, only. Dashed lines stand for the sum of golden and silver channel results. The colors are: blue for the shortest baseline; red for longest baseline; green for the combination of the two baselines; the horizontal dashed grey line represents the present bound on θ_{14} . Left panel: 50 GeV Neutrino Factory; Right panel: 20 GeV Neutrino Factory.

values of $\theta_{13}^{(4fam)}$ larger than $\sin^2 2\theta_{13}^{(4fam)} \leq 4 \times 10^{-5}$ for any of the choices of (δ_2, δ_3) shown. The sensitivity to the active-sterile mixing angle θ_{14} , on the other hand, is $\theta_{14} \leq 9^\circ$ when marginalizing over θ_{24} and θ_{34} . We eventually compare the results obtained using the 50 GeV Neutrino Factory setup, figure 5 (left), with those that can be achieved using the 20 GeV Neutrino Factory ISS-inspired setup, figure 5 (right). As before, solid lines stand for golden channel data, only, whereas dashed lines stand for the combination of golden and silver channel data. Blue lines stand for the shortest baseline (3000 km or 4000 km); red lines for the longest baseline (7500 km in both setups); green lines for the combination of the two; eventually, the grey dashed line represents the present bound on θ_{14} . In addition to θ_{24} and θ_{34} , we have marginalized over the CP-violating phases δ_2 and δ_3 , with $\delta_2, \delta_3 \in [0, 360^\circ]$. The rest of the parameters have been kept fixed to the values given above.

First of all notice that for both setups the $\theta_{13}^{(4fam)}$ -sensitivity that can be reached using golden channel data, only, is much poorer at the short baseline than at the long baseline. We have found $\theta_{13}^{(4fam)} \leq 6 \times 10^{-4} (9 \times 10^{-4})$ for any value of θ_{14} at the short baseline for the 50 GeV (20 GeV) setup, to be compared with $\theta_{13}^{(4fam)} \leq 2 \times 10^{-4} (3 \times 10^{-4})$ at the long baseline for the 50 GeV (20 GeV) setup. The second relevant point is that the silver channel significantly improves the $\theta_{13}^{(4fam)}$ -sensitivity for the 50 GeV setup, but only marginally for the 20 GeV one. We can see that the $\theta_{13}^{(4fam)}$ -sensitivity at the short baseline using the combination of golden and silver channels becomes $\theta_{13}^{(4fam)} \leq 2 \times 10^{-4} (6 \times 10^{-4})$ for the 50 GeV (20 GeV) setup. When considering the long baseline we can see, however, that the impact of the silver channel becomes marginal (though it can still be observed for the 50 GeV setup).

The $\theta_{13}^{(4fam)}$ -sensitivity that can be reached using the combination of the two baselines is: $\theta_{13}^{(4fam)} \leq 6 \times 10^{-5} (1.5 \times 10^{-4})$ for any value of θ_{14} at the 50 GeV (20 GeV) setup. The

inclusion of the silver channel data does not modify significantly these results.

Our conclusion is that the higher energy setup has a much greater ultimate sensitivity to $\theta_{13}^{(4\text{fam})}$ than the ISS-inspired 20 GeV one. On the other hand, both setups are not able to improve the present bounds on θ_{14} when marginalizing over θ_{24}, θ_{34} (see, however, section 4.3). The silver channel can significantly improve the $\theta_{13}^{(4\text{fam})}$ -sensitivity when only one baseline is considered at the 50 GeV setup. However, it has a negligible impact when the combination of the golden channel data at the two baselines is considered.

Eventually, we have studied the impact of the correlated systematic errors α_s, β_s in eq. (4.1) on our results, For both the 50 GeV and 20 GeV setups, we have found that the results shown in figure 5 do not change for $\alpha_s = \beta_s = 0$. Golden and silver channels are indeed dominated by statistical errors.

4.1.2 Sensitivity to $U_{e4}U_{\mu4}$ and $U_{e4}U_{\tau4}$

Since sensitivity to θ_{14} at the Neutrino Factory is poor, it is worth investigating whether the Neutrino Factory has sensitivity to other combinations of the mixing matrix elements. From the form of the appearance oscillation probability

$$P(\nu_\alpha \rightarrow \nu_\beta) = 4\text{Re} [U_{\alpha3}U_{\beta3}^*(U_{\alpha3}^*U_{\beta3} + U_{\alpha4}^*U_{\beta4})] \sin^2 \left(\frac{\Delta m_{31}^2 L}{4E} \right) + \dots,$$

we can expect that the golden and silver channels have some sensitivity to $U_{e4}U_{\mu4}$ and $U_{e4}U_{\tau4}$. In the present parametrization (2.2) of the mixing matrix, we have $U_{e4}U_{\mu4} = s_{14}c_{14}s_{24} = s_{14}s_{24} + O(\epsilon^6)$ and $U_{e4}U_{\tau4} = s_{14}c_{14}c_{24}s_{34} = s_{14}s_{34} + O(\epsilon^5)$, where we have used the fact that $|\theta_{14}|$ and $|\theta_{24}|$ are small. In the analysis of sensitivity to $U_{e4}U_{\mu4}$ ($U_{e4}U_{\tau4}$), instead of using $|\theta_{14}|$ and $|\theta_{24}|$ ($|\theta_{14}|$ and $|\theta_{34}|$) as the independent variables, it is convenient to take $s_{14}s_{24}$ and s_{14}/s_{24} ($s_{14}s_{34}$ and s_{14}/s_{34}) as the independent ones, respectively. Taking this basis we have performed analysis on sensitivity to $U_{e4}U_{\mu4}$ and $U_{e4}U_{\tau4}$. The sensitivity is defined as in section 4.1.1 with straightforward replacements. The results are shown in figure 6 and they indicate that the combination of the golden and silver channels has good sensitivity to these variables. To see how much improvement we have, we take the square root of $U_{e4}U_{\mu4}$ or $U_{e4}U_{\tau4}$, so that these factors correspond roughly to sine of some angle. Then the upper bound for $\sqrt{U_{e4}U_{\mu4}}$ by the 50 GeV (20 GeV) Neutrino Factory is $\sqrt{5} \times 10^{-4}$ ($\sqrt{1} \times 10^{-3}$), which is about 15% (20%) of the current bound, $\sqrt{U_{e4}U_{\mu4}} \leq \sqrt{0.02}$. Similarly, the upper bound for $\sqrt{U_{e4}U_{\tau4}}$ by both 50 GeV and 20 GeV Neutrino Factory is $\sqrt{2} \times 10^{-3}$, which is about 20% of the current bound, $\sqrt{U_{e4}U_{\tau4}} \leq 0.06$.

For both $U_{e4}U_{\mu4}$ and $U_{e4}U_{\tau4}$ plots, we see that both the golden and silver channels play a role in giving the constraints. As it is expected from statistics, the result by the 50 GeV Neutrino Factory is better for $U_{e4}U_{\mu4}$, but the sensitivity to $U_{e4}U_{\tau4}$ is almost the same for the two setups (notice that the scale on the vertical axis for the left and right panels are different). For the 20 GeV case, the data at 7500 km perform very well and the combined data of 4000 km and 7500 km give a result almost comparable to that of 50 GeV.

It is interesting to note that the golden channel also plays a role in improving sensitivity to $U_{e4}U_{\tau4} \propto s_{34}$. We have obtained a lengthy analytic formula for the golden channel in matter with some approximation, i.e., to quartic order in ϵ while keeping all orders in θ_{34}

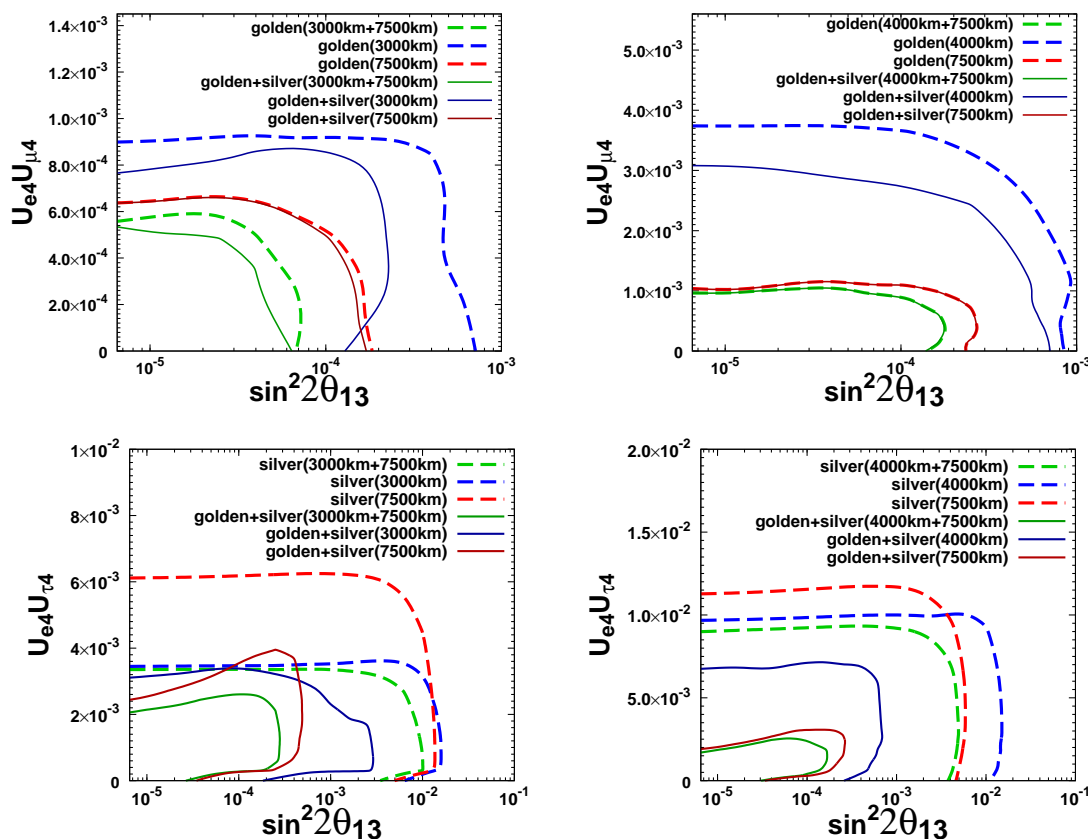


Figure 6. Sensitivity limit at 90% CL to $U_{e4}U_{\mu4}$ and $U_{e4}U_{\tau4}$. $\Delta\chi^2$ is evaluated for a fixed set of values of $(\sin^2 2\theta_{13}, U_{e4}U_{\mu4})$ (upper panels) or a fixed set of values of $(\sin^2 2\theta_{13}, U_{e4}U_{\tau4})$ (lower panels), marginalizing over $s_{14}/s_{24}, \theta_{34}, \delta_2$ and δ_3 (upper panels), or over $s_{14}/s_{34}, \theta_{24}, \delta_2$ and δ_3 (lower panels). Left panels: 50 GeV Neutrino Factory; Right panels: 20 GeV Neutrino Factory. The current bound on $U_{e4}U_{\mu4}$ ($U_{e4}U_{\tau4}$) is 0.02 (0.06).

and we have found that dependence on θ_{34} appears through the form of $O(\epsilon^4) \times s_{34}^2 A_e / \Delta E_{31}$. This explains why the golden channel has some sensitivity to $U_{e4}U_{\tau4}$ through the matter effect at the longer baseline, once we choose a suitable set of the independent parameters to vary.

4.2 Sensitivity to $(\theta_{24}, \theta_{34})$

The sensitivity is defined as in the previous section: we first compute the expected number of events for $\nu_\mu \rightarrow \nu_\mu$ and $\nu_\mu \rightarrow \nu_\tau$ oscillations for the input values $\theta_{13}^{(4\text{fam})} = 0$ and $\theta_{14} = \theta_{24} = \theta_{34} = 0, N^0$; we then compute the expected number of events in the $(\theta_{24}, \theta_{34})$ -plane for the same oscillation channels in the four-family model. The $\Delta\chi^2$, computed as in eq. (4.1) with respect to the "true" value N^0 , is eventually evaluated.

Contrary to the case of the golden and silver channels, however, the number of expected background events is much smaller than the signal for both the disappearance and discovery channels. The effect of α_b and β_b is, thus, negligible. Hence, we will not perform

minimization with respect to α_b and β_b for these channels and put these parameters to zero hereafter. As in the case of the golden and silver channels, the variance is defined by eq. (4.4), where N_j^0 in this case are the number of events of the disappearance or discovery channels, and the uncorrelated bin-to-bin systematic error f_j is 5% for the ν_μ disappearance channel and 10% for the discovery channel, irrespectively of the energy bin, of the baseline and of the stored muon polarity.

In the numerical analysis, the central values of the following parameters in common between three- and four-family models are: $\theta_{12} = 34^\circ$, $\theta_{13} = 5.7^\circ$, $\theta_{23} = 45^\circ$; $\Delta m_{\text{sol}}^2 = 7.9 \times 10^{-5} \text{ eV}^2$, $\Delta m_{31}^2 = 2.4 \times 10^{-3} \text{ eV}^2$; $\delta_2 = \delta = 0$ (where δ is the three-family CP-violating phase). The central values for the following three parameters specific to the four-family model are: $\Delta m_{\text{SBL}}^2 = 1 \text{ eV}^2$, $\theta_{14} = 0$ and $\delta_1 = 0$. Matter effects have been included considering a constant matter density $\rho = 3.4 \text{ g/cm}^3$ for the shortest baseline and $\rho = 4.3 \text{ g/cm}^3$ for the longest one, computed averaging over the density profile in the PREM [86] along the neutrino path. We have checked that marginalization over a 10% matter density uncertainty does not modify our results.

The sensitivity to (3+1)-sterile neutrinos at the 90% CL in the $(\theta_{24}, \theta_{34})$ -plane for the 50 GeV Neutrino Factory setup is shown in figures 7 and 8. In these figures, we have studied how the marginalization over θ_{23} , Δm_{31}^2 and δ_3 modify our results by varying them in the ranges $\theta_{23} \in [40^\circ, 50^\circ]$, $\Delta m_{31}^2 \in [2.0, 2.8] \times 10^{-3} \text{ eV}^2$ and $\delta_3 \in [0, 360^\circ]$. We have also checked the impact of the marginalization over all the other parameters (otherwise fixed to their central values, given above), by studying them one by one in combination with θ_{23} , Δm_{31}^2 and δ_3 . The considered marginalization ranges are: $\theta_{12} \in [30^\circ, 36^\circ]$; $\theta_{13} \in [0, 10^\circ]$; $\theta_{14} \in [0, 10^\circ]$; $\Delta m_{21}^2 \in [7.0, 8.3] \times 10^{-5} \text{ eV}^2$; $\delta_1 \in [0, 360^\circ]$ and $\delta_2 \in [0, 360^\circ]$. We have found that none of these parameters modify significantly our results, contrary to the case of θ_{23} , Δm_{31}^2 and δ_3 . Eventually, we have checked that changing the sign of Δm_{31}^2 does not modify our results, either.¹¹

First of all, in figure 7 we show the sensitivity limit at 90% CL to θ_{24} and θ_{34} , for fixed $\delta_3 = 0$, whilst marginalizing over θ_{23} in the range $\theta_{23} \in [40^\circ, 50^\circ]$ and Δm_{31}^2 in the range $\Delta m_{31}^2 \in [2.0, 2.8] \times 10^{-3} \text{ eV}^2$. Notice that the considered allowed range for θ_{23} is a bit smaller than its present allowed range from the three-family global analysis. The Neutrino Factory, however, has an enormous potential for improving the measurement of the three-family atmospheric parameters through the ν_μ disappearance channel as it was shown, for example, in ref. [109]. It is, therefore, absolutely reasonable to vary θ_{23} over a reduced range. In the two plots, red lines stand for the $\nu_\mu \rightarrow \nu_\mu$ disappearance channel data; blue lines stand for the $\nu_\mu \rightarrow \nu_\tau$ discovery channel data; green lines stand for the combination of both; the dashed grey line represents the present bound on θ_{24} and θ_{34} . We discuss first the left panel of figure 7, that refers to the results at the shortest baseline, $L = 3000 \text{ km}$. Notice that the disappearance channel has the strongest sensitivity to θ_{24} , that can be excluded above $\theta_{24} \sim 8^\circ$ for any value of θ_{34} . On the other hand, the $\nu_\mu \rightarrow \nu_\tau$ channel gives the ultimate sensitivity to θ_{34} for vanishing θ_{24} , $\theta_{34} \leq 15^\circ$. In both channels, we can see a strong correlation between θ_{24} and θ_{34} , with a bound

¹¹Notice that we are not sensitive to the sign of the largest mass difference, Δm_{41}^2 .

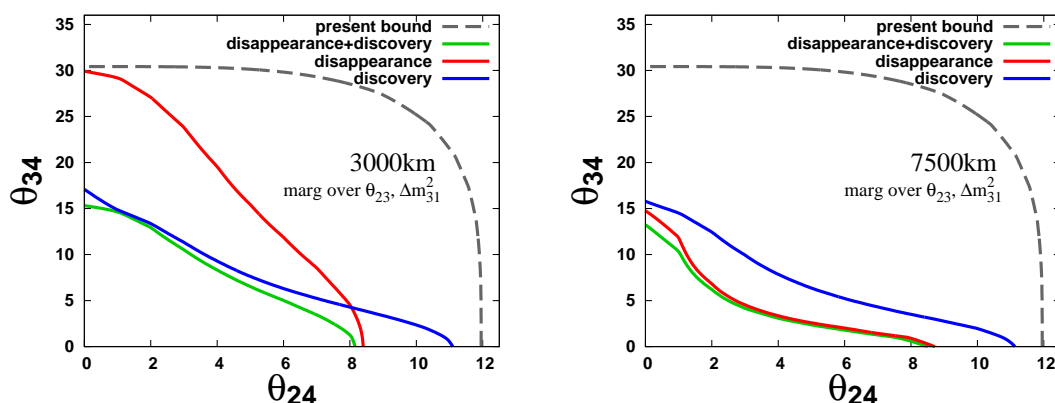


Figure 7. Sensitivity limit at 90% CL to θ_{24} and θ_{34} , for fixed $\delta_3 = 0$, whilst marginalizing over θ_{23} in the range $\theta_{23} \in [40^\circ, 50^\circ]$ and Δm_{31}^2 in the range $\Delta m_{31}^2 \in [2.0, 2.8] \times 10^{-3} \text{ eV}^2$. Red lines stand for the disappearance channel $\nu_\mu \rightarrow \nu_\mu$; blue lines stand for the discovery channel $\nu_\mu \rightarrow \nu_\tau$; green lines stand for the combination of both; the dashed grey line represents the present bound on θ_{24} and θ_{34} . Left: $L = 3000 \text{ km}$ baseline, Right: $L = 7500 \text{ km}$ baseline.

on θ_{34} that is strongly dependent on the specific value of θ_{24} considered. This behavior can be understood by looking at eqs. (2.6), (2.7) in section 2. The strong correlation between the two mixing angles is induced by the subleading $O(\epsilon^3)$ terms, proportional to $(A_n L) s_{24} s_{34} \cos \delta_3$ (since we are considering $\delta_3 = 0$ the term proportional to $\sin \delta_3$ in $P_{\mu\tau}$ vanishes). The $(\theta_{24}, \theta_{34})$ -correlation in the ν_μ disappearance channel is softer than in the $\nu_\mu \rightarrow \nu_\tau$ one: a consequence of the different statistical significance of this term in appearance and disappearance channels. Eventually, the combination of the two channels gives a very good sensitivity to both mixing angles.

A similar combined sensitivity is achieved at the longest baseline, $L = 7500 \text{ km}$, whose results are shown in the right panel of figure 7. We can see comparing the blue lines on both panels that the $\nu_\mu \rightarrow \nu_\tau$ channel sensitivity to $(\theta_{24}, \theta_{34})$ is substantially the same when changing baseline (the expected number of events for this channel at the two baselines is very similar, see table 1). On the other hand, the ν_μ disappearance channel data (the red line) has a much stronger sensitivity than at the short baseline: a consequence of the increased significance of the subleading term with respect to the dominant one in the disappearance channel due to larger matter effects at 7500 km.

The sensitivity of the disappearance channel to θ_{34} arises at a higher order in the expansion that we have presented in eqs. (2.6), (2.7). If we introduce terms to fourth order in ϵ (under the assumption $\theta_{13} = \theta_{14} = 0$, and taking into account the deviations from maximality of θ_{23}), we get:

$$\begin{aligned}
 P_{\mu\mu} = 1 - 2\theta_{24}^2 - \left[1 - 4(\delta\theta_{23})^2 - 2\theta_{24}^2 + \theta_{34}^2 \frac{A_n}{\Delta_{31}} \left(4\delta\theta_{23} - \theta_{34}^2 \frac{A_n}{\Delta_{31}} \right) \right] \sin^2 \frac{\Delta_{31}L}{2} \\
 - (A_n L) \left\{ 2\theta_{24} \theta_{34} \cos \delta_3 - \frac{\theta_{34}^2}{2} \left(4\delta\theta_{23} - \theta_{34}^2 \frac{A_n}{2\Delta_{31}} \right) \right\} \sin \Delta_{31}L + O(\epsilon^5), \quad (4.8)
 \end{aligned}$$

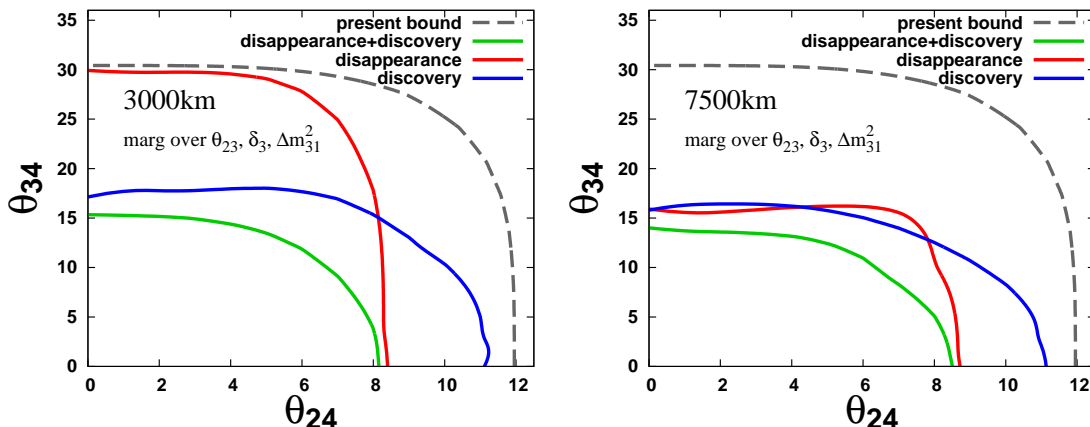


Figure 8. Sensitivity limit at 90% CL to θ_{24} and θ_{34} , marginalizing over $\theta_{23} \in [40^\circ, 50^\circ]$, the CP-violating phase $\delta_3 \in [0, 360^\circ]$ and $\Delta m_{31}^2 \in [2.0, 2.8] \times 10^{-3} \text{eV}^2$. Red lines stand for the disappearance channel $\nu_\mu \rightarrow \nu_\mu$; blue lines stand for the discovery channel $\nu_\mu \rightarrow \nu_\tau$; green lines stand for the combination of both; the grey dashed line represents the present bound on θ_{24} and θ_{34} . Left: $L = 3000 \text{ km}$ baseline, Right: $L = 7500 \text{ km}$ baseline.

$$\begin{aligned}
 P_{\mu\tau} = & \left\{ 1 - 4(\delta\theta_{23})^2 - \theta_{24}^2 - \theta_{34}^2 \left[1 - \frac{\theta_{34}^2}{3} - \frac{A_n}{\Delta_{31}} \left(4\delta\theta_{23} - \theta_{34}^2 \frac{A_n}{\Delta_{31}} \right) \right] \right\} \sin^2 \frac{\Delta_{31}L}{2} \\
 & + \left\{ \theta_{24} \theta_{34} \sin \delta_3 + (A_n L) \left[2\theta_{24} \theta_{34} \cos \delta_3 - \frac{\theta_{34}^2}{2} \left(4\delta\theta_{23} - \theta_{34}^2 \frac{A_n}{2\Delta_{31}} \right) \right] \right\} \sin \Delta_{31}L \\
 & + O(\epsilon^5), \tag{4.9}
 \end{aligned}$$

$$\begin{aligned}
 P_{\mu s} = & 2\theta_{24}^2 + \left[\theta_{34}^2 \left(1 - \frac{\theta_{34}^2}{3} \right) - \theta_{24}^2 \right] \sin^2 \frac{\Delta_{31}L}{2} - \theta_{24} \theta_{34} \sin \delta_3 \sin \Delta_{31}L \\
 & + O(\epsilon^5). \tag{4.10}
 \end{aligned}$$

Most of the θ_{34} -dependent terms in eq. (4.8) are proportional to the matter parameter $(A_n L)$. This means that the impact of these terms will be more important at the longest baseline, than at the shortest one (as we have seen in figure 7). On the other hand, the θ_{24} -sensitivity arises from the θ_{24}^2 term at $O(\epsilon^4)$ in eq. (4.8). These behaviors are strongly modified if we marginalize over the CP-violating phase δ_3 , as it can be seen in figure 8, where we present the sensitivity limit at 90% CL to θ_{24} and θ_{34} , whilst marginalizing over θ_{23} in the range $\theta_{23} \in [40^\circ, 50^\circ]$, over δ_3 in the range $\delta_3 \in [0, 360^\circ]$ and over Δm_{31}^2 in the range $\Delta m_{31}^2 \in [2.0, 2.8] \times 10^{-3} \text{eV}^2$. As before, red lines stand for the $\nu_\mu \rightarrow \nu_\mu$ disappearance channel data; blue lines stand for the $\nu_\mu \rightarrow \nu_\tau$ discovery channel data; green lines stand for the combination of both; the grey dashed line represents the present bound on θ_{24} and θ_{34} .

Notice that the correlation between θ_{24} and θ_{34} in the ν_μ disappearance data (red lines) has vanished. This is a straightforward consequence of the marginalization over δ_3 , that removes the term proportional to $(A_n L) s_{24} s_{34} \cos \delta_3$ in eq. (2.6), responsible for that correlation. We have found that the sensitivity on the two active-sterile mixing angles θ_{24} and θ_{34} is now represented by vertical and horizontal lines (similar to the results in figure 5). A similar effect is found for the $\nu_\mu \rightarrow \nu_\tau$ appearance channel data (blue lines),

though softer. We can see that, at both baselines (but more significantly at the longest one) some remnants of the $(\theta_{24}, \theta_{34})$ -correlation can still be observed for this channel. Comparing the results of the two channels, we have found again that at the short baseline the $\nu_\mu \rightarrow \nu_\mu$ data give the best sensitivity to θ_{24} , whereas the $\nu_\mu \rightarrow \nu_\tau$ data give the best sensitivity to θ_{34} . At the long baseline, $\nu_\mu \rightarrow \nu_\mu$ is as good as $\nu_\mu \rightarrow \nu_\tau$ in the θ_{34} -sensitivity.

We, eventually, compare the 90% CL $(\theta_{24}, \theta_{34})$ -sensitivity that can be obtained using the combination of the two channels and of the two baselines at the 50 GeV Neutrino Factory setup, figure 9 (left), with the one that can be achieved using the 20 GeV Neutrino Factory ISS-inspired setup, figure 9 (right). As before, red lines stand for ν_μ disappearance channel data; blue lines for the $\nu_\mu \rightarrow \nu_\tau$ discovery channel data; green lines for the combination of both channels; the grey dashed line represents the present bound on θ_{24} and θ_{34} . Data for the two baselines are always summed. In these plots, we have marginalized over $\theta_{23} \in [40^\circ, 50^\circ]$, $\delta_3 \in [0, 360^\circ]$ and $\Delta m_{31}^2 \in [2.0, 2.8] \times 10^{-3} \text{eV}^2$. The rest of the parameters have been kept fixed to the values given previously.¹²

First of all, we can see by comparing red lines (the disappearance channel data) between figure 9 (left) and figure 9 (right) that the ultimate sensitivities to θ_{24} and θ_{34} at the two setups are very similar: the upper bounds $\theta_{24} \leq 7.5^\circ (8^\circ)$ and $\theta_{34} \leq 15^\circ$ can be inferred from the data for the 50 GeV (20 GeV) setup. When we eventually combine the results for the disappearance and the discovery channels, however, we find that the 50 GeV Neutrino Factory outperforms the 20 GeV ISS-inspired one, as it can be seen comparing the green lines in figure 9. This can be easily explained pointing out that the discovery channel data (blue lines) are able to exclude a significantly larger region of the parameter space when going to higher energy, a straightforward consequence of the higher statistics due to the higher $\nu_\tau N$ cross-section. In figure 9 we have also studied the impact of the correlated systematic errors α_s, β_s in eq. (4.1) on our results. Dashed blue, red and green lines represent the 90% CL sensitivities to $(\theta_{24}, \theta_{34})$ when the correlated systematic errors α_s, β_s are not included and only the uncorrelated bin-to-bin systematic errors ($f_j = 5\%$ for the ν_μ disappearance channel and $f_j = 10\%$ for the discovery channel, irrespectively of the energy bin, of the baseline and of the stored muon polarity) are taken into account.

Comparing dashed and solid lines at the 20 GeV Neutrino Factory (right panel), we can see that the inclusion of the correlated systematic errors has a negligible impact when analyzing the data at this setup. On the other hand, when studying the data for both channels at the 50 GeV setup, we can see that the inclusion of these errors modify our results. In particular, the sensitivity to θ_{24} through the ν_μ disappearance channel goes from $\theta_{24} \leq 6^\circ$ when only f_j is considered to $\theta_{24} \leq 7.5^\circ$ when α_s, β_s are also taken into account.

Our final conclusion is the following: using the 20 GeV ISS-inspired Neutrino Factory, we get two roughly independent limits on the two angles θ_{24} and θ_{34} : $\theta_{24} \leq 8^\circ$ for any value of θ_{34} and $\theta_{34} \leq 14^\circ$ for any value of θ_{24} at the 90 % CL. Slightly stronger ultimate limits are obtained at the 50 GeV Neutrino Factory: $\theta_{24} \leq 7.5^\circ$ for vanishing θ_{34} and $\theta_{34} \leq 12^\circ$ for vanishing θ_{24} . The significantly large discovery channel statistics at the 50 GeV Neutrino Factory with respect to the 20 GeV one, however, strongly increase the sensitivity of this

¹² We have checked that the effect of the marginalization on the rest of the parameters do not affect the results.

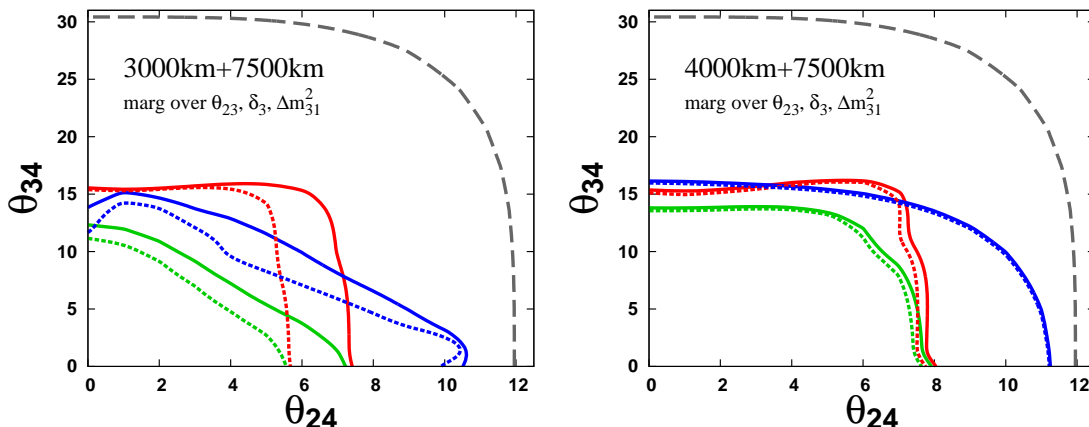


Figure 9. Sensitivity limit at 90% CL to θ_{24} and θ_{34} , marginalizing over $\theta_{23} \in [40^\circ, 50^\circ]$, the CP-violating phase $\delta_3 \in [0, 360^\circ]$ and $\Delta m_{31}^2 \in [2.0, 2.8] \times 10^{-3} \text{eV}^2$, for the combination of the two baselines. Dashed lines stand for the results without the correlated systematic errors. Red lines stand for the disappearance channel $\nu_\mu \rightarrow \nu_\mu$; blue lines stand for the discovery channel $\nu_\mu \rightarrow \nu_\tau$; green lines stand for the combination of both. Left panel: 50 GeV Neutrino Factory; Right panel: 20 GeV Neutrino Factory.

setup to the combination of θ_{24} and θ_{34} , such that a roughly diagonal line in the $(\theta_{24}, \theta_{34})$ plane connecting $(\theta_{24}, 0)$ and $(0, \theta_{34})$ can be drawn.

4.3 Discrimination of the four neutrino schemes

In the subsections 4.1 and 4.2 we have discussed the sensitivity to θ_{13} , θ_{14} , θ_{24} , θ_{34} by looking at statistical significance of deviation of a four-flavor scheme from that with a certain set of reference values of the oscillation parameters. Here we will discuss whether the Neutrino Factory setup can distinguish our four-neutrino scheme from the three-flavor scenario.

We introduce the "sterile neutrino discovery potential", defined as follows:

$$\Delta\chi^2(4\text{fam}) = \min_{\text{marg par}} \left[\sum_{\text{pol.}, (\text{chan.}), (L)} \min_{\alpha'_s, \beta'_s} \left\{ \sum_j \frac{1}{\sigma_j^2} \left((1 + \alpha_s + x_j \beta_s) N_j(3\text{fam}) + (1 + \alpha_b + x_j \beta_b) B_j(3\text{fam}) - N_j(4\text{fam}) - B_j(4\text{fam}) \right)^2 + \left(\frac{\alpha_s}{\sigma_{\alpha_s}} \right)^2 + \left(\frac{\alpha_b}{\sigma_{\alpha_b}} \right)^2 + \left(\frac{\beta_s}{\sigma_{\beta_s}} \right)^2 + \left(\frac{\beta_b}{\sigma_{\beta_b}} \right)^2 \right\} + \Delta\chi_{\text{atm+re}}^2(4\text{fam}) \right], \quad (4.11)$$

where $\Delta\chi_{\text{atm+re}}^2(4\text{fam})$, defined in eq. (4.2), is the prior from the four-flavor oscillation analysis of the atmospheric and reactor data, and the errors of the oscillation parameters in the prior $\Delta\chi_{\text{atm+re}}^2(4\text{fam})$ are given by eq. (4.3).

A remark is in order. The definition of the $\Delta\chi^2$ in the present case, although looking similar, is slightly different from that used in the previous sections. In sections 4.1 and 4.2 we assumed that the minimum of the χ^2 corresponds to the "true" values of the four-family model, and therefore $\chi_{\text{min}, 4\text{fam}}^2 = 0$. The $\Delta\chi^2$ is then computed in the same model in which

data are generated, and CL contours define the region of parameter space compatible at a given CL with the "true" values. In this section we also assume that data are generated in the four-family model, but we try to fit them in the three-family model. The minimum of the χ^2 in the four-family model is located at the "true" values of the parameters and $\chi_{\min,4fam}^2 = 0$. On the other hand, when we try to fit the four-family-generated data in the three-family model we will in general find $\chi_{\min,3fam}^2 \neq 0$, since a "wrong" model is used to fit the data, except for the special case defined by $\theta_{j4} = 0$ ($j = 1, 2, 3$), $\theta_{ij}^{(4fam)} = \theta_{ij}|_{\text{bestfit}}$ ($(i, j) = (1, 2), (1, 3), (2, 3)$), $\Delta m_{j1}^{2(4fam)} = \Delta m_{j1}^2|_{\text{bestfit}}$ ($j = 2, 3$), where the two models coincide and $\Delta\chi^2 = 0$. In the rest of the four-flavor parameter space, the $\Delta\chi^2$ defined in eq. (4.12) corresponds to $\chi_{\min,3fam}^2 - \chi_{\min,4fam}^2$. CL contours define, then, regions in the four-family parameter space for which a three-family fit to the data is worse than a four-family fit to the data of a quantity $\Delta\chi^2$. For example, a point with $\Delta\chi^2 = 4.61$ is a point that is fitted by the four-family model much better than by the three-family model. We will define points outside this contour as points for which the hypothesis that data can be fitted in the three-family model is "excluded at 90% CL". Under these premises, we can use eq. (4.12) to determine regions in which we are able to distinguish four- from three-family models in the four-flavor parameter space in the same manner as in the previous subsections.

Since the excluded region is expected to depend little on the solar neutrino oscillation parameters in the three-flavor scheme, we will not marginalize $\Delta\chi^2$ with respect to $\theta_{12}^{(3fam)}$ and $\Delta m_{21}^{2(3fam)}$ in eq. (4.12). Moreover, while $\Delta\chi^2$ is naively expected to depend on all of the parameters $\theta_{13}^{(3fam)}$, $\theta_{23}^{(3fam)}$, $|\Delta m_{31}^{2(3fam)}|$, $\delta^{(3fam)}$, we have found numerically that it suffices to vary some of the parameters and put other parameters to the best-fit values in most analyses. Namely, in the case of the golden and silver (disappearance and discovery) channels, a dominant role is played by $\theta_{13}^{(3fam)}$ and $\delta^{(3fam)}$ ($\theta_{23}^{(3fam)}$ and $|\Delta m_{31}^{2(3fam)}|$) which are the only three-family parameters that we vary, and the other three-family ones are fixed in the analysis. To compare the results with those in the subsections 4.1 and 4.2, we project the excluded region either in the $(\theta_{13}^{(4fam)}, \theta_{14})$ plane, or in the $(\theta_{24}, \theta_{34})$ plane. In these projections, we would like to obtain the most conservative excluded region, i.e., the common excluded region in the $(\theta_{24}, \theta_{34})$ plane irrespective of the values of $\theta_{13}^{(4fam)}$ and θ_{14} , or the common excluded region in the $(\theta_{13}^{(4fam)}, \theta_{14})$ plane irrespective of the values of θ_{24} and θ_{34} . Notice that the four angles can in principle be measured simultaneously if we use informations from the four channels at the same time. To obtain them, in principle we have to marginalize $\Delta\chi^2$ not only with respect to the three-family parameters described above but also with respect to the four-family ones, such as $\theta_{12}^{(4fam)}$, $\theta_{23}^{(4fam)}$, $\Delta m_{21}^{2(4fam)}$, $|\Delta m_{32}^{2(4fam)}|$, $\delta_1, \delta_2, \delta_3$, as well as $(\theta_{24}, \theta_{34})$ in the former case and $(\theta_{13}^{(4fam)}, \theta_{14})$ in the latter. In marginalizing over the four-family parameters, however, we do not have to vary all the parameters for a couple of reasons. First of all, since the excluded region is expected to depend little on the solar neutrino oscillation parameters in the four-flavor scheme, we can fix the solar parameters $\theta_{12}^{(4fam)}$, $\Delta m_{21}^{2(4fam)}$, δ_1 . Secondly, because of the prior $\Delta\chi_{\text{atm+re}}^2(4fam)$, in practice we can fix the following parameters to the best fit values: $s_{13}^{2(4fam)} \simeq 0.01$, $s_{23}^{2(4fam)} \simeq 0.5$, $|\Delta m_{31}^{2(4fam)}| \simeq 2.4 \times 10^{-3} \text{eV}^2$, $(\theta_{24}, \theta_{34}) \simeq (0, 0)$ in the case

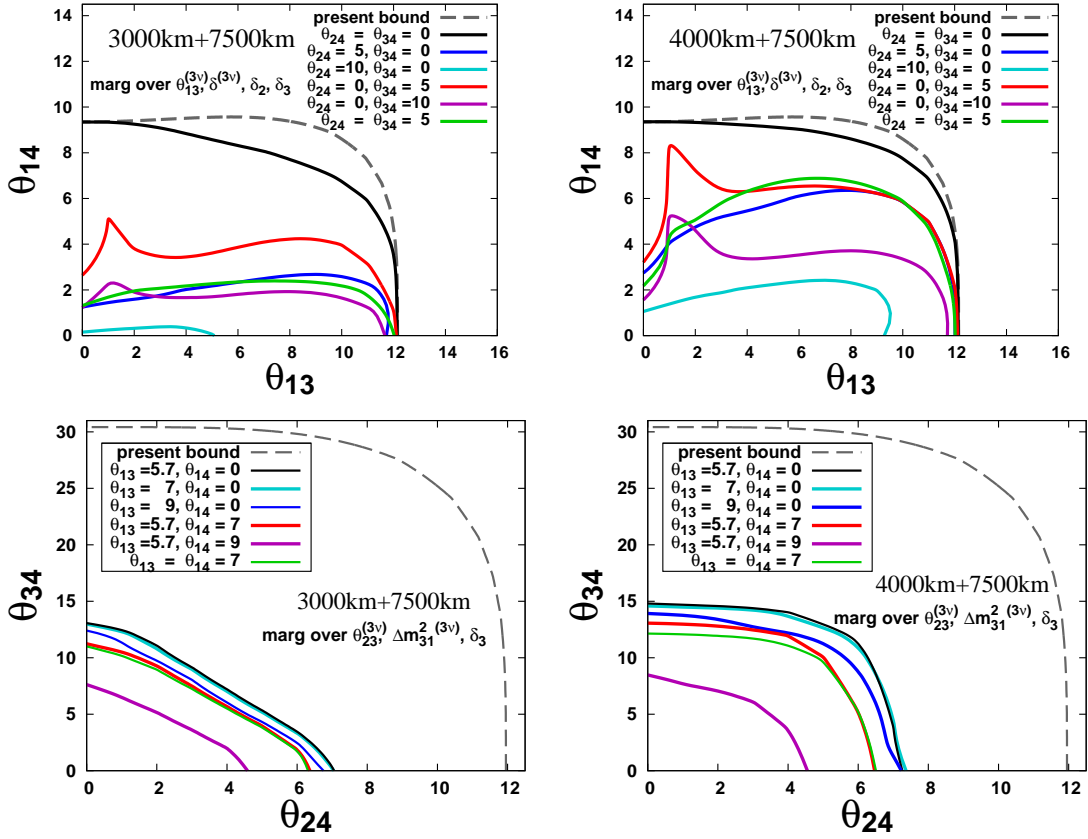


Figure 10. Left-upper panel: The right upper part of each line is the region projected onto the $(\theta_{13}, \theta_{14})$ plane, in which the hypothesis of the three flavor scheme is excluded at 90% CL at the 50 GeV Neutrino Factory. It is obtained by marginalizing over $\theta_{13}^{(3\text{fam})}$ and $\delta^{(3\text{fam})}$ as well as δ_2 and δ_3 . The grey dashed lines stand for the excluded region obtained only from the prior $\Delta\chi_{\text{atm+re}}^2(4\text{fam})$ where terms other than $(s_{13}^{2(4\text{fam})} - 0.01)^2/\sigma^2(s_{13}^2) + (s_{14}^2)^2/\sigma^2(s_{14}^2)$ are assumed to be zero in eq. (4.2). The excluded regions for nonvanishing θ_{24} or θ_{34} , which are always larger than the case for $\theta_{24} = \theta_{34} = 0$, are also depicted for information. Left-lower panel: Excluded region at 90% CL projected onto the $(\theta_{24}, \theta_{34})$ plane. It is obtained by marginalizing over $\theta_{23}^{(3\text{fam})}$, $|\Delta m_{31}^{2(3\text{fam})}|$ as well as δ_3 . The grey dashed lines stand for the excluded region obtained only from the prior $\Delta\chi_{\text{atm+re}}^2(4\text{fam})$ where terms other than $(s_{24}^2)^2/\sigma^2(s_{24}^2) + (s_{34}^2)^2/\sigma^2(s_{34}^2)$ are assumed to be zero in eq. (4.2). Right-upper(lower) panel: The same figure as the left-upper(lower) panel for the 20 GeV ISS-inspired setup.

of the $(\theta_{13}^{(4\text{fam})}, \theta_{14})$ plane, and $(\theta_{13}^{(4\text{fam})}, \theta_{14}) \simeq (5.7^\circ, 0)$ in the case of the $(\theta_{24}, \theta_{34})$ plane. Thus, the only non-trivial four-family parameters to be marginalized over are δ_2 and δ_3 in the case of the $(\theta_{13}^{(4\text{fam})}, \theta_{14})$ plane, and δ_3 in the case of the $(\theta_{24}, \theta_{34})$ plane.

The results obtained are presented in figure 10, where the dashed black line stands for the region which is excluded by the prior, i.e., by the present data of the atmospheric and reactor experiments. Upper panels show the "sterile neutrinos discovery potential" of golden and silver channels; lower panels the "discovery potential" of ν_μ disappearance and $\nu_\mu \rightarrow \nu_\tau$ appearance channel. On the left, we show results obtained for the 50 GeV Neutrino

Factory; on the right, using the 20 GeV ISS-inspired setup. We can see in figure 10 (upper panels) that at both setups, if we have no information on θ_{24} and θ_{34} , then the golden and silver channels cannot discriminate between the three- and four-family models for both setups within the presently allowed region. If we can previously measure θ_{24} and θ_{34} using the $\nu_\mu \rightarrow \nu_\mu$ and $\nu_\mu \rightarrow \nu_\tau$ channels, finding that one or both angles are non-vanishing, then we can see in both upper panels of figure 10 that the "sterile neutrino discovery potential" of the combination of golden and silver channels is significantly improved. For example, for $\theta_{34} \sim 10^\circ$, the 50 GeV (20 GeV) setup can distinguish the (3+1)-neutrino model from standard three-family oscillations for θ_{14} as small as $\theta_{14} \sim 2^\circ(4^\circ)$. This is because of the same reason that the Neutrino Factory has good sensitivity to $U_{e4}U_{\mu 4}$ and $U_{e4}U_{\tau 4}$, as was discussed in section 4.1.2. We point out that the silver channel gives a non-trivial contribution to the "discovery potential" $\Delta\chi^2$ in some regions of the parameter space, although the contributions of the golden and silver channels are not shown separately.

In figure 10(lower panels) we can see that, irrespectively of prior knowledge of $\theta_{13}^{(4\text{fam})}$ and θ_{14} , the combination of the ν_μ disappearance and the $\nu_\mu \rightarrow \nu_\tau$ discovery channels permits discrimination between the four- and three-neutrino oscillation models in a significant region of the presently allowed parameter space. The additional information from golden and silver channels increases the region in which discrimination is possible.

We conclude that combination of the four channels is extremely effective to tell the difference between the four- and three-flavor schemes in a significant region of the presently allowed parameter space. Notice that the synergy between the four channels is not symmetric: whereas a previous knowledge of $(\theta_{24}, \theta_{34})$ strongly increase the "discovery potential" in the $(\theta_{13}^{(4\text{fam})}, \theta_{14})$ -plane, the measurement of $(\theta_{13}^{(4\text{fam})}, \theta_{14})$ has a much smaller impact in the "discovery potential" in the $(\theta_{24}, \theta_{34})$ -plane. Eventually, the 50 GeV setup has a greater "sterile neutrino discovery potential" than the 20 GeV one.

4.4 Dependence of sensitivity on the systematic errors

We have also investigated the dependence of the performance of the four channels on the systematic errors.

As for the golden and silver channels, for which statistical errors are dominant, we have found from numerical calculations that the sensitivities of these two channels to $\theta_{13}^{(4\text{fam})}$ and θ_{14} depend only to some extent on σ_α (the correlated systematic error on the overall normalization), and they depend very little on f_j (the bin-to-bin uncorrelated error) and σ_β (the correlated systematic error in the linear distortion of the spectral shape).

The dependence of the discovery and disappearance channels on f_j , σ_α and σ_β (and on the MECC volume, in the case of the former) is shown in figure 11. The upper panels present the discovery channel $(\theta_{24}, \theta_{34})$ -sensitivity, where we consider $f_j \equiv f_{\mu\tau} = 0.10, 0.03$, $\sigma_\alpha = 0.100, 0.050, 0.025, 0.010$, and the MECC mass either 4 or 8 kton. The lower panels present the disappearance channel $(\theta_{24}, \theta_{34})$ -sensitivity, assuming $f_j \equiv f_{\mu\mu} = 0.05, 0.02$ and $\sigma_\alpha = 0.100, 0.050, 0.025, 0.010$. We have checked numerically that the impact of the systematic error σ_β in the linear distortion of the spectral shape is small and it will not be discussed here. For both channels we have considered the 50 GeV setup performance (left panels) and the 20 GeV setup one (right panels). From figure 11 (upper panels), we see

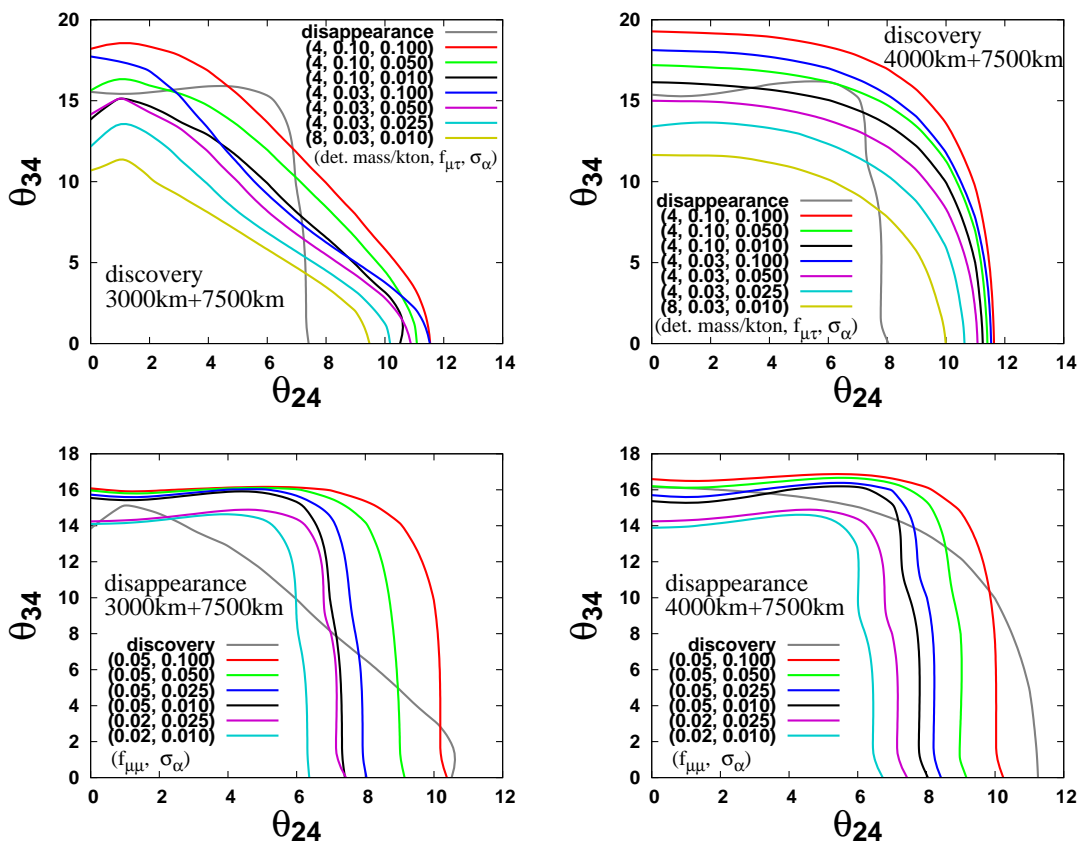


Figure 11. The 90%CL sensitivity to $(\theta_{24}, \theta_{34})$ using the $\nu_\mu \rightarrow \nu_\tau$ (the upper panels) and $\nu_\mu \rightarrow \nu_\mu$ (the lower panels) channels for different values of the uncorrelated bin-to-bin systematic error $f_j \equiv f_{\mu\tau} = 0.1, 0.03$ and $f_j \equiv f_{\mu\mu} = 0.05, 0.02$, of the correlated systematic error on the overall normalization $\sigma_{\alpha_s} = 0.1, 0.05, 0.025, 0.01$ and of the MECC mass ($= 4, 8$ kton in the case of $\nu_\mu \rightarrow \nu_\tau$). Left panels: at the 50 GeV setup; Right panels: at the 20 GeV ISS-inspired setup. In all the figures black lines stand for the excluded region for the reference values used in the calculations in other sections. The grey lines stand for the excluded region using the disappearance (discovery) channel with $f_{\mu\mu} = 0.05$, $\sigma_{\alpha_s} = 0.01$ (with 4 kton, $f_{\mu\tau} = 0.1$, $\sigma_{\alpha_s} = 0.01$).

that $f_{\mu\tau}$ is the most important factor to improve the performance of the discovery channel for both the 50 GeV and 20 GeV neutrino factories. On the other hand, an increase of the MECC mass from 4 to 8 kton improves only marginally the discovery channel sensitivity. In figure 11 (lower panels), we see that a reduction of both $f_{\mu\mu}$ and σ_α should be pursued to increase the disappearance channel sensitivity. One important conclusion from figure 11 is that an improvement of $f_{\mu\tau}$ below 10% is mandatory in order to take full advantage of the discovery channel at the Neutrino Factory, particularly for the 20 GeV setup. This error represents indeed our incomplete knowledge of the MECC detector. To improve our analysis on the discovery channel in the future, we need detailed information on the correlated and uncorrelated systematic errors, such as the uncertainties of the detection efficiency which depend only on the nature of MECC or depend on the characteristics of

the individual detectors located at each of the two baselines. Although there has been no study on these systematic errors so far, they are expected to be better understood after the first years of data taking of the OPERA experiment (that started operation in 2008).

4.5 A CP-violating sterile neutrino signal

In sections 4.1 and 4.2 we have considered the case of a null result for sterile neutrino searches at the Neutrino Factory after 4 years running for both muon polarities, showing exclusion plots both in the $(\theta_{13}^{(4fam)}, \theta_{14})$ - and in the $(\theta_{24}, \theta_{34})$ -planes. However, due to the impressive statistics achievable at the Neutrino Factory, it could well be possible that a positive signal is found (if sterile neutrinos with $O(1eV^2)$ mass difference with respect to active ones do exist). For this reason, in section 4.3 we have shown the region of the parameter space for which it is possible to distinguish the (3+1)-model from three-family oscillations.

Eventually, we will present in this section a first analysis of the precision achievable in our setup in the simultaneous measurement of mixing angles and CP-violating phases. We first focus on θ_{24}, θ_{34} and on the CP-violating phase δ_3 . Notice that each of the three possible CP-violating signals in a four-family model is related to a different Jarlskog invariant, proportional to a different combination of the mixing angles. The Jarlskog invariant that depends on $\sin \delta_3$ is, in our parametrization, proportional to the combination $\sin 2\theta_{23}s_{24}s_{34} \sin \delta_3$, as it can be seen in eqs. (4.8), (4.9). A measurement of δ_3 is thus possible only if both θ_{24} and θ_{34} are simultaneously non-vanishing. We will thus show 99% CL contours in the (θ_{34}, δ_3) -plane for particular input pairs $(\bar{\theta}_{34}, \bar{\delta}_3)$ for fixed non-vanishing values of θ_{24} .

The measurement of (θ_{34}, δ_3) is achieved combining data from the ν_μ disappearance channel and the $\nu_\mu \rightarrow \nu_\tau$ discovery channel. This analysis, of course, does not pretend to be as exhaustive as those that have been presented in the framework of the three-family model. In particular, we will not address within a comprehensive approach the problem of degeneracies in four-family models. Notice that this problem, extremely severe in the three-family oscillation studies at the Neutrino Factory (see, for example, refs. [69, 108] and [122]), is expected to be even more complicated in a four-neutrino model. In the particular case of the δ_3 -dependent CP-violating signal, that can be extracted using the $\nu_\mu \rightarrow \nu_\mu$ and $\nu_\mu \rightarrow \nu_\tau$ channels, we do expect to observe at least degeneracies due to the (θ_{34}, δ_3) -correlation (the so-called "intrinsic degeneracies", [69]); those dependent on the wrong reconstruction of the sign of the atmospheric mass difference¹³ Δm_{31}^2 (known as "sign degeneracies", [70]); and, eventually, those dependent on a wrong reconstruction of the "atmospheric" mixing angle θ_{23} octant (known as "octant degeneracies", [107]).

The contours in the (θ_{34}, δ_3) -plane have been obtained as follows: we have first computed the expected number of events for $\nu_\mu \rightarrow \nu_\mu$ and $\nu_\mu \rightarrow \nu_\tau$ oscillations in the four-family model for particular choices of the relevant parameters, $\theta_{24} = \bar{\theta}_{24}, \theta_{34} = \bar{\theta}_{34}$ and $\delta_3 = \bar{\delta}_3$. We have then computed the expected number of events in the (θ_{34}, δ_3) -plane for the same oscillation channels in the four-family model, varying $\theta_{34} \in [0, 35^\circ]$ and $\delta_3 \in [0, 360^\circ]$. The

¹³ At long baselines we are not sensitive to the sign of the SBL mass difference Δm_{41}^2 .

$\Delta\chi^2$ is then computed as follows:

$$\Delta\chi^2 = \left(\sum_j [N_j(\bar{\theta}_{24}, \theta_{34}, \delta_3) - N_j(\bar{\theta}_{24}, \bar{\theta}_{34}, \bar{\delta}_3)]^2 / \sigma_j^2 \right) \quad (4.12)$$

where the minimum of the χ^2 is, trivially, obtained for $\theta_{34} = \bar{\theta}_{34}$; $\delta_3 = \bar{\delta}_3$. As before, j runs over the different signals: the ν_μ disappearance and the $\nu_\mu \rightarrow \nu_\tau$ discovery channels data, divided into 10 energy bins, for the two baselines and the two possible stored muons polarities. The variance σ_j is defined by eq. (4.4), with $f_j = 5\%$ for the ν_μ disappearance channel and 10% for the $\nu_\mu \rightarrow \nu_\tau$ discovery channel. No correlated systematic errors have been considered in the plots of this section. The region in the (θ_{34}, δ_3) -plane compatible with the input values $(\bar{\theta}_{34}, \bar{\delta}_3)$ at the 2 d.o.f.'s 99% CL is eventually defined by drawing the contour line corresponding to $\Delta\chi^2 = 9.21$. Notice that we have also studied the simultaneous measurement of θ_{24}, θ_{34} and δ_3 using the combination of the $\nu_\mu \rightarrow \nu_\mu$ and $\nu_\mu \rightarrow \nu_\tau$ channels, finding that sensitivity to δ_3 is lost for values of the product $s_{24}s_{34}$ smaller than $(s_{24}s_{34})_{\min} \sim 0.01$. The results that we show have been obtained for choices of the input parameters $(\bar{\theta}_{24}, \bar{\theta}_{34})$ such that $s_{24}s_{34} \geq (s_{24}s_{34})_{\min}$. We show in figure 12 the 2 d.o.f.'s 99 %CL contours for the simultaneous measurement of θ_{34} and δ_3 using the combined data from the disappearance and the discovery channels for two representative values of θ_{24} : $\bar{\theta}_{24} = 3^\circ$ (left panels) and $\bar{\theta}_{24} = 5^\circ$ (right panels). Blue dashed lines stand for the $L = 3000$ km baseline; red dashed lines stand for the $L = 7500$ km baseline; black dashed lines stand for the combination of both baselines.

In the numerical analysis, the following parameters in the four-family model have been kept fixed to their central values: $\theta_{12} = 34^\circ$, $\theta_{13} = 0$; $\Delta m_{\text{sol}}^2 = 7.9 \times 10^{-5} \text{ eV}^2$; $\Delta m_{31}^2 = \Delta m_{\text{atm}}^2 = 2.4 \times 10^{-3} \text{ eV}^2$; $\delta_1 = \delta_2 = 0$. Eventually, $\Delta m_{\text{SBL}}^2 = 1 \text{ eV}^2$ and $\theta_{14} = 0^\circ$. For simplicity, we have fixed $\theta_{23} = 45^\circ$. We do not expect any "octant degeneracies", thus. The input values that we have studied to illustrate the discovery potential of our setup are: $\bar{\theta}_{34} = 20^\circ, 30^\circ$; $\bar{\delta}_3 = 90^\circ$ (upper panels) and $\bar{\delta}_3 = 200^\circ$ (lower panels). Matter effects have been included considering, as always, a constant matter density $\rho = 3.4 \text{ g/cm}^3$ for the shortest baseline and $\rho = 4.3 \text{ g/cm}^3$ for the longest one, computed averaging over the density profile in the PREM [86] along the neutrino path.

First of all, we can see that the combination of the two channels at the shortest baseline (blue lines) is not enough to solve the sign degeneracies (labeled with "SD" in the plot), that can be observed for all of the choices of the three input parameters $(\bar{\theta}_{24}, \bar{\theta}_{34}, \bar{\delta}_3)$. The sign clones are located at the point $(\theta_{34}^{\text{SD}}, \delta_3^{\text{SD}})$, where $\theta_{34}^{\text{SD}} \sim \bar{\theta}_{34}$ and δ_3^{SD} satisfies the relation $\sin \bar{\delta}_3 \sin \Delta_{31} L = -\sin \delta_3^{\text{SD}} \sin \Delta_{31} L$, with $\delta_3^{\text{SD}} \sim -90^\circ$ for $\bar{\delta}_3 = 90^\circ$ and $\delta_3^{\text{SD}} \sim 20^\circ$ for $\bar{\delta}_3 = 200^\circ$. The intrinsic degeneracy is also found for one specific choice of the input parameter $(\bar{\theta}_{24} = 3^\circ, \bar{\theta}_{34} = 20^\circ, \bar{\delta}_3 = 200^\circ)$. On the other hand, no intrinsic or sign degeneracy are found at the longest baseline (red lines). When combining the two baselines we see that the degeneracies are solved and that a very good precision on the simultaneous measurement of θ_{34} and δ_3 is achieved for all the choices of the input parameters that we have considered. In particular, the error in δ_3 at the 99% CL is of the order of a few tens of degrees. At the same time, the mixing angle θ_{34} can be measured for these particular inputs with a precision of a few degrees.

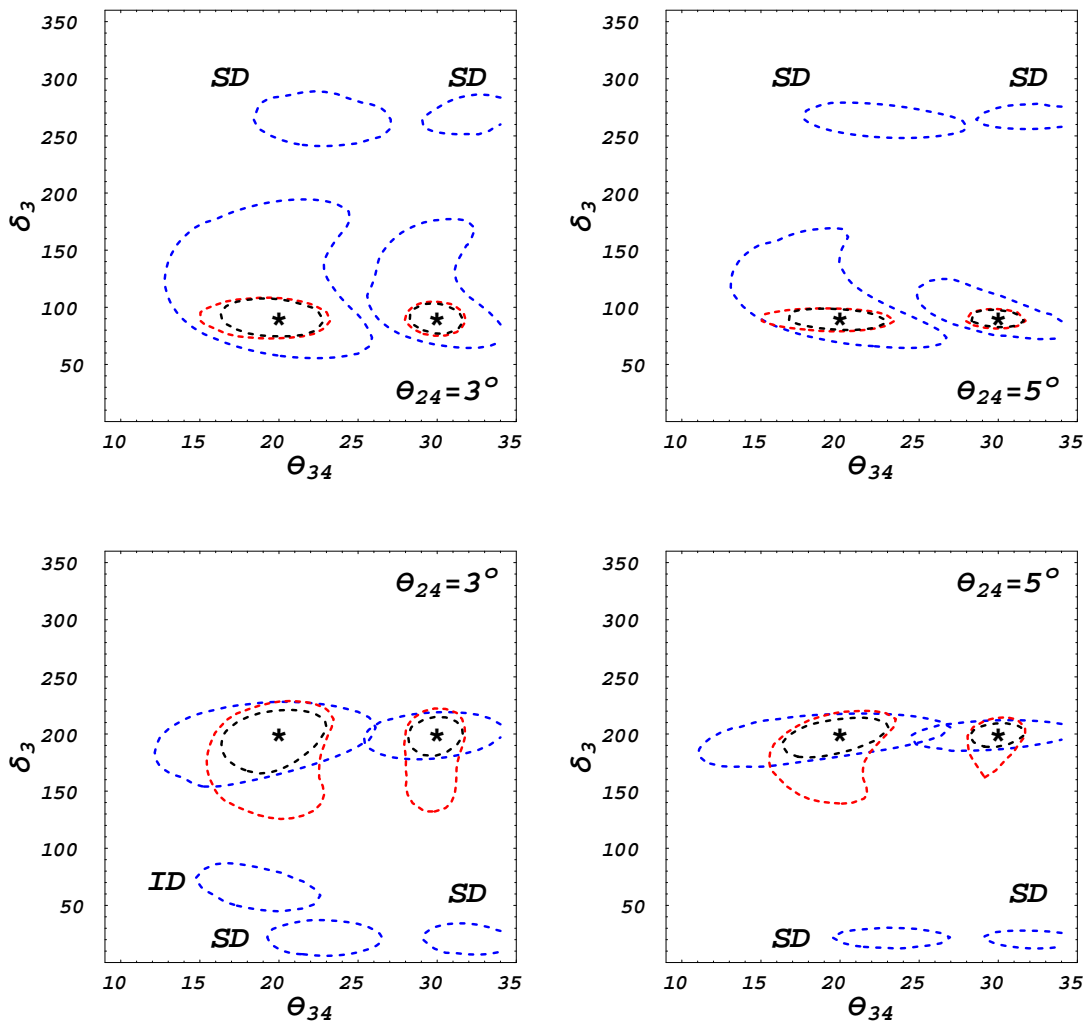


Figure 12. 99% CL contours for the simultaneous measurement of θ_{34} and δ_3 using the combined data from the ν_μ disappearance and the $\nu_\mu \rightarrow \nu_\tau$ discovery channels. Two different values of θ_{24} have been considered: $\theta_{24} = 3^\circ$ (left panels); $\theta_{24} = 5^\circ$ (right panels). The input pairs $(\bar{\theta}_{34}, \bar{\delta}_3)$, marked by a star in the plots, are: $\bar{\theta}_{34} = 20^\circ, 30^\circ; \bar{\delta}_3 = 90^\circ$ (upper panels) and 200° (lower panels). In the plots, "ID" stands for "Intrinsic Degeneracy"; "SD" stands for "Sign Degeneracy". Blue dashed lines represent the $L = 3000$ km baseline data; red dashed lines the $L = 7500$ km baseline data; black dashed lines stand for the combination of both baselines.

We summarize our results for the simultaneous measurement of θ_{34} and δ_3 in figure 13, where the 99% CL " δ_3 -discovery potential" in the (θ_{34}, δ_3) -plane for different values of $\bar{\theta}_{24}$ is shown.¹⁴ We define the " δ_3 -discovery potential" as the region in the $(\sin^2 2\theta_{34}, \delta_3)$ -plane for which a given (non-zero) value of the CP-violating phase δ_3 can be distinguished at the 99% CL (for 2 d.o.f.'s) from the CP-conserving case, i.e., $\delta_3 = 0, \pi$. Note that we have also taken into account the effects of the sign degeneracy in this analysis.

¹⁴Notice that, as we stressed at the beginning of this section, sensitivity to δ_3 is lost when the product $s_{24}s_{34}$ is smaller than $(s_{24}s_{34})_{\min} \sim 0.01$.

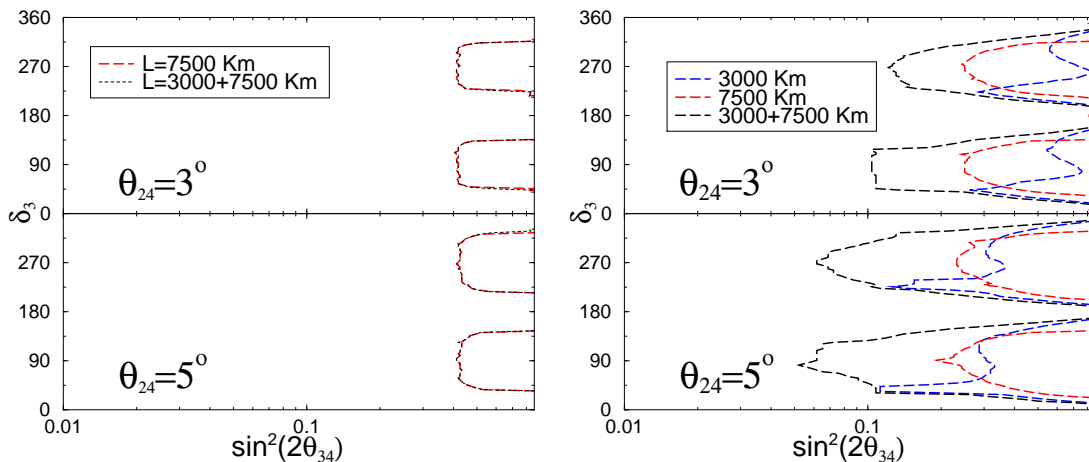


Figure 13. The 99 % CL “ δ_3 -discovery potential” in the (θ_{34}, δ_3) -plane. Left: only $\nu_\mu \rightarrow \nu_\mu$ disappearance channel data; Right: combination of $\nu_\mu \rightarrow \nu_\mu$ disappearance and $\nu_\mu \rightarrow \nu_\tau$ appearance channels data. Upper panels have been obtained for $\bar{\theta}_{24} = 3^\circ$; lower panels for $\bar{\theta}_{24} = 5^\circ$. Blue dashed lines stand for $L = 3000$ km baseline data; red dashed lines stand for $L = 7500$ km baseline data; black dashed lines stand for the combination of the two baselines.

In the left panel, only data from the $\nu_\mu \rightarrow \nu_\mu$ disappearance channel are shown. In the right panel, we have combined data from the ν_μ disappearance channel with those from the $\nu_\mu \rightarrow \nu_\tau$ appearance channel. Upper panels refer to $\bar{\theta}_{24} = 3^\circ$; lower panels to $\bar{\theta}_{24} = 5^\circ$. Blue dashed lines stand for the $L = 3000$ km baseline; red dashed lines stand for the $L = 7500$ km baseline; eventually, black dashed lines stand for the combination of the two baselines.

We can see from figure 13 (left) that, using ν_μ disappearance channel only, we are able to measure a non-vanishing δ_3 for values of θ_{34} above $\sin^2 2\theta_{34} \geq 0.4$ ($\theta_{34} \geq 18^\circ$). The CP-coverage¹⁵ is $\sim 50\%$, with a very smooth dependence on θ_{34} , being a bit larger for larger $\bar{\theta}_{24}$. We can also see that the detector at $L = 3000$ km have no δ_3 -sensitivity whatsoever.

The situation is completely different when the $\nu_\mu \rightarrow \nu_\tau$ discovery channel data are added to the ν_μ disappearance ones, figure 13 (right). First of all, we see that the $L = 3000$ km detector is no longer useless to measure δ_3 : spikes of δ_3 -sensitivity for particular values of δ_3 can be observed, in some cases outperforming the far detector results. However, it is in the combination of the two baselines where we can see that a dramatic improvement in the δ_3 -discovery potential is achievable. When the $\nu_\mu \rightarrow \nu_\tau$ data are included, a non-vanishing δ_3 can be measured for values of θ_{34} as small as $\sin^2 2\theta_{34} = 0.06$ ($\theta_{34} = 7^\circ$) for $\bar{\theta}_{24} = 5^\circ$ and $\sin^2 2\theta_{34} = 0.10$ ($\theta_{34} = 9^\circ$) for $\bar{\theta}_{24} = 3^\circ$. For $\sin^2 2\theta_{34} \geq 0.4$ ($\theta_{34} \geq 20^\circ$), roughly 80% (60%) of CP-coverage is achieved for $\bar{\theta}_{24} = 5^\circ$ (3°). The striking improvement in the δ_3 -discovery potential is a consequence of the synergy of the two channels and of the two baselines, whose combination is able to solve most of the correlations that otherwise strongly limits the potential of the ν_μ disappearance channel. For completeness, we also present in figure 14 results for the sensitivity of the golden and silver channels to the phase

¹⁵The CP-coverage is the fraction of the δ_3 -parameter space for which we are able to exclude $\delta_3 = 0, \pi$ at the 99% CL for a given value of θ_{34} .

δ_2 , that reduces to the three-family CP-violating phase δ in the limit $\theta_{i4} \rightarrow 0$. A comment is in order: as it can be seen from eq. (4.5), using the parametrization in eq. (2.2), the golden channel oscillation probability in vacuum depends on the combination $(\delta_2 - \delta_3)$ up to the eighth-order in ϵ . This means that, in the (3+1)-model, a CP-conserving result in the golden channel may be found for non-vanishing values of δ_2 and δ_3 if $\delta_1 = 0$; $(\delta_2 - \delta_3) = 0, \pi$. This degeneracy can be broken only by adding new information, such as that obtained using the silver channel, see eq. (4.6), ν_μ disappearance or $\nu_\mu \rightarrow \nu_\tau$ appearance data. Golden channel data at the $L = 3000$ km baseline may not be able, thus, to detect a non-vanishing CP-violating signal even when both δ_2, δ_3 are different from $0, \pi$.

The contours in the $(\theta_{13}^{(4fam)}, \delta_2)$ -plane have been obtained as follows: we have first computed the expected number of events for $\nu_e \rightarrow \nu_\mu$ and $\nu_e \rightarrow \nu_\tau$ oscillations in the four-family model for particular choices of the relevant parameters, $\theta_{13}^{(4fam)} = \bar{\theta}_{13}^{(4fam)}$ and $\delta_2 = \bar{\delta}_2$. We have then computed the expected number of events in the $(\theta_{13}^{(4fam)}, \delta_2)$ -plane for the same oscillation channels in the four-family model, varying $\theta_{13}^{(4fam)} \in [0, 10^\circ]$ and $\delta_2 \in [0, 360^\circ]$. The $\Delta\chi^2$ is then computed as follows:

$$\Delta\chi^2 = \left(\sum_j \left[N_j(\theta_{13}^{(4fam)}, \delta_2) - N_j(\bar{\theta}_{13}^{(4fam)}, \bar{\delta}_2) \right]^2 / \sigma_j^2 \right) \quad (4.13)$$

where the minimum of the χ^2 is, trivially, obtained for $\theta_{13}^{(4fam)} = \bar{\theta}_{13}^{(4fam)}$; $\delta_2 = \bar{\delta}_2$. As before, j runs over the different signals: the $\nu_e \rightarrow \nu_\mu$ and the $\nu_e \rightarrow \nu_\tau$ data, divided into 10 energy bins, for the two baselines and the two possible stored muons polarities. The variance σ_j is defined by eq. (4.4), with $f_j = 2\%$ for the golden channel and 10% for the silver channel. No correlated systematic errors have been considered in the plots of this section. The region in the $(\theta_{13}^{(4fam)}, \delta_2)$ -plane compatible with the input values $(\bar{\theta}_{13}^{(4fam)}, \bar{\delta}_2)$ at the 2 d.o.f.'s 99% CL is eventually defined by drawing the contour line corresponding to $\Delta\chi^2 = 9.21$.

Results have been obtained for $\bar{\theta}_{13}^{(4fam)} = 2^\circ, 5^\circ$ and $\bar{\delta}_2 = 90^\circ, 250^\circ$. The other parameters are: $\theta_{12} = 34^\circ$; $\theta_{23} = 45^\circ$; $\Delta m_{21}^2 = 7.9 \times 10^{-5} \text{ eV}^2$, $\Delta m_{31}^2 = 2.4 \times 10^{-3} \text{ eV}^2$ and $\Delta m_{41}^2 = 1 \text{ eV}^2$. For simplicity, we show results for $\delta_1 = \delta_3 = 0$ in these plots (remember that the measured phase should be interpreted as $\delta = (\delta_2 - \delta_3)$ for $\delta_1 = 0$). Eventually, the three active-sterile mixing angles are: $\theta_{14} = \theta_{24} = 5^\circ$; $\theta_{34} = 20^\circ$ in figure 14 (left); and $\theta_{14} = \theta_{24} = \theta_{34} = 10^\circ$ in figure 14 (right). In the plots, golden and silver channels data are always summed. Four-family results are shown for the two baselines separately and summed: blue dashed lines stand for the $L = 3000$ km baseline data; red dashed lines stand for the $L = 7500$ km baseline data; black dashed lines stand for the combination of all data. For comparison, black solid lines stand for the three-family results for the combination of the baselines. We can see from the plots in figure 14 (left) that, when the active-sterile mixing angles θ_{14} and θ_{24} are "small", the four-family results are extremely similar to those obtained by a fit in the three-family model.¹⁶ The 99% CL contours in the four-family model are slightly larger than the three-family ones. The shape of contours

¹⁶ Results do not depend significantly on θ_{34} : as it can be seen in eqs. (4.5) and (4.6), this angle only enters in the silver channel oscillation probability, statistically less relevant than the golden channel data.

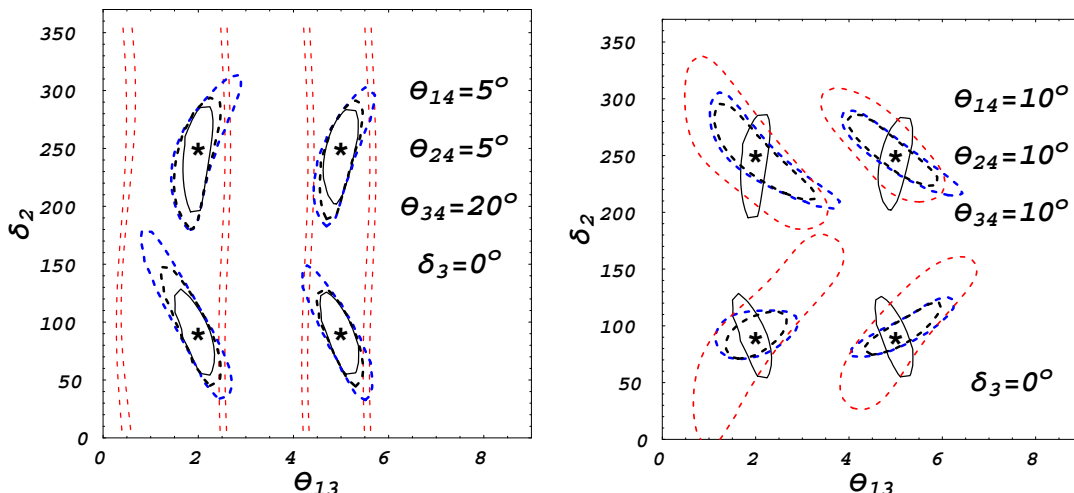


Figure 14. 99% CL contours for the simultaneous measurement of θ_{13} and δ_2 using the combined data from the $\nu_e \rightarrow \nu_\mu$ and the $\nu_e \rightarrow \nu_\tau$ golden and silver channels. Two different choices of the active-sterile mixing angles have been considered: $\theta_{14} = \theta_{24} = 5^\circ; \theta_{34} = 20^\circ$ (left panel); $\theta_{14} = \theta_{24} = \theta_{34} = 10^\circ$ (right panel). The input pairs (θ_{13}, δ_2) , marked by a star in the plots, are: $\bar{\theta}_{13} = 2^\circ, 5^\circ; \bar{\delta}_2 = 90^\circ, 250^\circ$. Golden and silver channels data are always summed. Four-family results are shown for the two baseline separately and summed: blue dashed lines stand for the $L = 3000$ km baseline data; red dashed lines stand for the $L = 7500$ km baseline data; black dashed lines stand for the combination of all data. Eventually, black solid lines stand for the three-family results for the combination of the baselines.

in the $(\theta_{13}^{(4\text{fam})}, \delta_2)$ -plane is identical for the four- and three-family. This means that the correlation between the two parameters is not modified by contributions proportional to θ_{14}, θ_{24} with respect to three-family expressions.

In figure 14 (right) we see that, when θ_{14} and θ_{24} assume values near their upper bound, the results for the four-family contours can significantly differ from the three-family ones. In particular, the four-family contours in the $(\theta_{13}^{(4\text{fam})}, \delta_2)$ -plane are orthogonal to the three-family ones. This is easily understood by looking at the approximated expressions for the oscillation probabilities of the golden and silver channels expanded to order ϵ^8 in section 4.1. As we can see, the two terms with a δ_2 -dependence in the second and third lines of eq. (4.5) are proportional to $s_{13}s_{14}s_{24} \sin(\delta_2 + \Delta_{31}L/2)$ and to $s_{13}(\Delta_{21}L) \cos(\delta_2 + \Delta_{31}L/2)$, respectively. When the first term becomes as large as the solar-suppressed one, the two terms give a destructive interference. Eventually, if the first term becomes larger than the second, the $(\theta_{13}^{(4\text{fam})}, \delta_2)$ -correlation changes, becoming orthogonal to the three-family-like one, as it can be seen in the figure. Notice that, when θ_{14} and θ_{24} assume values near their upper bound, there is a little sensitivity to the CP-phases at the longer baseline. Since this baseline corresponds to the magic baseline, we can conclude that this is an effect characteristic to the four neutrino scheme.

5 Conclusions

We have studied the potential of a Neutrino Factory to search for signature of the (3+1)-scheme, where the largest mass squared difference Δm_{SBL}^2 can be any value larger than 0.1 eV^2 , as long as oscillations driven by Δm_{SBL}^2 are averaged for the range of the energy and the baseline at a Neutrino Factory. From the analytic expressions of the oscillation probabilities, we have seen that the disappearance channel $\nu_\mu \rightarrow \nu_\mu$ and the “*discovery channel*” $\nu_\mu \rightarrow \nu_\tau$ are extremely powerful in constraining the parameter space of the (3+1)-scheme.

We have performed a numerical analysis of the sensitivity to sterile neutrinos in two setups: (a) A Neutrino Factory with the muon energy $E_\mu = 50 \text{ GeV}$, 2×10^{20} useful muon decays per year per baseline, with two detectors located at $L = 3000 \text{ km}$ and $L = 7500 \text{ km}$ from the source, respectively; (b) The setup suggested in the final ISS Physics Report, i.e., a Neutrino Factory with $E_\mu = 20 \text{ GeV}$, 5×10^{20} useful muon decays per year per baseline, with two detectors located at $L = 4000 \text{ km}$ and $L = 7500 \text{ km}$ from the source, respectively. The two detectors are of the Hybrid-MIND type (50 kton MIND + 4 kton MECC). In both cases we have assumed data taking for 4 years for both muon polarities. We have carefully taken into account the relevant backgrounds, efficiencies and systematic errors and our analysis is, thus, much more detailed than in previous studies in the literature.

We have looked at the sensitivity to θ_{13} , θ_{14} , analyzing the golden and silver channels. While Neutrino Factories do not give any useful constraint on θ_{14} when marginalizing over θ_{24} and θ_{34} , as in the case of the three-flavor framework, they give quite a strong constraint on $\sin^2 2\theta_{13}$, down to 7×10^{-5} (2×10^{-4}) for the 50 GeV (20 GeV) case with a slight dependence on θ_{14} . In the present work we did not assume any near detector, since the issue has not yet been studied in detail (see [123]). If we put a near detector, then we should be able to give a constraint on θ_{14} because the near detector will give us information on how much neutrino oscillations occur due to the largest mass squared difference Δm_{SBL}^2 . Further studies on the near detector will be necessary to obtain quantitative results on θ_{14} .

Combining the disappearance and discovery channels, we have found that both the 50 GeV (20 GeV) Neutrino Factories can constrain θ_{34} and θ_{24} down to 12° (14°) and 7.5° (8°), respectively, marginalizing over all other four-family parameters. If we closely look at the details, then we found some difference between the performances of the 50 GeV and 20 GeV Neutrino Factories, such as the sensitivity plot in the $(\theta_{24}, \theta_{34})$ -plane or the regions in the $(\theta_{24}, \theta_{34})$ - and $(\theta_{13}^{(4\text{fam})}, \theta_{14})$ -planes where the three-flavor mixing hypothesis is excluded, where the sensitivity of the 50 GeV Neutrino Factory is always a bit better because the $\nu_\mu \rightarrow \nu_\tau$ channel, which becomes more important at higher energies, makes this difference. The present results should be compared to the previous study [60] on the CNGS experiment, which cannot improve the present bound on θ_{24} and θ_{34} , if running at the nominal luminosity. The sensitivity to θ_{24} and θ_{34} of the Neutrino Factory setups proposed in this paper is better than the potential sensitivity of the CNGS experiment even if the CNGS beam intensity would be increased by a factor 10.

We have also discussed dependence of the sensitivity of the four channels on the systematic errors. The sensitivities of the golden and silver channels depend mainly on the

correlated systematic error σ_α on the overall normalization. As for the disappearance and discovery channels, the sensitivity of the former depends on the bin-to-bin uncorrelated error f_j and σ_α , whereas that of the latter depends mainly on f_j . To take advantage of the discovery channel, it is necessary to reduce f_j below 10%. To this purpose, the expertise on ECC technology that will be gained after the first years of OPERA data taking will be of great importance.

On the other hand, in the case where we have a positive signal of the sterile neutrino mixing, we have found that we can measure the new CP phase δ_3 by combining the disappearance and discovery channels at the two baselines, where information from the $L = 7500$ km baseline plays a dominant role in resolving parameter degeneracy. After combination of the two channels and the two baselines, the CP-violating phase δ_3 can be measured at 99% CL for values of $\sin^2 2\theta_{34} \geq 0.06$ (notice that, using only the disappearance channel at the two baseline, δ_3 can be measured at 99% CL for $\sin^2 2\theta_{34} \geq 0.4$, only). It should be emphasized that the measurement of CP-violation in the $\nu_\mu \rightarrow \nu_\tau$ channel is a clear new signal of CP-violation associated to the sterile neutrino scheme. We have also found that the measurement of the three-family-like CP-violating phase δ_2 is modified by the presence of non-vanishing active-sterile mixing angles.

While our works contain some results on parameter degeneracy in the (3+1)-scheme, the problem on the general structure of parameter degeneracy in the four neutrino schemes is beyond the scope of the present paper and should be pursued in future.

Finally, we would like to stress that, while the discovery channel at a Neutrino Factory is not very useful for the measurements of the three-flavor oscillation parameters, it is a very important channel to search for new physics beyond the standard scenario. The discovery channel at a Neutrino Factory deserves, thus, further studies.

A The mixing matrix elements $U_{\alpha j}$

The mixing matrix elements in the parametrization (2.2) are given by the following:

$$\begin{cases} U_{e1} = c_{12}c_{13}c_{14} \\ U_{e2} = c_{13}c_{14}s_{12}e^{-i\delta_1} \\ U_{e3} = c_{14}s_{13}e^{-i\delta_2} \\ U_{e4} = s_{14} \end{cases} \quad (\text{A.1})$$

$$\begin{cases} U_{\mu 1} = -c_{23}c_{24}s_{12}e^{i\delta_1} - c_{12} [c_{24}s_{13}s_{23}e^{i(\delta_2-\delta_3)} + c_{13}s_{14}s_{24}] \\ U_{\mu 2} = c_{12}c_{23}c_{24} - s_{12}e^{-i\delta_1} [c_{24}s_{13}s_{23}e^{i(\delta_2-\delta_3)} + c_{13}s_{14}s_{24}] \\ U_{\mu 3} = c_{13}c_{24}s_{23}e^{-i\delta_3} - s_{13}s_{14}s_{24}e^{-i\delta_2} \\ U_{\mu 4} = c_{14}s_{24} \end{cases} \quad (\text{A.2})$$

$$\begin{cases} U_{\tau 1} = s_{12}e^{i\delta_1} [c_{34}s_{23}e^{i\delta_3} + c_{23}s_{24}s_{34}] \\ \quad - c_{12} \{c_{13}c_{24}s_{14}s_{34} + s_{13}e^{i\delta_2} [c_{23}c_{34} - s_{23}s_{24}s_{34}e^{-i\delta_3}]\} \\ U_{\tau 2} = -c_{12} [c_{34}s_{23}e^{i\delta_3} + c_{23}s_{24}s_{34}] \\ \quad - s_{12}e^{-i\delta_1} \{c_{13}c_{24}s_{14}s_{34} + s_{13}e^{i\delta_2} [c_{23}c_{34} - s_{23}s_{24}s_{34}e^{-i\delta_3}]\} \\ U_{\tau 3} = -c_{24}s_{13}s_{14}s_{34}e^{-i\delta_2} + c_{13} [c_{23}c_{34} - s_{23}s_{24}s_{34}e^{-i\delta_3}] \\ U_{\tau 4} = c_{14}c_{24}s_{34} \end{cases} \quad (\text{A.3})$$

$$\begin{cases} U_{s1} = s_{12}e^{i\delta_1} [c_{23}c_{34}s_{24} - s_{23}s_{34}e^{i\delta_3}] \\ \quad - c_{12} \{c_{13}c_{24}c_{34}s_{14} - s_{13}e^{i\delta_2} [c_{34}s_{23}s_{24}e^{-i\delta_3} + c_{23}s_{34}]\} \\ U_{s2} = -c_{12} [c_{23}c_{34}s_{24} - s_{23}s_{34}e^{i\delta_3}] \\ \quad - s_{12}e^{-i\delta_1} \{c_{13}c_{24}c_{34}s_{14} - s_{13}e^{i\delta_2} [c_{34}s_{23}s_{24}e^{-i\delta_3} + c_{23}s_{34}]\} \\ U_{s3} = -c_{24}c_{34}s_{13}s_{14}e^{-i\delta_2} - c_{13} [c_{34}s_{23}s_{24}e^{-i\delta_3} + c_{23}s_{34}] \\ U_{s4} = c_{14}c_{24}c_{34} \end{cases} \quad (\text{A.4})$$

where $c_{ij} = \cos \theta_{ij}$ and $s_{ij} = \sin \theta_{ij}$.

B Oscillation probabilities by the KTY formalism

To derive the expressions for the oscillation probabilities in matter, we use the KTY formalism which has been introduced in ref. [62, 63].¹⁷ The evolution equation of flavor eigenstates¹⁸ is:

$$i \frac{d}{dt} |\nu_\alpha\rangle = \mathcal{H}_{\alpha\beta} |\nu_\beta\rangle \equiv [U\mathcal{E}U^\dagger + \mathcal{A}]_{\alpha\beta} |\nu_\beta\rangle,$$

where

$$\mathcal{E} = \text{diag} \left(0, \frac{\Delta m_{21}^2}{2E}, \frac{\Delta m_{31}^2}{2E}, \frac{\Delta m_{41}^2}{2E} \right) \equiv \text{diag}(0, \Delta_{21}, \Delta_{31}, \Delta_{41}), \quad (\text{B.1})$$

$$\mathcal{A} = \sqrt{2} G_F \text{diag}(n_e, 0, 0, n_n/2) \equiv \text{diag}(A_e, 0, 0, A_n),$$

$\Delta_{ij} = \Delta m_{ij}^2/2E$, and n_e and n_n are respectively the electron and neutron densities. In eq. (B.1), we have subtracted from \mathcal{H} the term $E_1 \mathbf{1} = \sqrt{E^2 + m_1^2} \mathbf{1}$, which contributes only to the phase of the oscillation amplitude and therefore does not affect the probability. In the KTY formalism, the oscillation probabilities in matter assume the following form:

$$P_{\alpha\beta} = \delta_{\alpha\beta} - 4 \sum_{i<j} \text{Re}(\tilde{X}_i^{\alpha\beta} \tilde{X}_j^{\alpha\beta*}) \sin^2 \left(\frac{\Delta \tilde{E}_{ij} L}{2} \right) + 2 \sum_{i<j} \text{Im}(\tilde{X}_i^{\alpha\beta} \tilde{X}_j^{\alpha\beta*}) \sin(\Delta \tilde{E}_{ij} L), \quad (\text{B.2})$$

where $\Delta \tilde{E}_{ji} \equiv \tilde{E}_j - \tilde{E}_i$ and $\tilde{X}_j^{\alpha\beta} \equiv \tilde{U}_{\alpha j} \tilde{U}_{\beta j}^*$ ($j = 1, 2, 3, 4$). \tilde{E}_i and $\tilde{U}_{\alpha i}$ are the \mathcal{H} eigenvalues and the effective mixing matrix in matter, respectively, defined through

$$\mathcal{H} = \tilde{U} \text{diag}(\tilde{E}_j) \tilde{U}^\dagger.$$

The $\tilde{X}_j^{\alpha\beta}$ matrices can be expressed as follows:

$$\tilde{X}_j^{\alpha\beta} \equiv \sum_l (V^{-1})_{jl} [\mathcal{H}^{l-1}]_{\alpha\beta} = \sum_l (V^{-1})_{jl} \left[(U\mathcal{E}U^\dagger + \mathcal{A})^{l-1} \right]_{\alpha\beta}, \quad (\text{B.3})$$

where V is the Vandermonde matrix:

$$V = \begin{pmatrix} 1 & 1 & 1 & 1 \\ \tilde{E}_1 & \tilde{E}_2 & \tilde{E}_3 & \tilde{E}_4 \\ \tilde{E}_1^2 & \tilde{E}_2^2 & \tilde{E}_3^2 & \tilde{E}_4^2 \\ \tilde{E}_1^3 & \tilde{E}_2^3 & \tilde{E}_3^3 & \tilde{E}_4^3 \end{pmatrix},$$

¹⁷ Another proof of the KTY formalism was given in ref. [124, 125] and it was extended to four neutrino schemes in ref. [126].

¹⁸ Greek (Latin) indices label the flavor (mass) basis: $\alpha = e, \mu, \tau, s$ ($i = 1, 2, 3, 4$).

whose determinant is $\prod_{i < j} \Delta \tilde{E}_{ji}$. The inverse of V can then be easily obtained as long as we know the eigenvalues \tilde{E}_j of the effective Hamiltonian in matter \mathcal{H} , expressed in terms of A_e , A_n and the vacuum parameters:

$$V^{-1} = \begin{pmatrix} \frac{1}{\Delta \tilde{E}_{21} \Delta \tilde{E}_{31} \Delta \tilde{E}_{41}} (\tilde{E}_2 \tilde{E}_3 \tilde{E}_4, -(\tilde{E}_2 \tilde{E}_3 + \tilde{E}_3 \tilde{E}_4 + \tilde{E}_4 \tilde{E}_2), \tilde{E}_2 + \tilde{E}_3 + \tilde{E}_4, -1) \\ \frac{-1}{\Delta \tilde{E}_{21} \Delta \tilde{E}_{32} \Delta \tilde{E}_{42}} (\tilde{E}_3 \tilde{E}_4 \tilde{E}_1, -(\tilde{E}_3 \tilde{E}_4 + \tilde{E}_4 \tilde{E}_1 + \tilde{E}_1 \tilde{E}_3), \tilde{E}_3 + \tilde{E}_4 + \tilde{E}_1, -1) \\ \frac{1}{\Delta \tilde{E}_{31} \Delta \tilde{E}_{32} \Delta \tilde{E}_{43}} (\tilde{E}_4 \tilde{E}_1 \tilde{E}_2, -(\tilde{E}_4 \tilde{E}_1 + \tilde{E}_1 \tilde{E}_2 + \tilde{E}_2 \tilde{E}_4), \tilde{E}_4 + \tilde{E}_1 + \tilde{E}_2, -1) \\ \frac{-1}{\Delta \tilde{E}_{41} \Delta \tilde{E}_{42} \Delta \tilde{E}_{43}} (\tilde{E}_1 \tilde{E}_2 \tilde{E}_3, -(\tilde{E}_1 \tilde{E}_2 + \tilde{E}_2 \tilde{E}_3 + \tilde{E}_3 \tilde{E}_1), \tilde{E}_1 + \tilde{E}_2 + \tilde{E}_3, -1) \end{pmatrix}. \tag{B.4}$$

Within the KTY formalism, thus, we only need to compute the eigenvalues of \mathcal{H} to derive the oscillation probabilities in matter.

A possible drawback of this approach is that the physical understanding of the oscillation probabilities (i.e. the dependence on the vacuum mixing matrix parameters) is encoded in the explicit expressions for the \tilde{X} coefficients. To make contact with the parameters to be measured in a manageable way, we thus need to introduce some approximations in the computation of the eigenvalues \tilde{E}_i and of the corresponding matrices $\tilde{X}_i^{\alpha\beta}$. Now, considering the present constraints from [60] in the standard and sterile small parameters, we see that θ_{13}, θ_{14} and θ_{24} cannot be much larger than 10° while the third active-sterile mixing angle, θ_{34} , can be as large as $\theta_{34} \sim 35^\circ$. Notice also that the present constraint on the θ_{23} deviation from the maximal mixing, $\delta\theta_{23} \equiv \theta_{23} - \pi/4$, is of the same order as those on θ_{13}, θ_{14} and θ_{24} . On the other hand, the solar and atmospheric mass differences, $\Delta m_{\text{sol}}^2, \Delta m_{\text{atm}}^2$, are much smaller than Δm_{SBL}^2 . In what follows, therefore, we expand all the quantities in power of a small parameter ϵ , and keep terms of cubic order in ϵ , where the small parameter is defined by

$$\begin{aligned} \epsilon &\equiv \theta_{34} \sim \sqrt{\theta_{13}} \sim \sqrt{\theta_{14}} \sim \sqrt{\theta_{24}} \sim \sqrt{\delta\theta_{23}} \lesssim 4 \times 10^{-1}, \\ \eta_2 &\equiv \Delta m_{21}^2 / \Delta m_{41}^2 \lesssim 10^{-4}, \\ \eta_3 &\equiv \Delta m_{31}^2 / \Delta m_{41}^2 \lesssim 10^{-3}, \\ \eta_{e(n)} &\equiv A_{e(n)} / \Delta E_{41} \lesssim 10^{-3}. \end{aligned}$$

Notice that, to third order in ϵ , in the expansion in the probabilities we have neglected all terms proportional to $\eta_{e,n,2,3}$. Although this can be a rather rough approximation, as we have seen before, it is very useful in order to understand the different physics potential of the various oscillation channels. Thus we have the following probabilities to third order in ϵ :

$$\begin{aligned} P_{ee} &\sim 1 + O(\epsilon^4), \\ P_{e\mu} &\sim P_{e\tau} \sim P_{es} \sim O(\epsilon^4), \\ P_{\mu\mu} &= 1 - \sin^2 \frac{\Delta_{31} L}{2} - 2(A_n L) s_{24} s_{34} \cos \delta_3 \sin \Delta_{31} L + O(\epsilon^4), \end{aligned}$$

$$\begin{aligned}
P_{\mu\tau} &= (1 - s_{34}^2) \sin^2 \frac{\Delta_{31}L}{2} + \{s_{24} s_{34} \sin \delta_3 + 2 (A_n L) s_{24} s_{34} \cos \delta_3\} \sin \Delta_{31}L \\
&\quad + O(\epsilon^4), \\
P_{\mu s} &= s_{34}^2 \sin^2 \frac{\Delta_{31}L}{2} - s_{24} s_{34} \sin \delta_3 \sin \Delta_{31}L + O(\epsilon^4).
\end{aligned}$$

In section 4.1 we had to go beyond $O(\epsilon^3)$ in order to explain our numerical results using the golden and silver channels. To this purpose, in the text we have shown the approximated expressions for $P_{e\mu}$ and $P_{e\tau}$ to order ϵ^8 in vacuum. To check unitarity of the four-family PMNS matrix at this order in ϵ , it is useful to show here the P_{es} oscillation probability, also:

$$\begin{aligned}
P_{es} &= 2\theta_{14}^2(1 - \theta_{14}^2 - \theta_{24}^2 - \theta_{34}^2) \\
&\quad + 2\{\theta_{13}^2(-2\theta_{14}^2 + \theta_{24}^2 + \theta_{34}^2 - 2\delta\theta_{23}\theta_{34}^2) + \theta_{13}^2\theta_{24}\theta_{34} \cos \delta_3\} \sin^2 \frac{\Delta_{31}L}{2} \\
&\quad - 2\sqrt{2}\theta_{13}\theta_{14}\theta_{24}(1 + \delta\theta_{23} - \theta_{34}^2) \sin\left(\delta_2 - \delta_3 + \frac{\Delta_{31}L}{2}\right) \sin \frac{\Delta_{31}L}{2} \\
&\quad - 2\sqrt{2}\theta_{13}\theta_{14}\theta_{34}\left(1 - \delta\theta_{23} - \frac{\theta_{34}^2}{2}\right) \sin\left(\delta_2 + \frac{\Delta_{31}L}{2}\right) \sin \frac{\Delta_{31}L}{2} \\
&\quad - \sin 2\theta_{12}\theta_{13}\theta_{34}^2(\Delta_{21}L) \cos\left(\delta_1 - \delta_2 + \delta_3 - \frac{\Delta_{31}L}{2}\right) \sin \frac{\Delta_{31}L}{2} \\
&\quad + \frac{1}{\sqrt{2}} \sin 2\theta_{12}\theta_{14}\theta_{34}(\Delta_{21}L) \sin(\delta_1 + \delta_3) - \frac{1}{\sqrt{2}} \sin 2\theta_{12}\theta_{14}\theta_{24}(\Delta_{21}L) \sin \delta_1.
\end{aligned}$$

As a final analytical contribution, we have calculated approximate probabilities associated to the channels under study, $P_{\mu\mu}$ and $P_{\mu\tau}$ (together with $P_{\mu s}$), to fourth order in ϵ but neglecting θ_{13} and θ_{14} :

$$\begin{aligned}
P_{\mu\mu} &= 1 - 2\theta_{24}^2 - \left[1 - 4(\delta\theta_{23})^2 - 2\theta_{24}^2 + \theta_{34}^2 \frac{A_n}{\Delta_{31}} \left(4\delta\theta_{23} - \theta_{34}^2 \frac{A_n}{\Delta_{31}}\right)\right] \sin^2 \frac{\Delta_{31}L}{2} \\
&\quad - (A_n L) \left\{2\theta_{24}\theta_{34} \cos \delta_3 - \frac{\theta_{34}^2}{2} \left(4\delta\theta_{23} - \theta_{34}^2 \frac{A_n}{2\Delta_{31}}\right)\right\} \sin \Delta_{31}L + O(\epsilon^5), \\
P_{\mu\tau} &= \left\{1 - 4(\delta\theta_{23})^2 - \theta_{24}^2 - \theta_{34}^2 \left[1 - \frac{\theta_{34}^2}{3} - \frac{A_n}{\Delta_{31}} \left(4\delta\theta_{23} - \theta_{34}^2 \frac{A_n}{\Delta_{31}}\right)\right]\right\} \sin^2 \frac{\Delta_{31}L}{2} \\
&\quad + \left\{\theta_{24}\theta_{34} \sin \delta_3 + (A_n L) \left[2\theta_{24}\theta_{34} \cos \delta_3 - \frac{\theta_{34}^2}{2} \left(4\delta\theta_{23} - \theta_{34}^2 \frac{A_n}{2\Delta_{31}}\right)\right]\right\} \sin \Delta_{31}L \\
&\quad + O(\epsilon^5), \\
P_{\mu s} &= 2\theta_{24}^2 + \left[\theta_{34}^2 \left(1 - \frac{\theta_{34}^2}{3}\right) - \theta_{24}^2\right] \sin^2 \frac{\Delta_{31}L}{2} - \theta_{24}\theta_{34} \sin \delta_3 \sin \Delta_{31}L \\
&\quad + O(\epsilon^5).
\end{aligned}$$

Acknowledgments

We acknowledge H. Minakata for useful comments, M. Maltoni and P. Migliozzi for useful discussions, and P. Lipari and M. Lusignoli for discussions. The work has been partially supported by the JSPS-CSIC Bilateral Joint Projects (Japan- Spain), a Grant-in-Aid for

Scientific Research of the Ministry of Education, Science and Culture of Japan, #19340062. K.F. thanks the support by the MEXT program "Support Program for Improving Graduate School Education"; J. L.-P. acknowledges partial financial support by the Ministry of Science and Innovation of Spain (MICINN) through an FPU grant, ref. AP2005-1185; A.D. acknowledges partial financial support by the Istituto Nazionale di Fisica Nucleare (INFN) through the Iniziativa Specifica RM21 for foreign guests; and by the MICINN through the research project FPA2006-05423 and through the INFN-MICINN-08 Bilateral Agreement (Italy-Spain) "Flavour as a window for new physics"; D.M. acknowledges partial financial support by Ministry of University and of Scientific Research of Italy, through the 2007-08 COFIN program. A.D. and J.L.-P. acknowledge also financial support from the Comunidad Autónoma de Madrid through the project P-ESP-00346. Eventually, A.D., J.L.-P. and D.M. acknowledge the financial support of the European Community under the European Commission Framework Programme 7 Design Study: EUROnu, Project Number 212372; and under the Framework Programme 6 BENE-CARE networking activity MRTN-CT-2004-506395. The EC is not liable for any use that may be made of the information contained herein.

A.D. and J.L.-P. thank the Physics Department of the Università di Roma "La Sapienza", where this work has been completed.

References

- [1] B.T. Cleveland et al., *Measurement of the solar electron neutrino flux with the Homestake chlorine detector*, *Astrophys. J.* **496** (1998) 505 [[SPIRES](#)].
- [2] SAGE collaboration, J.N. Abdurashitov et al., *Measurement of the solar neutrino capture rate with gallium metal*, *Phys. Rev. C* **60** (1999) 055801 [[astro-ph/9907113](#)] [[SPIRES](#)].
- [3] GALLEX collaboration, W. Hampel et al., *GALLEX solar neutrino observations: results for GALLEX IV*, *Phys. Lett. B* **447** (1999) 127 [[SPIRES](#)].
- [4] SUPER-KAMIOKANDE collaboration, S. Fukuda et al., *Solar B-8 and hep Neutrino measurements from 1258 days of Super-Kamiokande data*, *Phys. Rev. Lett.* **86** (2001) 5651 [[hep-ex/0103032](#)] [[SPIRES](#)].
- [5] SUPER-KAMIOKANDE collaboration, J.P. Cravens et al., *Solar neutrino measurements in Super-Kamiokande-II*, *Phys. Rev. D* **78** (2008) 032002 [[arXiv:0803.4312](#)] [[SPIRES](#)].
- [6] SNO collaboration, Q.R. Ahmad et al., *Measurement of the charged current interactions produced by B-8 solar neutrinos at the Sudbury Neutrino Observatory*, *Phys. Rev. Lett.* **87** (2001) 071301 [[nucl-ex/0106015](#)] [[SPIRES](#)].
- [7] SNO collaboration, S.N. Ahmed et al., *Measurement of the total active B-8 solar neutrino flux at the Sudbury Neutrino Observatory with enhanced neutral current sensitivity*, *Phys. Rev. Lett.* **92** (2004) 181301 [[nucl-ex/0309004](#)] [[SPIRES](#)].
- [8] SNO collaboration, B. Aharmim et al., *An independent measurement of the total active 8B solar neutrino flux using an array of ^3He proportional counters at the sudbury Neutrino Observatory*, *Phys. Rev. Lett.* **101** (2008) 111301 [[arXiv:0806.0989](#)] [[SPIRES](#)].
- [9] SUPER-KAMIOKANDE collaboration, Y. Fukuda et al., *Evidence for oscillation of atmospheric neutrinos*, *Phys. Rev. Lett.* **81** (1998) 1562 [[hep-ex/9807003](#)] [[SPIRES](#)].

- [10] MACRO collaboration, M. Ambrosio et al., *Matter effects in upward-going muons and sterile neutrino oscillations*, *Phys. Lett. B* **517** (2001) 59 [[hep-ex/0106049](#)] [[SPIRES](#)].
- [11] CHOOZ collaboration, M. Apollonio et al., *Limits on neutrino oscillations from the CHOOZ experiment*, *Phys. Lett. B* **466** (1999) 415 [[hep-ex/9907037](#)] [[SPIRES](#)].
- [12] CHOOZ collaboration, M. Apollonio et al., *Search for neutrino oscillations on a long base-line at the CHOOZ nuclear power station*, *Eur. Phys. J. C* **27** (2003) 331 [[hep-ex/0301017](#)] [[SPIRES](#)].
- [13] F. Boehm et al., *Final results from the Palo Verde neutrino oscillation experiment*, *Phys. Rev. D* **64** (2001) 112001 [[hep-ex/0107009](#)] [[SPIRES](#)].
- [14] KAMLAND collaboration, K. Eguchi et al., *First results from KamLAND: evidence for reactor anti- neutrino disappearance*, *Phys. Rev. Lett.* **90** (2003) 021802 [[hep-ex/0212021](#)] [[SPIRES](#)].
- [15] K2K collaboration, M.H. Ahn et al., *Indications of neutrino oscillation in a 250 KM long-baseline experiment*, *Phys. Rev. Lett.* **90** (2003) 041801 [[hep-ex/0212007](#)] [[SPIRES](#)].
- [16] K2K collaboration, E. Aliu et al., *Evidence for muon neutrino oscillation in an accelerator-based experiment*, *Phys. Rev. Lett.* **94** (2005) 081802 [[hep-ex/0411038](#)] [[SPIRES](#)].
- [17] MINOS collaboration, D.G. Michael et al., *Observation of muon neutrino disappearance with the MINOS detectors and the NuMI neutrino beam*, *Phys. Rev. Lett.* **97** (2006) 191801 [[hep-ex/0607088](#)] [[SPIRES](#)].
- [18] MINOS collaboration, P. Adamson et al., *Measurement of neutrino oscillations with the MINOS detectors in the NuMI beam*, *Phys. Rev. Lett.* **101** (2008) 131802 [[arXiv:0806.2237](#)] [[SPIRES](#)].
- [19] PARTICLE DATA GROUP collaboration, C. Amsler et al., *Review of particle physics*, *Phys. Lett. B* **667** (2008) 1 [[SPIRES](#)].
- [20] B. Pontecorvo, *Mesonium and antimesonium*, *Sov. Phys. JETP* **6** (1957) 429 [*Zh. Eksp. Teor. Fiz.* **33** (1957) 549] [[SPIRES](#)].
- [21] Z. Maki, M. Nakagawa and S. Sakata, *Remarks on the unified model of elementary particles*, *Prog. Theor. Phys.* **28** (1962) 870 [[SPIRES](#)].
- [22] B. Pontecorvo, *Neutrino experiments and the question of leptonic-charge conservation*, *Sov. Phys. JETP* **26** (1968) 984 [*Zh. Eksp. Teor. Fiz.* **53** (1967) 1717] [[SPIRES](#)].
- [23] V.N. Gribov and B. Pontecorvo, *Neutrino astronomy and lepton charge*, *Phys. Lett. B* **28** (1969) 493 [[SPIRES](#)].
- [24] T. Schwetz, M.A. Tortola and J.W.F. Valle, *Three-flavour neutrino oscillation update*, *New J. Phys.* **10** (2008) 113011 [[arXiv:0808.2016](#)] [[SPIRES](#)].
- [25] G.L. Fogli, E. Lisi, A. Marrone, A. Palazzo and A.M. Rotunno, *What we (would like to) know about the neutrino mass*, [arXiv:0809.2936](#) [[SPIRES](#)].
- [26] G.L. Fogli, E. Lisi, A. Marrone, A. Palazzo and A.M. Rotunno, *Hints of $\theta_{13} > 0$ from global neutrino data analysis*, *Phys. Rev. Lett.* **101** (2008) 141801 [[arXiv:0806.2649](#)] [[SPIRES](#)].
- [27] H.L. Ge, C. Giunti and Q.Y. Liu, *Bayesian constraints on θ_{13} from solar and KamLAND neutrino data*, [arXiv:0810.5443](#) [[SPIRES](#)].
- [28] M.C. Gonzalez-Garcia and M. Maltoni, *Phenomenology with massive neutrinos*, *Phys. Rept.* **460** (2008) 1 [[arXiv:0704.1800](#)] [[SPIRES](#)].

- [29] THE T2K collaboration, Y. Itow et al., *The JHF-Kamioka neutrino project*, [hep-ex/0106019](#) [SPIRES].
- [30] NOvA collaboration, D.S. Ayres et al., *NOvA proposal to build a 30-kiloton off-axis detector to study neutrino oscillations in the Fermilab NuMI beamline*, [hep-ex/0503053](#) [SPIRES].
- [31] M. Ishitsuka, T. Kajita, H. Minakata and H. Nunokawa, *Resolving neutrino mass hierarchy and CP degeneracy by two identical detectors with different baselines*, *Phys. Rev. D* **72** (2005) 033003 [[hep-ph/0504026](#)] [SPIRES].
- [32] K. Hagiwara, N. Okamura and K.-i. Senda, *Solving the neutrino parameter degeneracy by measuring the T2K off-axis beam in Korea*, *Phys. Lett. B* **637** (2006) 266 [Erratum *ibid.* **B 641** (2006) 486] [[hep-ph/0504061](#)] [SPIRES].
- [33] M.V. Diwan et al., *Very long baseline neutrino oscillation experiments for precise measurements of mixing parameters and CP-violating effects*, *Phys. Rev. D* **68** (2003) 012002 [[hep-ph/0303081](#)] [SPIRES].
- [34] S. Geer, *Neutrino beams from muon storage rings: characteristics and physics potential*, *Phys. Rev. D* **57** (1998) 6989 [Erratum *ibid.* **D 59** (1999) 039903] [[hep-ph/9712290](#)] [SPIRES].
- [35] P. Zucchelli, *A novel concept for a $\bar{\nu}_e/\nu_e$ neutrino factory: the beta beam*, *Phys. Lett. B* **532** (2002) 166 [SPIRES].
- [36] BELLE experiment, <http://belle.kek.jp/>.
- [37] BABAR experiment, <http://www-public.slac.stanford.edu/babar/>.
- [38] Y. Grossman, *Nonstandard neutrino interactions and neutrino oscillation experiments*, *Phys. Lett. B* **359** (1995) 141 [[hep-ph/9507344](#)] [SPIRES].
- [39] M.M. Guzzo, A. Masiero and S.T. Petcov, *On the MSW effect with massless neutrinos and no mixing in the vacuum*, *Phys. Lett. B* **260** (1991) 154 [SPIRES].
- [40] E. Roulet, *Mikheyev-Smirnov-Wolfenstein effect with flavor-changing neutrino interactions*, *Phys. Rev. D* **44** (1991) 935 [SPIRES].
- [41] S. Antusch, C. Biggio, E. Fernandez-Martinez, M.B. Gavela and J. Lopez-Pavon, *Unitarity of the leptonic mixing matrix*, *JHEP* **10** (2006) 084 [[hep-ph/0607020](#)] [SPIRES].
- [42] A. Abada, C. Biggio, F. Bonnet, M.B. Gavela and T. Hambye, *Low energy effects of neutrino masses*, *JHEP* **12** (2007) 061 [[arXiv:0707.4058](#)] [SPIRES].
- [43] ISS PHYSICS WORKING GROUP collaboration, A. Bandyopadhyay et al., *Physics at a future Neutrino Factory and super-beam facility*, [arXiv:0710.4947](#) [SPIRES].
- [44] T. Ota, J. Sato and N.-a. Yamashita, *Oscillation enhanced search for new interaction with neutrinos*, *Phys. Rev. D* **65** (2002) 093015 [[hep-ph/0112329](#)] [SPIRES].
- [45] T. Ota and J. Sato, *Can ICARUS and OPERA give information on a new physics?*, *Phys. Lett. B* **545** (2002) 367 [[hep-ph/0202145](#)] [SPIRES].
- [46] E. Fernandez-Martinez, M.B. Gavela, J. Lopez-Pavon and O. Yasuda, *CP-violation from non-unitary leptonic mixing*, *Phys. Lett. B* **649** (2007) 427 [[hep-ph/0703098](#)] [SPIRES].
- [47] G. Altarelli and D. Meloni, *CP violation in neutrino oscillations and new physics*, *Nucl. Phys. B* **809** (2009) 158 [[arXiv:0809.1041](#)] [SPIRES].

- [48] LSND collaboration, C. Athanassopoulos et al., *Evidence for $\bar{\nu}_\mu \rightarrow \bar{\nu}_e$ oscillation from the LSND experiment at the Los Alamos meson physics facility*, *Phys. Rev. Lett.* **77** (1996) 3082 [[nucl-ex/9605003](#)] [[SPIRES](#)].
- [49] LSND collaboration, C. Athanassopoulos et al., *Evidence for $\nu_\mu \rightarrow \nu_e$ neutrino oscillations from LSND*, *Phys. Rev. Lett.* **81** (1998) 1774 [[nucl-ex/9709006](#)] [[SPIRES](#)].
- [50] LSND collaboration, A. Aguilar et al., *Evidence for neutrino oscillations from the observation of $\bar{\nu}_e$ appearance in a $\bar{\nu}_\mu$ beam*, *Phys. Rev. D* **64** (2001) 112007 [[hep-ex/0104049](#)] [[SPIRES](#)].
- [51] ALEPH collaboration, *Precision electroweak measurements on the Z resonance*, *Phys. Rept.* **427** (2006) 257 [[hep-ex/0509008](#)] [[SPIRES](#)].
- [52] THE MINIBOONE collaboration, A.A. Aguilar-Arevalo et al., *A search for electron neutrino appearance at the $\Delta m^2 \sim 1\text{eV}^2$ scale*, *Phys. Rev. Lett.* **98** (2007) 231801 [[arXiv:0704.1500](#)] [[SPIRES](#)].
- [53] M. Sorel, J.M. Conrad and M. Shaevitz, *A combined analysis of short-baseline neutrino experiments in the (3+1) and (3+2) sterile neutrino oscillation hypotheses*, *Phys. Rev. D* **70** (2004) 073004 [[hep-ph/0305255](#)] [[SPIRES](#)].
- [54] M. Maltoni and T. Schwetz, *Sterile neutrino oscillations after first MiniBooNE results*, *Phys. Rev. D* **76** (2007) 093005 [[arXiv:0705.0107](#)] [[SPIRES](#)].
- [55] V. Barger, D. Marfatia and K. Whisnant, *Confronting mass-varying neutrinos with MiniBooNE*, *Phys. Rev. D* **73** (2006) 013005 [[hep-ph/0509163](#)] [[SPIRES](#)].
- [56] S. Palomares-Ruiz, S. Pascoli and T. Schwetz, *Explaining LSND by a decaying sterile neutrino*, *JHEP* **09** (2005) 048 [[hep-ph/0505216](#)] [[SPIRES](#)].
- [57] A. de Gouvêa and Y. Grossman, *A three-flavor, Lorentz-violating solution to the LSND anomaly*, *Phys. Rev. D* **74** (2006) 093008 [[hep-ph/0602237](#)] [[SPIRES](#)].
- [58] T. Schwetz, *LSND versus MiniBooNE: sterile neutrinos with energy dependent masses and mixing?*, *JHEP* **02** (2008) 011 [[arXiv:0710.2985](#)] [[SPIRES](#)].
- [59] A.E. Nelson and J. Walsh, *Short baseline neutrino oscillations and a new light gauge boson*, *Phys. Rev. D* **77** (2008) 033001 [[arXiv:0711.1363](#)] [[SPIRES](#)].
- [60] A. Donini, M. Maltoni, D. Meloni, P. Migliozzi and F. Terranova, *3+1 sterile neutrinos at the CNGS*, *JHEP* **12** (2007) 013 [[arXiv:0704.0388](#)] [[SPIRES](#)].
- [61] CNGS experiment, <http://proj-cngs.web.cern.ch/proj-cngs/>.
- [62] K. Kimura, A. Takamura and H. Yokomakura, *Exact formula of probability and CP-violation for neutrino oscillations in matter*, *Phys. Lett. B* **537** (2002) 86 [[hep-ph/0203099](#)] [[SPIRES](#)].
- [63] K. Kimura, A. Takamura and H. Yokomakura, *All you ever want to know about neutrino oscillation probabilities in constant matter*, *Phys. Rev. D* **66** (2002) 073005 [[hep-ph/0205295](#)] [[SPIRES](#)].
- [64] A. Donini and D. Meloni, *The 2+2 and 3+1 four-family neutrino mixing at the neutrino factory*, *Eur. Phys. J. C* **22** (2001) 179 [[hep-ph/0105089](#)] [[SPIRES](#)].
- [65] A. Donini, M. Lusignoli and D. Meloni, *Telling three from four neutrinos at the neutrino factory*, *Nucl. Phys. B* **624** (2002) 405 [[hep-ph/0107231](#)] [[SPIRES](#)].

- [66] ISS DETECTOR WORKING GROUP collaboration, T. Abe et al., *Detectors and flux instrumentation for future neutrino facilities*, 2009 *JINST* **4** T05001 [[arXiv:0712.4129](#)] [[SPIRES](#)].
- [67] A. Cervera et al., *Golden measurements at a neutrino factory*, *Nucl. Phys. B* **579** (2000) 17 [*Erratum ibid.* **593** (2001) 731] [[hep-ph/0002108](#)] [[SPIRES](#)].
- [68] A. Donini, D. Meloni and P. Migliozzi, *The silver channel at the Neutrino Factory*, *Nucl. Phys. B* **646** (2002) 321 [[hep-ph/0206034](#)] [[SPIRES](#)].
- [69] J. Burguet-Castell, M.B. Gavela, J.J. Gomez-Cadenas, P. Hernández and O. Mena, *On the measurement of leptonic CP-violation*, *Nucl. Phys. B* **608** (2001) 301 [[hep-ph/0103258](#)] [[SPIRES](#)].
- [70] H. Minakata and H. Nunokawa, *Exploring neutrino mixing with low energy superbeams*, *JHEP* **10** (2001) 001 [[hep-ph/0108085](#)] [[SPIRES](#)].
- [71] A. Donini, M.B. Gavela, P. Hernández and S. Rigolin, *Neutrino mixing and CP-violation*, *Nucl. Phys. B* **574** (2000) 23 [[hep-ph/9909254](#)] [[SPIRES](#)].
- [72] A. Donini, M.B. Gavela, P. Hernández and S. Rigolin, *Four species neutrino oscillations at nu-factory: sensitivity and CP-violation*, *Nucl. Instrum. Meth. A* **451** (2000) 58 [[hep-ph/9910516](#)] [[SPIRES](#)].
- [73] A. Kalliomaki, J. Maalampi and M. Tanimoto, *Search for CP-violation at a neutrino factory in a four- neutrino model*, *Phys. Lett. B* **469** (1999) 179 [[hep-ph/9909301](#)] [[SPIRES](#)].
- [74] A. Dighe and S. Ray, *Signatures of heavy sterile neutrinos at long baseline experiments*, *Phys. Rev. D* **76** (2007) 113001 [[arXiv:0709.0383](#)] [[SPIRES](#)].
- [75] A. Boyarsky, A. Neronov, O. Ruchayskiy and M. Shaposhnikov, *Constraints on sterile neutrino as a dark matter candidate from the diffuse X-ray background*, *Mon. Not. Roy. Astron. Soc.* **370** (2006) 213 [[astro-ph/0512509](#)] [[SPIRES](#)].
- [76] M. Maltoni, T. Schwetz, M.A. Tortola and J.W.F. Valle, *Status of global fits to neutrino oscillations*, *New J. Phys.* **6** (2004) 122 [[hep-ph/0405172](#)] [[SPIRES](#)].
- [77] N. Okada and O. Yasuda, *A sterile neutrino scenario constrained by experiments and cosmology*, *Int. J. Mod. Phys. A* **12** (1997) 3669 [[hep-ph/9606411](#)] [[SPIRES](#)].
- [78] S.M. Bilenky, C. Giunti and W. Grimus, *Neutrino mass spectrum from the results of neutrino oscillation experiments*, *Eur. Phys. J. C* **1** (1998) 247 [[hep-ph/9607372](#)] [[SPIRES](#)].
- [79] F. Dydak et al., *A search for Muon-neutrino oscillations in the Δm^2 range $0.3 - eV^2 \rightarrow 90 - eV^2$* , *Phys. Lett. B* **134** (1984) 281 [[SPIRES](#)].
- [80] Y. Declais et al., *Search for neutrino oscillations at 15-meters, 40-meters and 95-meters from a nuclear power reactor at Bugey*, *Nucl. Phys. B* **434** (1995) 503 [[SPIRES](#)].
- [81] G. Karagiorgi et al., *Leptonic CP-violation studies at MiniBooNE in the (3+2) sterile neutrino oscillation hypothesis*, *Phys. Rev. D* **75** (2007) 013011 [[hep-ph/0609177](#)] [[SPIRES](#)].
- [82] S.M. Bilenky, C. Giunti, W. Grimus and T. Schwetz, *Four-neutrino mixing and big-bang nucleosynthesis*, *Astropart. Phys.* **11** (1999) 413 [[hep-ph/9804421](#)] [[SPIRES](#)].
- [83] R. Foot and R.R. Volkas, *Studies of neutrino asymmetries generated by ordinary sterile neutrino oscillations in the early universe and implications for big bang nucleosynthesis bounds*, *Phys. Rev. D* **55** (1997) 5147 [[hep-ph/9610229](#)] [[SPIRES](#)].

- [84] M. Cirelli, G. Marandella, A. Strumia and F. Vissani, *Probing oscillations into sterile neutrinos with cosmology, astrophysics and experiments*, *Nucl. Phys. B* **708** (2005) 215 [[hep-ph/0403158](#)] [[SPIRES](#)].
- [85] A. De Rujula, M. Lusignoli, L. Maiani, S.T. Petcov and R. Petronzio, *A fresh look at neutrino oscillations*, *Nucl. Phys. B* **168** (1980) 54 [[SPIRES](#)].
- [86] A.M. Dziewonski and D.L. Anderson, *Preliminary reference earth model*, *Phys. Earth Planet. Interiors* **25** (1981) 297 [[SPIRES](#)].
- [87] S.K. Agarwalla, S. Choubey and A. Raychaudhuri, *Neutrino mass hierarchy and θ_{13} with a magic baseline beta-beam experiment*, *Nucl. Phys. B* **771** (2007) 1 [[hep-ph/0610333](#)] [[SPIRES](#)].
- [88] A. Bueno, M. Campanelli and A. Rubbia, *Physics potential at a neutrino factory: can we benefit from more than just detecting muons?*, *Nucl. Phys. B* **589** (2000) 577 [[hep-ph/0005007](#)] [[SPIRES](#)].
- [89] M. Campanelli, A. Bueno and A. Rubbia, *$\nu_\mu \rightarrow \nu_\tau$ oscillations appearance with kinematic approach at very long baselines (VLBL)*, *Nucl. Instrum. Meth. A* **451** (2000) 176 [[SPIRES](#)].
- [90] A. De Rujula, M.B. Gavela and P. Hernández, *Neutrino oscillation physics with a neutrino factory*, *Nucl. Phys. B* **547** (1999) 21 [[hep-ph/9811390](#)] [[SPIRES](#)].
- [91] A. Broncano and O. Mena, *Corrections to the fluxes of a neutrino factory*, *Eur. Phys. J. C* **29** (2003) 197 [[hep-ph/0203052](#)] [[SPIRES](#)].
- [92] B. Autin, A. Blondel and J.R. Ellis, *Prospective study of muon storage rings at CERN*, CERN-YELLOW-99-02 [[SPIRES](#)].
- [93] P. Gruber et al., *The study of a European neutrino factory complex*, CERN-NUFACT-NOTE-103 [[SPIRES](#)].
- [94] D. Finley and N. Holtkamp, *A feasibility study of a neutrino source based on a muon storage ring*, *Nucl. Instrum. Meth. A* **472** (2000) 388 [[SPIRES](#)].
- [95] S. Ozaki et al., *Feasibility study 2 of a muon based neutrino source*, BNL-52623 [[SPIRES](#)].
- [96] MUON COLLIDER/NEUTRINO FACTORY collaboration, M.M. Alsharoa et al., *Recent progress in neutrino factory and muon collider research within the Muon collaboration*, *Phys. Rev. ST Accel. Beams* **6** (2003) 081001 [[hep-ex/0207031](#)] [[SPIRES](#)].
- [97] M.S. Zisman, *Technical design aspects of feasibility study-II*, *Nucl. Instrum. Meth. A* **503** (2003) 384 [[SPIRES](#)].
- [98] Y. Kuno et al., *A feasibility study of a neutrino factory in Japan*, [[SPIRES](#)].
- [99] M.S. Zisman, *International Scoping Study: accelerator working group report*, *J. Phys. Conf. Ser.* **110** (2008) 112006. [[SPIRES](#)].
- [100] P. Lipari, private communication.
- [101] P. Lipari, M. Lusignoli and F. Sartogo, *The Neutrino cross-section and upward going muons*, *Phys. Rev. Lett.* **74** (1995) 4384 [[hep-ph/9411341](#)] [[SPIRES](#)].
- [102] A. Cervera-Villanueva, *MIND performance and prototyping*, *AIP Conf. Proc.* **981** (2008) 178 [[SPIRES](#)].
- [103] A. Cervera, F. Dydak and J. Gomez Cadenas, *A large magnetic detector for the neutrino factory*, *Nucl. Instrum. Meth. A* **451** (2000) 123 [[SPIRES](#)].

- [104] D. Autiero et al., *The synergy of the golden and silver channels at the Neutrino Factory*, *Eur. Phys. J. C* **33** (2004) 243 [[hep-ph/0305185](#)] [[SPIRES](#)].
- [105] P. Huber and W. Winter, *Neutrino factories and the 'magic' baseline*, *Phys. Rev. D* **68** (2003) 037301 [[hep-ph/0301257](#)] [[SPIRES](#)].
- [106] J. Kopp, T. Ota and W. Winter, *Neutrino factory optimization for non-standard interactions*, *Phys. Rev. D* **78** (2008) 053007 [[arXiv:0804.2261](#)] [[SPIRES](#)].
- [107] G.L. Fogli and E. Lisi, *Tests of three-flavor mixing in long-baseline neutrino oscillation experiments*, *Phys. Rev. D* **54** (1996) 3667 [[hep-ph/9604415](#)] [[SPIRES](#)].
- [108] V. Barger, D. Marfatia and K. Whisnant, *Breaking eight-fold degeneracies in neutrino CP-violation, mixing and mass hierarchy*, *Phys. Rev. D* **65** (2002) 073023 [[hep-ph/0112119](#)] [[SPIRES](#)].
- [109] A. Donini, E. Fernandez-Martinez, D. Meloni and S. Rigolin, *ν_μ disappearance at the SPL, T2K-I, NOnuA and the neutrino factory*, *Nucl. Phys. B* **743** (2006) 41 [[hep-ph/0512038](#)] [[SPIRES](#)].
- [110] P. Huber and T. Schwetz, *A low energy neutrino factory with non-magnetic detectors*, *Phys. Lett. B* **669** (2008) 294 [[arXiv:0805.2019](#)] [[SPIRES](#)].
- [111] MINOS collaboration, E. Ales et al., *P-875: A long baseline neutrino oscillation experiment at Fermilab, NUMI-L-79* [[SPIRES](#)].
- [112] P. Huber, M. Lindner, M. Rolinec and W. Winter, *Optimization of a neutrino factory oscillation experiment*, *Phys. Rev. D* **74** (2006) 073003 [[hep-ph/0606119](#)] [[SPIRES](#)].
- [113] INO collaboration, D. Indumathi, *India-based Neutrino Observatory (INO)*, *Pramana* **63** (2004) 1283 [[SPIRES](#)].
- [114] C. Fukushima et al., *A thin emulsion spectrometer using a compact permanent magnet*, *Nucl. Instrum. Meth. A* **592** (2008) 56 [[SPIRES](#)].
- [115] D. Meloni, *Solving the octant degeneracy with the Silver channel*, *Phys. Lett. B* **664** (2008) 279 [[arXiv:0802.0086](#)] [[SPIRES](#)].
- [116] P. Migliozzi, private communication.
- [117] L. Scotto Lavina, *Design and Performance of ECC-MECC* talk at the *NuFact'08 Workshop*, Valencia, [PoS\(NUFACT08\)049](#).
- [118] K. Fuki, *Sterile neutrino oscillation at a neutrino factory*, poster at the *NuFact'08 Workshop*, Valencia, [PoS\(NUFACT08\)123](#).
- [119] D. Meloni, *Sterile neutrinos at future long baseline experiments*, *Nucl. Phys. Proc. Suppl.* **188** (2009) 207 [[arXiv:0812.3555](#)] [[SPIRES](#)].
- [120] M.C. Gonzalez-Garcia, M. Maltoni and A.Y. Smirnov, *Measuring the deviation of the 2-3 lepton mixing from maximal with atmospheric neutrinos*, *Phys. Rev. D* **70** (2004) 093005 [[hep-ph/0408170](#)] [[SPIRES](#)].
- [121] P. Huber, M. Lindner and W. Winter, *Superbeams versus neutrino factories*, *Nucl. Phys. B* **645** (2002) 3 [[hep-ph/0204352](#)] [[SPIRES](#)].
- [122] A. Donini, D. Meloni and S. Rigolin, *Clone flow analysis for a theory inspired neutrino experiment planning*, *JHEP* **06** (2004) 011 [[hep-ph/0312072](#)] [[SPIRES](#)].
- [123] A. Laing and F.J.P. Soler, *Flux measurement at a neutrino factory near detector for neutrino oscillations*, *AIP Conf. Proc.* **981** (2008) 166 [[SPIRES](#)].

- [124] Z.-z. Xing and H. Zhang, *Reconstruction of the neutrino mixing matrix and leptonic unitarity triangles from long-baseline neutrino oscillations*, *Phys. Lett. B* **618** (2005) 131 [[hep-ph/0503118](#)] [[SPIRES](#)].
- [125] O. Yasuda, *On the exact formula for neutrino oscillation probability by Kimura, Takamura and Yokomakura*, [arXiv:0704.1531](#) [[SPIRES](#)].
- [126] H. Zhang, *Sum rules of four-neutrino mixing in matter*, *Mod. Phys. Lett. A* **22** (2007) 1341 [[hep-ph/0606040](#)] [[SPIRES](#)].